

Role of Disorder and Interactions on the Surface of Topological Superconductors

Von der Fakultät Mathematik und Physik der Universität Stuttgart zur
Erlangung der Würde eines Doktors der Naturwissenschaften
(Dr. rer. nat.) genehmigte Abhandlung

vorgelegt von

Raquel Pinheiro de Almeida Queiroz

aus Lisboa, PORTUGAL

Hauptberichter: Prof. Dr. Walter Metzner
Mitberichter: Dr. Andreas Schnyder
Prof. Dr. Maria Daghofer
Prof. Dr. Tilman Pfau

Tag der mündlichen Prüfung: 21 Oktober 2015

MAX-PLANCK-INSTITUT FÜR FESTKÖRPERFORSCHUNG
STUTT GART 2015

Para o meu pai, mãe e irmã

Abstract

In this work we study the surface properties of topological systems, with a special focus on topological superconductors without inversion symmetry. These materials provide a rich playground for multiple topological phenomena, showing boundary modes with linear and (or) flat dispersion arising from complex nodal structures.

A remarkable characteristic of topological phases is their robustness to local perturbations. In usual topological phases such as topological band insulators, this protection owes its existence to the presence of a pronounced energy gap separating topological sectors. In the present work, we explore the extent to which this robustness can be generalized to gapless topological phases. We numerically test the robustness of topological boundary modes against local disorder and explore the contrast between different disorder strengths and distributions.

An experimental signature is proposed to detect and distinguish the exotic topological boundary modes in the limit of dilute disorder, with Fourier-transform scanning tunneling microscopy in mind. We show that each type of surface state carries a universal feature in its scattering interference pattern, hence making this surface technique particularly suitable.

We further explore the consequences of strong surface disorder, which does not drastically alter the bulk's topology. We show that two limits are of particular interest. First, we consider strong fluctuations in the surface's electrostatic potential, which lead to the formation of a high density of Anderson localized impurity states on the surface. We show that these impurity states mediate scattering within the boundary modes due to their energy proximity. Consequently, this type of disorder is particularly harmful for topological surface states, in particular for potential fluctuations with comparable strength to the system's bandwidth.

The second limit of disorder concerns strong surface impurities, which can equivalently be regarded as lattice vacancies or surface roughness. We show that in the presence of this type of disorder, the topological states migrate to inner layers. Hence, lattice vacancies or surface roughness cannot harm the topological boundary modes of both gapped and gapless phases. It follows that the existence of the topological surface states does not depend on translational symmetry. We show that substituting one disorder regime by the other by inducing strong localized surface scatterers can lead to a sharper signal in photoemission measurements after sputtering samples of the topological insulator bismuth selenide.

Additionally, we study the interplay between topology and electron-electron interactions

at the surface of nodal superconductors, where the infinitely degenerate flat bands are susceptible to spontaneous symmetry breaking. We show that for singly degenerate flat bands, time reversal symmetry is spontaneously broken due to the emergence of a complex superconducting pairing amplitude, leading to the generation of spontaneous chiral currents at the surface of the nodal topological superconductors.

Finally, we briefly look into possible symmetry preserving interactions that can lead to the destruction of the boundary modes. It was recently proposed that the single particle topology of one dimensional topological superconductors collapses in the presence of interactions if its invariant is a multiple of 8. Using a dimensional hierarchy approach, we propose a generalized form of a quartic interaction that allows for the adiabatic connection of topological sectors, distinct in the non-interacting limit.

Contents

0. Preface	1
1. Theoretical background	7
1.1. Topological phases of matter	7
1.1.1. Symmetry classes	9
1.1.2. Topological classification of matrix Hamiltonians	11
1.1.3. Bott periodicity	18
1.1.4. Topological invariants	20
1.2. Disorder	23
1.2.1. Wave function localization	23
1.2.2. Role of symmetry in transport	24
1.2.3. Nature of Anderson phase transitions	27
1.2.4. Types of disorder	28
1.2.5. Topology in disordered systems	28
1.2.6. Topology in disordered nodal systems	29
1.3. A very short introduction to superconductivity	31
1.3.1. BCS superconductivity	31
1.3.2. Unconventional superconductivity	32
1.3.3. Noncentrosymmetric superconductors	35
1.3.4. Superfluid ^3He	37
1.4. This thesis	39
2. Topological surface states in noncentrosymmetric superconductors	41
2.1. Bulk-boundary correspondence in nodal systems	41
2.2. Overview of the different types of topological surface states in 2D and 3D	45
2.3. Model: Noncentrosymmetric superconductors	45
2.3.1. Impurity Hamiltonian	50
2.4. Helical Majorana states	51
2.4.1. Helical Majorana state in 2D	51
2.4.2. Helical Majorana state in 3D	54

2.5. Arc surface states	56
2.6. Flat-band edge-states	57
2.7. Conclusion	64
3. Quasiparticle interference: Experimental signatures of topological surface states	65
3.1. Introduction	65
3.2. Local density of states with dilute impurities	68
3.3. Analytical result in the centrosymmetric limit	69
3.4. Numerical results for noncentrosymmetric superconductors	72
3.5. Conclusion	76
4. Beyond low energy: Dirac edge and surface states	77
4.1. Bi_2Se_3 : A 3D topological insulator	77
4.1.1. Numerical simulation	80
4.1.2. Experimental results	82
4.1.3. Discussion	83
4.2. Topological superconductors	86
4.2.1. Numerical simulation	87
4.2.2. Three-dimensional topological NCS	88
4.2.3. Two-dimensional topological NCS	93
4.2.4. Magnetic surface disorder	96
4.2.5. Conclusion	96
5. Beyond low energy: Flat-band edge states	99
5.1. Edge states at irregularly shaped boundaries	99
5.2. Strong edge disorder	103
5.2.1. Nonmagnetic impurities	103
5.2.2. Magnetic impurities	105
5.3. Conclusion	106
6. Effects of correlations on highly degenerate surface states	107
6.1. Self-consistent Gap equation	108
6.2. Phase diagram and nodal structure	110
6.3. Surface current	111
6.4. Numerical results	112
6.5. Role of Majorana flat bands for TRS breaking	117
6.6. Role of Majorana arc state for TRS breaking	118
6.7. Conclusion	120

7. Topology of interacting fermions	121
7.1. Dimensional hierarchy in noninteracting fermions	122
7.1.1. Complex classes $A \leftrightarrow AIII$	122
7.1.2. Real classes $DIII \leftrightarrow D \leftrightarrow BDI \leftrightarrow \dots$	124
7.2. Breakdown of \mathbb{Z} classification in BDI chains	126
7.3. Dimensional hierarchy for interacting fermions	127
7.3.1. Example: From BDI to DIII	127
7.3.2. General reduction mechanism	129
7.3.3. General form of the interaction	132
7.4. Conclusion	133
8. Conclusion and Outlook	135
A. Point group symmetries	137
B. Recursive Green's function	139
Bibliography	143

0. Preface

Solid state physics is a compelling field devoted to the study of collective properties of a large number of fundamental particles. Intriguing emergent phases can be manifested due to non-trivial electron-electron interactions. Examples are metallic phases of dispersing electrons which turn, upon lowering the temperature, into phases of coherent bosons, or alternately, phases of half-fermions by spatially separating their degrees of freedom. Our vast understanding of phases of matter relies on the insightful description of phase transitions proposed by Ginzburg and Landau [1, 2] where emergent phases are described by local order parameters which acquire a non-vanishing value under symmetry breaking, together with a decrease in the system's free energy. Examples of these types of ordered states include magnets, crystals, superconductors, and superfluids.

Since its discovery in 1911 [3], superconductivity has continued to be a fascinating subject, keeping many of the greatest minds in the last and present century puzzled. The beginnings of our comprehension of the problem can be attributed to Bardeen, Cooper and Schrieffer [4], who discovered in 1957 the microscopic theory of conventional superconductivity (BCS theory). Briefly summarized, it was shown that the retardation effect due to Coulomb overscreening allows for an effective attractive interaction between electrons. Due to this attractive interaction, the electrons form bosonic Cooper pairs, which condense into a coherent macroscopic quantum state, the Cooper pair condensate. This condensate is a coherent macroscopic state, which has been observed experimentally innumerable times and widely applied in technology, evidencing the importance of our fundamental understanding of the electron's quantum character.

With the discovery of high-temperature superconductors by Bednorz and Müller in 1986 [5], it became clear that the understanding of superconductivity was far from complete, particularly the nature of its underlying microscopic mechanism. It is understood that the longer range of the correlation functions in comparison to normal BCS superconductors excludes electron-phonon coupling as the driving force behind this unusual phase of matter. Spin-fluctuations are proposed [6, 7] to lead to such phases, showing that the phase character of the condensate can in fact be quite complex, allowing for high-angular momentum pairing functions, with strongly anisotropic coherent phase. The complexity of the order parameter opens the door for yet another extraordinary perspective, which will be explored in the present work.

Parallel to these discoveries, von Klitzing [8] observed in a rather dirty sample of gallium arsenide the quantum Hall effect (QHE). The QHE had immediately a wide impact, as for the first time a transport property was measured that did not seem to depend on any details of the system, with an exactly quantized value of conductivity of e^2/h , to 10^{-9} precision. Such phenomena required a fundamental explanation relying on the global, rather than local properties of the wave functions. The discovery of the QHE marked the beginning of an intense study of topological phases of matter in solid state physics. It is nowadays clear, that quasiparticle wave functions (fermionic quasiparticles or emergent bosons such as Cooper pairs) can be non-local objects, present due to the existence of topologically separated sectors in the landscape of gapped Hamiltonians. Having a full gap in the bulk, the QHE owes its perfect conductivity to chiral boundary modes with linear dispersion, that avoid local backscattering due to their topological character. A topological phase transition can be driven by applying a strong magnetic field, forcing the Fermi level to cross a Landau level. In this process a metallic intermediate state is reached and a different number of boundary modes is localized at the edges.

Although the connection between the QHE and superconductivity seems unexpected, in the following I wish to make this relationship clear. Unconventional superconductors, such as high-temperature superconductors, due to their non-trivial pairing symmetry can show equivalent topological character which results in boundary modes. Here, the superconducting gap is regarded as the protecting gap which stabilizes the topological phase. In unconventional superconductors, given the possibility of high-angular momentum pairing, the gap can vanish at some regions in momentum space, the nodal structures. This leads to remarkably rich topological features, allowing for both boundary modes of flat or linear dispersion. Due to the lack of a full bulk gap, nodal phases can also be more susceptible to perturbations.

In summary, a topological material is characterized by an insulating or semi-metallic bulk allowing for perfectly conducting modes localized on its boundary, insensitive to local perturbations [9, 10]. Boundary states are responsible both for the perfectly quantized conductivity in the QHE [11], and the zero-energy flat band observed in high-temperature cuprate superconductors [12]. The existence of boundary modes in topological phases is universal, as it depends uniquely on global symmetry considerations rather than local details which are material or model dependent.

Superconductivity leads to a global symmetry between electron and hole excitations: the spectrum is symmetric about zero energy, with a state at energy $-E$ for each state at $+E$. Any midgap (boundary) state must be pinned exactly at $E = 0$, i.e. a Majorana fermion [13]. From this restriction many unusual properties emerge and the search for understanding and observation of this particle has been the target of intense focus from the community in

the past years [14]. Although isolated Majoranas call for our attention [15], finding fully gapped superconductors hosting them has been proven quite challenging. It is however experimentally feasible that unconventional topological superconductors with complex nodal structures are found in nature, possibly hosting various realizations of boundary states with different dispersions. Some candidate materials have been proposed [16], however direct evidence of Majorana boundary modes is still lacking. It is therefore relevant to understand in detail the effects of perturbations, either from disorder or electronic correlations, in the different types of topological boundary states. In this way, not only can we explore the extent to which these states can be applied to future technologies, but also it allows us to identify key characteristics that might facilitate their experimental detection.

Accordingly, this text will be focused on the richness of topological states in nodal superconductors, and the possibility of their observation under real experimental conditions. For this purpose we will focus our attention on noncentrosymmetric superconductors (NCSs), serving as representatives for a larger class of topological materials. NCSs are unconventional superconductors without inversion symmetry, which are relatively common among anisotropic superconductors [17]. They arise in heavy fermion systems, where the strong interplay between superconductivity and magnetism favors pairing symmetries with high angular momentum, but also in weakly correlated systems with strong spin-orbit coupling [16]. Most NCS materials show nodal points and lines leading to remarkably rich topological features.

The topological features of the materials discussed here can be described in their entirety using quadratic mean-field Hamiltonians. That is, systems where electron-electron correlations can be described at the mean-field level and do not play an essential role. Consequently, the study of mean-field approximate Hamiltonians is generally sufficient. The interplay between interactions and this sort of topological order is, however, not yet fully understood. On one hand, the interplay between correlations at the surface of topological materials, where boundary states are localized, still requires further investigation. On the other hand, it is interesting to explore the role of symmetry preserving interactions in the bulk, which can lead to a change in the topological sector without closing the bulk gap, possibly leading to the full destruction of boundary modes.

This thesis is organized as follows:

Theoretical background

Chapter 1 discusses the main concepts necessary to contextualize this thesis. It is directed at readers unfamiliar with the topic, focusing on the role of symmetry in single-particle topological phases. Topological phases are discussed in detail and an introduction to symmetry in disordered media follows. Superconductivity is briefly discussed focusing on pairing symmetries, and examples of possible topological materials are given.

Topological surface states in noncentrosymmetric superconductors

Chapter 2 is dedicated to clarifying the relationship between bulk topological invariants and the resulting boundary theories in both gapped and gapless systems. The model in study is introduced and an overview of the possible surface states in noncentrosymmetric superconductors is given. We find the explicit solution of the topological boundary modes under a few approximations.

» Part of the content of this chapter is found in Refs. (i) and (ii) in the list of publications.

Quasiparticle interference: Experimental signatures of topological surface states

Chapter 3 builds upon the results from the previous chapter to propose experimental signatures of the topological surface states. It is shown that the pairing symmetry of the unconventional superconductor can be identified from measurements of the surface states.

» This chapter is published in Ref. (i).

Beyond low energy

In chapters 4 and 5, we examine the effect of strong surface disorder in order to test the limits of the topological protection. Nodal superconductors pose a significant obstacle when trying to tackle the problem in a purely analytic fashion. The strong anisotropies caused by unconventional pairing and spin orbit coupling make the problems nearly unsolvable without resorting to powerful numerical tools. Accordingly, we use exact diagonalization and recursive Green's function methods to determine the effects of strong disorder on the surface states. The approach we use allows us to account for the interplay between surface states (protected from disorder) and bulk or localized impurity states (not topologically protected from disorder). The numerical calculations are adapted and compared to the case of the

topological insulator Bi_2Se_3 . We propose an experimental signature which is subsequently observed by our experimental collaborators.

» Section 1 of this chapter is unpublished, to appear in Ref. (iv), while Section 2 is published in Ref. (iii).

Effects of correlations in highly degenerate surface states

Chapter 6 deals with the emergent physics on the surface of three-dimensional NCSs, once topological surface states are present. It is well established that high degeneracy is generally unstable to even the smallest interactions, however, lifting the degeneracy of topological flat bands must be accompanied with a local change in the symmetry class. In this chapter we discuss the microscopic mechanism for such an effect and determine the spontaneous symmetry breaking at the surface using self-consistent mean-field calculations.

» This chapter is unpublished, to appear in Ref. (v).

Topology of interacting fermions

Chapter 7 includes a general discussion on the effect of interactions in fully gapped bulk topological insulators and superconductors. We show that the Bott periodicity of non-interacting topological phases is violated, due to the possibility of connecting different topological sectors adiabatically through strongly interacting regions. This reduction is, however, only possible with the presence of a large number of degenerate surface bound states. Effects of interactions on semi-metals and nodal superconductors such as nodal NCSs will be the subject of further research, and falls out of the scope of this thesis.

» This chapter is unpublished, to appear in Ref. (vi).

List of publications

This thesis comprises three published articles, and three others currently in the process of publication:

- (i) Hofmann, J. S., Queiroz, R. and Schnyder, A. P., *Theory of quasiparticle scattering interference on the surface of topological superconductors*. Phys. Rev. B 88, 134505 (2013).
- (ii) Queiroz, R. and Schnyder, A. P., *Stability of flat-band edge states in topological superconductors without inversion center*. Phys. Rev. B 89, 054501 (2014).
- (iii) Queiroz, R. and Schnyder, A. P., *Helical Majorana surface states of strongly disordered topological superconductors with time-reversal symmetry*. Phys. Rev. B 91, 014202 (2015).
- (iv) Queiroz, R., Landolt, G., Muff, S., Slomski, B., Schmitt, T., Strocov, V., Hoffman, P., Osterwalder, J., Schnyder, A. P. and Dil, J. H., *Sputtering induced re-emergence of the topological surface state in Bi₂Se₃*. Submitted, arXiv:1512.06068.
- (v) Queiroz, R. and Schnyder, A. P., *Time-reversal symmetry breaking on the surface of nodal topological superconductors*. In preparation.
- (vi) Queiroz, R., Khalaf, E. and Stern, A. *Classification of interacting fermionic phases by dimensional reduction*. Submitted, arXiv:1601.01596.

1. Theoretical background

1.1. Topological phases of matter

Topological phases of matter are characterized by global rather than local order parameters, and are consequently robust to local perturbations. The global order parameters are commonly called *topological invariants*, which label the adiabatically disconnected sectors from the space of possible Hamiltonians with a given symmetry and dimension. In short-range entangled topological phases, this invariant corresponds to the number of modes localized at the interfaces between two phases with distinct topological numbers. This is a much celebrated result referred to as *bulk-boundary correspondence* [9, 10, 18].

Topological phases such as the one described above are denoted *symmetry protected topological phases* (SPTs), evident by integer (as opposed to fractional) bulk excitations. Their topological classification can be determined in terms of effective single-particle Hamiltonians, and their topological character is fully determined by the characterization of their boundary excitations.

Many subjects such as unconventional superconductivity were revisited with a renewed focus on their topological nature, resulting in a clearer and simpler message. The topological theory of band insulators, such as Bi_2Se_3 or HgTe received in the last years a remarkable amount of attention, since the boundary states were experimentally observed in both photoemission [19–28] and transport experiments [29].

A simple illustration of a topological phase is found for a chain of dimerized electrons, the Su-Schrieffer-Heeger (SSH) model [30], created with the original purpose of describing electronic properties of polyacetylene. Consider a one-dimensional chain with hopping terms t and t' , alternating between adjacent lattice sites. An insulating state can be formed by letting $t' \rightarrow 0$, which will lead to a fully dimerized chain where the electron wave functions are localized but shared between two sites coupled by the amplitude t . An equivalent construction can be made by letting $t \rightarrow 0$ instead, which will lead to a system in everything equivalent to the previous one in the presence of periodic boundary conditions. They belong, however, to different topological sectors, as there is no smooth and adiabatic transformation between the two states. An interpolation between the two sectors would necessarily cross the point $t = t'$ for which the eigenstates are extended through the entire wire. From the discussion

above, we expect additionally that the two sectors of the SSH model host a different number of edge bound states. Let's look now at the finite chain by removing the periodic boundaries. Assume the first site is coupled to the second by t , the second to the third with t' and so on. Letting $t \rightarrow 0$ leaves the first site of the chain disconnected, hence, adding an electron to this site costs no energy. On the other hand if $t' \rightarrow 0$, such a state would not exist, as the end of the chain contains a full dimer. The two sectors, besides being adiabatically disconnected from each other, are distinguished by the existence of an ingap edge state.

Each of the topological sectors has a different number of boundary excitations protected by chiral symmetry. An adiabatic path between the two sectors which preserve chiral symmetry is, therefore, forbidden. In order to facilitate the study of adiabaticity in Bloch systems we introduce the concept of *Berry phases* [31]. For a cyclic loop in some parameter space, for example the lattice momentum k , the wave-function acquires a well defined geometric phase, which can only change under non-adiabatic path deformations — it is a topological invariant. The Berry phase can be expressed as the integral along a closed path of the Berry vector potential determined by the systems eigenstates, being the basis to define the different topological invariants arising both in gapped and gapless SPT phases. For trivial systems, we can impose a constant phase for all eigenstates by a smooth gauge transformation. On the other hand, a nonzero Berry phase for a closed loop evidences an obstruction in choosing a common phase along the loop. A look into the geometric properties of each symmetry class and dimension, allows one to exhaustively determine the possible topological invariants [32, 33]. In Table 1.1 this classification is summarized, where two different topological invariants arise in the context of single particle Hamiltonians: (i) \mathbb{Z} invariants, refer to an integer ($2\mathbb{Z}$ if even) number of disconnected topological sectors within the same symmetry class, allowing for an integer number of perfectly conducting boundary modes. The classic example is the QHE (class A), for which varying the magnetic field strength can lead to a topological phase transition. In a topological phase, or a quantum Hall plateau, an integer number of chiral charge modes are present on the edge, with a conductance of $\sigma = C e^2/h$ with $C \in \mathbb{Z}$, the topological invariant known as Chern or TKNN number [34]. (ii) \mathbb{Z}_2 invariants which refer to systems with only two distinct topological sectors, where a single boundary mode is protected. The most common examples are 2 and 3D topological insulators (class AII).

In closing, it is important to note that in their most general form, topological phases are not constrained to the conditions mentioned above. Strongly correlated topological phases can have fractionalized bulk excitations and long range entanglement. This is the case, for example, of the fractional Hall effect, for which the bulk shows *topological order* [35, 36] and ground state degeneracy for periodic boundaries. Such phases are a fascinating subject, however fall out of the scope of this thesis.

1.1.1. Symmetry classes

The set of symmetries $\{\mathcal{G}\}$ of an Hamiltonian \mathcal{H} can be used to identify and characterize a general system, as it determines the relevant conservation laws and quantum numbers. For example, translational symmetry in both space and time leads to the conservation of momentum and energy. A symmetry is defined by an operator \mathcal{G} , which leaves the Hamiltonian invariant, i.e.,

$$\mathcal{G}\mathcal{H}\mathcal{G}^{-1} = \mathcal{H}. \quad (1.1)$$

For the majority of symmetry operations in physics, \mathcal{G} represents a unitary linear map, i.e., $\mathcal{G}i\mathcal{G}^{-1} = i$. In this category are included Lorentz transformations, gauge symmetries, mirror symmetries, etc. However, they do not constitute the full set of physically relevant symmetries. Symmetry operations respecting $\mathcal{G}i\mathcal{G}^{-1} = -i$ are also allowed and imply strong constraints on the form of the Hamiltonian \mathcal{H} . An antiunitary symmetry \mathcal{G}_{au} can always be written as $\mathcal{G}_{\text{au}} = \mathcal{G}_{\text{u}}\mathcal{K}$, where \mathcal{K} represents complex conjugation and \mathcal{G}_{u} a unitary symmetry.

A key difference between unitary anti-unitary transformations is that the latter does not preserve (anti)commutation relations [37], which is explicitly seen by

$$[r_i, i\partial_{r_j}] = \delta_{ij} \xrightarrow{\mathcal{K}} [r_i, i\partial_{r_j}] = -\delta_{ij}, \quad (1.2)$$

where r is the position and $k = i\partial_r$ the momentum operators. If \mathcal{K} is a symmetry of the Hamiltonian, it must be real $\mathcal{H}^* = \mathcal{H}$, which is the case for integer spin system symmetric under reversal of time. Generally, time-reversal symmetry (TRS) can be written as $\mathcal{T} = \mathcal{G}_T\mathcal{K}$, for \mathcal{G}_T a unitary symmetry. Applying TRS twice, one concludes that either $\mathcal{T}^2 = +1$ or $\mathcal{T}^2 = -1$. While $\mathcal{T}^2 = +1$ concerns integer spin particles, $\mathcal{T}^2 = -1$ is related with half-integer spin particles, where TRS flips the spin degree of freedom. Schematically, we have for spinless and half-spin fermions,

$$\mathcal{T}^2 = +1 : c_{\mathbf{k}}^\dagger \xrightarrow{\mathcal{T}} c_{-\mathbf{k}}^\dagger, \quad (1.3a)$$

$$\mathcal{T}^2 = -1 : c_{\mathbf{k}\uparrow}^\dagger \xrightarrow{\mathcal{T}} c_{-\mathbf{k}\downarrow}^\dagger, \quad \text{and} \quad c_{\mathbf{k}\downarrow}^\dagger \xrightarrow{\mathcal{T}} -c_{-\mathbf{k}\uparrow}^\dagger, \quad (1.3b)$$

where $c_{\mathbf{k}\sigma}^\dagger$ represents the fermionic creation operator. Analogously, we can define a different antiunitary operation \mathcal{C} which arises in the context of particle-hole symmetric (PHS) Hamiltonians, here we can define

$$\mathcal{C}^2 = +1 : c_{\mathbf{k}}^\dagger \xrightarrow{\mathcal{C}} c_{-\mathbf{k}}, \quad (1.3c)$$

$$\mathcal{C}^2 = -1 : c_{\mathbf{k}1}^\dagger \xrightarrow{\mathcal{C}} c_{-\mathbf{k}2}, \quad \text{and} \quad c_{\mathbf{k}2}^\dagger \xrightarrow{\mathcal{C}} -c_{-\mathbf{k}1}, \quad (1.3d)$$

where c_{kn}^\dagger and c_{kn} are the fermionic creation and annihilation operators with n an isospin (band) index [38]. These cases emerge in the context of triplet and singlet superconductors, respectively.

With the two antiunitary symmetry operations we construct a total of ten different symmetry classes of Hamiltonians \mathcal{H} , coined in the literature as the *ten-fold way* [39, 40]. Two complex classes (A, AIII) with no TRS or PHS but possibly satisfying the combination $S = \mathcal{TC}$, denoted chiral symmetry; and eight real classes (AI, BDI, D, DIII, AII, CII, C, CI) with TRS and(or) PHS, squaring to $+1$ or -1 according to the discussion above. The last eight classes can be conveniently represented by an 8-hour clock [41], found in Figure 1.3.

Matrix Hamiltonians

In non-interacting systems, \mathcal{H} can be expressed in terms of a first-quantized matrix Hamiltonian H_{ij} defined by

$$\mathcal{H} = \sum_{\mathbf{k}} \Psi_i^\dagger(\mathbf{k}) H_{ij}(\mathbf{k}) \Psi_j(\mathbf{k}), \quad (1.4)$$

where (i, j) are general indices for real space or internal degrees of freedom, whose summation is assumed if repeated. H_{ij} acts on the fermionic basis states, Ψ_i , which obey the standard fermionic anticommutation relation $\{\Psi_i, \Psi_j^\dagger\} = \delta_{ij}$. In the language of first quantization, the symmetry operators \mathcal{T} , \mathcal{C} and S are represented by the matrix operators

$$\mathcal{T} = U_T \mathcal{K}, \quad \mathcal{C} = U_C \mathcal{K}, \quad S = \mathcal{TC}, \quad (1.5)$$

which can be applied either to the matrix Hamiltonian H or to the basis states Ψ . We note that the unitary matrix S respects $S^2 = 1$ but is not uniquely defined. For the sake of convention let us define this action explicitly,

$$\begin{aligned} \mathcal{T} : \mathcal{T} \Psi_i(\mathbf{k}) \mathcal{T}^{-1} &= (U_T)_{ij} \Psi_j(-\mathbf{k}), \\ \mathcal{C} : \mathcal{C} \Psi_i(\mathbf{k}) \mathcal{C}^{-1} &= (U_C^*)_{ij} \Psi_j^\dagger(-\mathbf{k}), \\ S : S \Psi_i(\mathbf{k}) S^{-1} &= (S)_{ij} \Psi_j^\dagger(\mathbf{k}), \end{aligned} \quad (1.6)$$

and

$$\begin{aligned} \mathcal{T} : U_T^\dagger H^*(-\mathbf{k}) U_T &= +H(\mathbf{k}), \\ \mathcal{C} : U_C^\dagger H^*(-\mathbf{k}) U_C &= -H(\mathbf{k}), \\ S : S^\dagger H(\mathbf{k}) S &= -H(\mathbf{k}). \end{aligned} \quad (1.7)$$

Table 1.1. Topological classification of non-interacting fermion phases characterized by the topological dimension $\delta = d - D_{\text{def}}$. d labels the total dimension of the Brillouin zone, and D_{def} labels the co-dimension of the defect (either in real or momentum space), zero for gapped systems without any defects. The different rows indicate the symmetry class, defined by the transformation of the Hamiltonian under the action of \mathcal{T} (time-reversal symmetry) and \mathcal{C} (particle-hole symmetry) squaring either to $+1$, -1 or absent, 0 . Each entry of the table shows the group of topologically distinct sectors, where \mathbb{Z} signifies distinct integer invariants; $2\mathbb{Z}$ integer and even topological invariants; \mathbb{Z}_2 binary invariants, i.e. "topological" or "trivial"; and 0 which means a single topological sector – the trivial one.

class	\mathcal{T}	\mathcal{C}	\mathcal{S}	$\delta=1$	$\delta=2$	$\delta=3$	$\delta=4$	$\delta=5$	$\delta=6$	$\delta=7$	$\delta=8$	name
A	0	0	0	0	\mathbb{Z}	0	\mathbb{Z}	0	\mathbb{Z}	0	\mathbb{Z}	unitary
AIII	0	0	1	\mathbb{Z}	0	\mathbb{Z}	0	\mathbb{Z}	0	\mathbb{Z}	0	ch-unitary
AI	+1	0	0	0	0	0	$2\mathbb{Z}$	0	\mathbb{Z}_2	\mathbb{Z}_2	\mathbb{Z}	orthogonal
BDI	+1	+1	1	\mathbb{Z}	0	0	0	$2\mathbb{Z}$	0	\mathbb{Z}_2	\mathbb{Z}_2	ch-orthogonal
D	0	+1	0	\mathbb{Z}_2	\mathbb{Z}	0	0	0	$2\mathbb{Z}$	0	\mathbb{Z}_2	BdG
DIII	-1	+1	1	\mathbb{Z}_2	\mathbb{Z}_2	\mathbb{Z}	0	0	0	$2\mathbb{Z}$	0	BdG
AII	-1	0	0	0	\mathbb{Z}_2	\mathbb{Z}_2	\mathbb{Z}	0	0	0	\mathbb{Z}	symplectic
CII	-1	-1	1	$2\mathbb{Z}$	0	\mathbb{Z}_2	\mathbb{Z}_2	\mathbb{Z}	0	0	0	ch-symplectic
C	0	-1	0	0	$2\mathbb{Z}$	0	\mathbb{Z}_2	\mathbb{Z}_2	\mathbb{Z}	0	0	BdG
CI	+1	-1	1	0	0	$2\mathbb{Z}$	0	\mathbb{Z}_2	\mathbb{Z}_2	\mathbb{Z}	0	BdG

TRS and PHS lead to complex conjugation of the first-quantized Hamiltonian H , and correspondingly to the reversal of the momentum direction. It is also customary to refer to \mathcal{T} and \mathcal{C} as reality conditions.

Finally, we note that the role of unitary symmetries should not be underestimated. Particularly, in the light of recent interest rise on topological crystalline insulators (TCIs) [42, 43]. Unitary symmetries can have a defining role on the topological nature of a given material by preventing sectors of opposite topological invariants to couple.

1.1.2. Topological classification of matrix Hamiltonians

A good understanding of a phenomenon comes from the ability to describe it in many different ways, as Feynman would say. The classification scheme of TIs and TSCs is a good example. From the symmetry restrictions above mentioned, there are a few ways to exhaustively determine the topological nature of general matrix Hamiltonians. Originally, the result was obtained by the symmetry constrains on arbitrary Hamiltonians in the context of transport in disordered systems [33], where topological terms were found to prevent

Anderson localization at the boundaries. The same result was then obtained from purely algebraic considerations, specifically by studying the periodic properties of K-theory and group cohomology [32, 44]. A comprehensive description of the classification procedure and the dimensional generalization using Dirac Hamiltonians by Ryu *et.al.* [40] will be the basis for this discussion. The main goal of this section is to introduce a unified background for the treatment of both fully gapped and partially gapped band Hamiltonians. This will serve as the basis for the extension to interacting fermions in the last chapter of this thesis. For a formal construction of Dirac representatives and their dimensional hierarchy the reader is referred to Refs. [40, 45].

Given a symmetry class and a spatial dimension d , topologically distinct Hamiltonian sectors are defined by equivalence classes of Hamiltonians that can be adiabatically deformed onto each other. That is, smoothly transformed into each other without a gap closing. These sectors are symmetry protected since a symmetry breaking term can adiabatically connect two topologically distinct sectors [46].

In fully gapped Hamiltonians, such as insulators and superconductors without nodes, the adiabaticity requirement means the bulk gap should not close during the entire transformation, while for partially gapped systems it means that the Fermi surface manifold can only be continuously deformed, without undergoing a Lifshitz transition. Since adiabatic transformations are allowed, a convenient way to study the topological character of different symmetry classes is by performing an adiabatic transformation from a general Hamiltonian into a Dirac Hamiltonian, for which the momentum dependence is kept only to linear order,

$$H(\mathbf{k}, r) = \sum_a^d k_a \Gamma^a + \mathcal{M}(\mathbf{k}, r), \quad (1.8)$$

for $a = \{1, \dots, d\}$, where Γ^a are generalized Dirac matrices belonging to the spinor representation of $SO(2n + 1)$, which satisfy the anti-commutation relation

$$\{\Gamma^a, \Gamma^b\} = 2\delta_{ab}, \quad (1.9)$$

and $\mathcal{M}(\mathbf{k}, r)$ a general mass with matrix structure, formed by a single or a product of Γ -matrices. For $SO(3)$, the Dirac matrices reduce to the familiar Pauli matrices σ^a with $a = \{x, y, z\}$, from which any 2×2 Hamiltonian can be built. Dirac Hamiltonians of the form (1.8) are not sufficient to describe a big part of physical systems but are sufficient to capture the geometric properties leading to topological features. Another difficulty is that Dirac Hamiltonians are unbound in energy, for this reason they can only describe effective low-energy Hamiltonians, in contrast with tight-binding models defined on a lattice. It follows

that a single Dirac fermion cannot be defined on a lattice, formally described by the *fermion doubling theorem* [47]. In the following, we focus our discussion on the topological properties in the continuum limit, that is $\mathbf{k}_i \in \mathbb{R}^d$, and infer results for a tight-binding Hamiltonian by considering the regularization $k_i \rightarrow \sin(\tilde{k}_i)$, where $\tilde{k}_i \in [-\pi, \pi[$ belongs to the first Brillouin zone (BZ).

As a first remark, let us note that any trivial gapped Dirac Hamiltonian can be continuously deformed into the atomic limit, where the gap is taken to infinity and the electronic states are localized around the lattice ions. The topology must be evident in the momentum dependence of the wave functions, in particular how their geometric character changes by varying \mathbf{k} . Furthermore, we can only define gauge invariant properties of a gauge field within closed boundaries. Thus, the Berry phase is defined as the integral of a Berry vector potential (Berry connection) $\mathcal{A}(\mathbf{k})$ over momentum space. In its simplest form, the Berry phase is defined by

$$\varphi = \oint_C \mathcal{A}(\mathbf{k}), \quad \text{with} \quad \mathcal{A}(\mathbf{k}) = -i \sum_{\text{occ. } n} \langle \Psi_n(\mathbf{k}) | \partial_{\mathbf{k}} | \Psi_n(\mathbf{k}) \rangle, \quad (1.10)$$

where the sum is taken over occupied bands labeled by n . $\mathcal{A}(\mathbf{k})$ is a gauge field in parameter space analogous to a magnetic vector potential from which a magnetic flux originates. One can define a gauge invariant quantity, the Berry curvature $\mathcal{F}(\mathbf{k})$, given in two-dimensions by $\mathcal{F}(\mathbf{k}) = \partial_{k_x} \mathcal{A}_y(\mathbf{k}) - \partial_{k_y} \mathcal{A}_x(\mathbf{k})$. A non-zero Berry phase is therefore associated with the existence of magnetic monopoles, or singularities in the Berry curvature. In other words, it evidences an obstruction in defining a smooth gauge in the full space, quite like trying to comb a hairy ball. The integral of $\mathcal{F}(\mathbf{k})$ over a closed surface does not depend locally on the integration path, however it can vary globally by enclosing a different number of singularities. This is saying that paths giving the same Berry phase φ are homotopically equivalent as they can be smoothly deformed into each other.

Before introducing the general features of Table 1.1, let us understand it by focusing on the specific example of real classes with $d = 1$ ($\delta = 1$). In one-dimension the space is parametrized by a single momentum $\mathbf{k} = k$, and following the general form of a Dirac Hamiltonian defined above, the only two irreducible Hamiltonians one can write are given by

$$H^{\text{BDI}} = k\sigma^1 + m\sigma^2, \quad (1.11a)$$

$$H^{\text{CII}} = k\gamma^1 + im\gamma^2\gamma^3\gamma^4, \quad (1.11b)$$

where γ^i are the *gamma*-matrices forming the irreducible representation of $SO(5)$, and $k \in \mathbb{R}$ as we are considering the continuum limit. The symmetry classes of both Hamiltonians

can be inferred by the missing Dirac matrices. In particular they are both chiral symmetric with $S = \sigma^3$ and $S = \gamma^5$, respectively. Eq. (1.11a) belongs to the class BDI, where TRS is given by $\mathcal{T} = \sigma^1 \mathcal{K}$ and PHS by $\mathcal{C} = \sigma^2 \mathcal{K}$, both squaring to $+1$. While (1.11b) belongs to class CII with $\mathcal{T} = i\gamma^1 \mathcal{K}$ and $\mathcal{C} = -i\gamma^2 \gamma^3 \gamma^4 \mathcal{K}$ squaring to -1 , which leads to doubly degenerate eigenstates (singlet superconductors). The Berry phases associated with the filled bands $E < 0$ are then $\varphi^{\text{BDI}} = \pi/2$ and $\varphi^{\text{CII}} = \pi$. That is, the phase winds around W times along the integration path, with $W = 1$ and $W = 2$ respectively. Let us do the calculation explicitly for the BDI case:

$$\psi(E, \phi) = \frac{1}{\sqrt{2}} \begin{pmatrix} e^{i\phi} \\ 1 \end{pmatrix}, \quad \text{with} \quad \tan \phi = \frac{m}{k}, \quad \text{and} \quad E = \sqrt{k^2 + m^2}, \quad (1.12)$$

the Berry phase is then calculated by

$$\mathcal{A}_\phi = -\frac{m}{2E^2} \Rightarrow \varphi = \int_{-\infty}^{\infty} \mathcal{A}_\phi dk = \frac{\pi}{2}, \quad (1.13)$$

becoming ill defined once the mass gap closes. A lattice regularization forces us to have an even number of Dirac states, each contributing $\varphi = \pi/2$. Thus, we arrive to the general Berry phase of a lattice 1D BDI system, $\varphi^{\text{BDI}} = W\pi \Rightarrow W \in \mathbb{Z}$. The same argument can be applied to (1.11b) to find that $W \in 2\mathbb{Z}$, where the extra factor of two reflects the double degeneracy of the bands in a singlet superconductor. Finally, in the complex classes, no reality condition (\mathcal{T} or \mathcal{C}) is imposed on the eigenstates, hence they are formed by complex fermions, with a higher degree of freedom. Analogous to the BDI case, the Hamiltonian in class AIII takes the same form as (1.11a) with chiral symmetry $S = \sigma^3$ alone. In the absence of reality conditions, Eq. (1.11b) can be brought to a block diagonal form, reflecting the existence of merely two complex classes A and AIII.

The emergence of \mathbb{Z}_2 invariants is more subtle. In this case, TRS or PHS restrict the values of the Berry phase to be $\phi = 0$ or $\phi = \pi$, depending on the existence of an even or odd number of symmetric pairs (each state and its TRS or PHS partner) at high symmetry points in momentum space.

Momentum defects

Materials showing protected stable Fermi points or general momentum space topological defects, owe their exotic properties to the Berry phase acquired by taking a path around these singularities. Among them are Weyl and Dirac semimetals [48–52], whose observation has been reported in TaAs and NbAs, respectively [53, 54], graphene [55] and nodal superconductors (fluids) such as noncentrosymmetric superconductors and the A-phase of

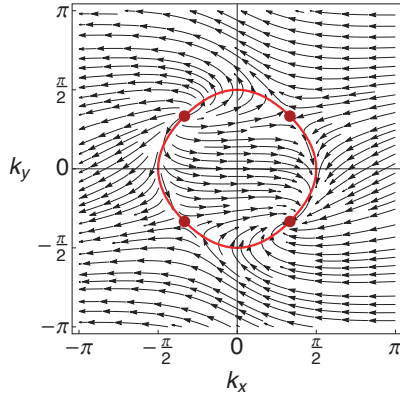


Figure 1.1. Momentum dependence of the Berry phase from a nodal $d_{x^2-y^2}$ -wave superconductor with 4-point nodes marked as dark dots. The normal state Fermi surface is indicated by the solid red line.

^3He [56].

Stable Fermi points and superconducting nodal structures are regions in momentum space, where bands cross and can be viewed as momentum-space defects [56]. Their stability against a trivial gap opening indicates that defects must be protected by a topological invariant. In other words, nodal points in cuprate $d_{x^2-y^2}$ -wave superconductors, Fermi points in graphene and nodal points in the A-phase of ^3He can be interpreted as momentum-space point defects, vortices and hedgehogs, respectively. Nodal lines in noncentrosymmetric superconductors, on the other hand, correspond to momentum-space vortex lines, which can be interpreted as long magnetically charged wires.

Momentum defects are expressed as zeros in the mass function $\mathcal{M}(\mathbf{k})$ in Eq. (1.8), and are thus locally approximated by a massless Dirac Hamiltonian with dimension d_{def} , lower or equal than that of the Brillouin zone. That is, the sum in (1.8) is taken on some subset of possible momentum directions. A defect situated at \mathbf{k}_0 implies that locally the Hamiltonian is described by (1.8) with $\mathcal{M} = 0$, after an appropriate translation that does not change the topological character of $\mathcal{A}(\mathbf{k})$, i.e. that it does not cross any other nodal structure on its way. With a vanishing mass \mathcal{M} , the integral in (1.10) is not well defined for all paths, specifically those that cross the monopole at $\mathbf{k} = 0$. It becomes important to define lower dimensional paths that do not cover the BZ. We define the co-dimension of the momentum defect D_{def} as the difference between the dimension of the space it is embedded in (dimension of the BZ)

and the dimension of the defect d_{def} , that is $D_{\text{def}} = d - d_{\text{def}} - 1$.¹ For example, a Dirac point embedded in a two-dimensional space would have $D_{\text{def}} = 1$. The topological dimension δ characterizes paths that enclose these defects, for which a non-trivial Berry phase can be picked. It follows that $\delta = d - D_{\text{def}}$. This is illustrated in Fig. 1.1, where we see that a non-zero Berry phase can be obtained by taking a contour \mathcal{C} around a nodal point. A parallel can be made with the above calculations of the Berry phase in gapped bands, where the mass is substituted to $m \rightarrow k_{d+1}$. The 1D gapped system has the same topological dimension as a 2D system with point nodes. In the latter case no truly 2D topological invariant can be defined since an integral over the entire BZ is bound to encounter singularities, and is not therefore well defined.

The singularities on the Berry curvature $\mathcal{F}(\mathbf{k})$ can be thought of as sources and sinks of Berry flux. The fermion doubling theorem guarantees that the total flux cancels, that is for each source there is a sink in a different point of the BZ. Moving the Dirac points around and bringing them close together can lead, without violating any symmetry, to their annihilation and a consequent topological phase transition. Due to the change of the topological character of the Fermi manifold, these type of transitions are called *topological Lifshitz transitions*.

The calculation of the Berry phase along a one-dimensional loop around a Dirac cone belonging to the symmetry class AIII (see Table 1.1) is then completely analogous to the one above. In this symmetry class we simply have chiral symmetry, corresponding to a sublattice symmetry such as in ideal graphene (without second neighbour hopping or sublattice asymmetries). A single Dirac cone can be effectively described by

$$H = k_x \sigma^1 + k_y \sigma^2, \quad (1.14)$$

with eigenstates given by (1.12) where $\tan \phi = k_y/k_x$ and $k = \sqrt{k_x^2 + k_y^2}$. The Berry vector potential, for which only the angular component survives is given by

$$\mathcal{A}_\phi(k) = -ik^{-1} \langle \psi(\phi) | \partial_\phi | \psi(\phi) \rangle = (2k)^{-1}, \quad (1.15)$$

leading to a Berry phase of $\varphi = \pi$ i.e., $W = 1$. A Dirac point of opposite chirality, for example $H = k_x \sigma^1 - k_y \sigma^2$, will carry the Berry phase $\varphi = -\pi$ and consequently they can be annihilated by bringing them close enough to one another.

The symmetry class of the Hamiltonian restricted to the integration path is generally not the same as the symmetry class of the full system. In fact, the symmetry classes can only coincide if the paths are taken along high symmetry planes in the BZ. \mathbb{Z}_2 invariants can only protect nodal points ($D_{\text{def}} = 1$) at high symmetry points, since they require a reality

¹The extra “-1” is introduced for convenience, cf. Table 1.1.

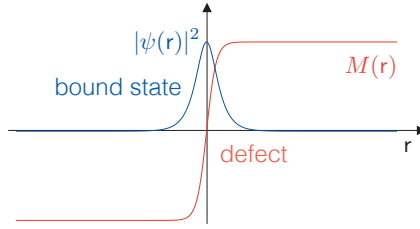


Figure 1.2. Real space defect with a domain wall in the mass function $M(r) \propto \tanh(r)$ (red) trapping a boundary bound state $\psi(r) \propto \text{sech}(r)$ (blue).

condition that necessarily connects opposite momenta. Nodal structures away from high symmetry points in the BZ can therefore only be protected by either no symmetry in even δ (class A) or chiral symmetry in odd δ (class AIII), with \mathbb{Z} invariants.

Spatial defects

To conclude the discussion of basic topological structures in band Hamiltonians, we finally look at spatial defects [41]. These are local regions in real space r where the gap vanishes due to domain walls in the gap function $\mathcal{M}(r)$. Just like in momentum defects, we characterize spatial defects by the co-dimension $D_{\text{def}} = d - d_{\text{def}} - 1$. The topological dimension $\delta = d - D_{\text{def}}$ determines the dimension of the sphere enclosing the defect. As an example, the surface of a 3D bulk material can be parametrized by a 2D domain wall in the mass, written, for example, as $M(r) \propto \tanh(r)$. Bulk-boundary correspondence guarantees that a gapless state exists bound to the defect.

To still be able to define the wave function in k -space, it is assumed that the path is sufficiently far away from the singular defect. Under these conditions, the defect bound state localized in the domain wall of the mass function at $r = 0$ can be obtained by enlarging the Hamiltonian to be written as the irreducible representation of $SO(2N + 1)$ with $N = \lfloor \frac{d+D_{\text{def}}}{2} \rfloor$, such that

$$H^{\text{def}}(r) = i\mathbf{\Gamma} \cdot \partial_r + \tilde{\mathbf{\Gamma}} \cdot \mathbf{M}(r), \quad (1.16)$$

for $\mathbf{\Gamma}^i = (\Gamma^1, \dots, \Gamma^d)$ the real space Dirac matrices, $\tilde{\mathbf{\Gamma}}_i = (\Gamma^{d+1}, \dots, \Gamma^{d+d_{\text{def}}})$ the mass Dirac matrices, and for $\mathbf{M} = (\tanh r_1, \dots, \tanh r_{d_{\text{def}}})^T$. The defect bound state is obtained by solving the equation

$$H^{\text{def}}(r)\tilde{\psi}(r) = 0, \quad (1.17)$$

having the solution²

$$\tilde{\psi}(\tilde{r}) = \prod_{i=1}^{d_{\text{def}}} P_i \operatorname{sech} r_i \psi, \quad P_i = \frac{1}{2}(1 + i\Gamma^i \tilde{\Gamma}^i), \quad (1.18)$$

for ψ a general vector belonging to $SO(N+1)$ and P_i the projector operator for each direction where a domain wall exists. $\tilde{\psi}(\tilde{r})$ is still linearly dispersive along $\tilde{r} = (r_1, \dots, r_{d-d_{\text{def}}})$.

1.1.3. Bott periodicity

The ten-fold way can be directly related to the ten symmetric spaces classified by Élie Cartan in 1926 [57]. The (only) ten different matrix Hamiltonians describing free fermionic systems are in one-to-one correspondence with the ten symmetric spaces in which the time-evolution operator can exist. The existence of such a small number of symmetric spaces indicates that the topological properties of general Hamiltonians should have a simple underlying structure.

In the context of topological band insulators, we restrict ourselves to the classification of fully gapped systems (or fully gapped subsystems), where the $(n+m) \times (n+m)$ matrix Hamiltonian $H(\mathbf{k})$ defined on the BZ has a well defined gap separating the n (below the gap) and m (above the gap) bands. The topological classification can be inferred by flattening the Hamiltonian into a matrix $Q(\mathbf{k})$ with m $E = +1$ and n $E = -1$ eigenvalues [58]. This transformation removes all details of the Hamiltonian, while preserving the possible topological nature of the model. Hence, $Q(\mathbf{k})$ corresponds to a map from the BZ to the classifying space characteristic of each symmetry class.

If there are no symmetries imposed on $Q(\mathbf{k})$, as in the symmetry class A, $Q(\mathbf{k})$ corresponds to a unitary matrix, up to basis transformations in the n and m degenerate subspaces. That is, it is an element of $\{Q\} = U(n+m)/(U(n) \times U(m))$. Up to weak topological invariants [18, 59], we can assume \mathbf{k} to take values in the S^δ -sphere rather than a T^δ -torus, for δ the topological dimension, as previously discussed. In this case, classifying $Q(\mathbf{k})$ corresponds to the classification of maps $Q(\mathbf{k}) : S^d \rightarrow \{Q\}$, given by the homotopy group $\pi_d[\{Q\}]$. This has a universal result [58, 60], being \mathbb{Z} for any *even* dimension, while 0 for any odd dimension. The different equivalence classes in even dimensions are labeled by the Chern number, C_δ .

Imposing chiral symmetry S on the above space we get the symmetry class AIII, where the energy spectrum is symmetric about $E = 0$, that is, $n = m$. In the Dirac Hamiltonian language introduced above, this symmetry class emerges when there is a missing Dirac matrix

²One can see that this general solution satisfies (1.17) by noting that $\partial_x \operatorname{sech} x = -\tanh x \operatorname{sech} x$, and using the commutation properties of the Dirac matrices.

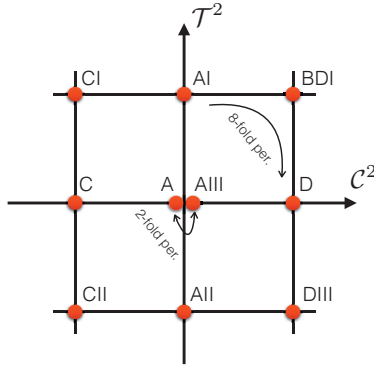


Figure 1.3. Bott clock for the eight real symmetry classes (outer square) and the two complex symmetry classes (center) defined by the antiunitary symmetries \mathcal{T} (time reversal symmetry) and \mathcal{C} (particle-hole symmetry), squaring to $+1$ or -1 . In the presence of TRS and (or) PHS a real condition is imposed in the Hamiltonians, being denoted real symmetry classes and respecting a 8-fold periodicity. In the absence of both TRS and PHS, two complex classes are allowed, with (AIII) and without (A) chiral symmetry, respecting a 2-fold Bott periodicity.

(Γ) in the Hamiltonian, which anticommutes with it. Since the conductance and valence bands are now related by symmetry, $Q(k)$ is simply an element of $U(n)$. The topological classification in this symmetry class is then given by $\pi_d[U(n)]$, which is given by \mathbb{Z} for *odd* dimensions δ , and 0 otherwise. In this case the Chern number vanishes, but we can define an alternative topological invariant to label the different equivalence classes: the winding number W_δ .

An equivalence between $\pi_d[U(n+m)/(U(n) \times U(m))]$ and $\pi_{d-1}[U(n)]$ can be established [44, 61–63], justifying the zig-zag pattern in the first two columns of Table 1.1. This is referred as the two-fold Bott periodicity of complex classes.

Imposing reality conditions in the above spaces, leads to the unfolding the two-fold periodicity into an eight-fold periodicity, as there are eight ways of imposing TRS and PHS. Here, the Chern and winding numbers are still well defined, leading to the ladder of \mathbb{Z} 's in Table. 1.1, in an intercalated way. However, the presence of symmetries connecting the states at k and $-k$ in the BZ leads to the appearance of two descendent \mathbb{Z}_2 invariants, for each of the \mathbb{Z} invariants. In conclusion, the following relation yields

$$\pi_\delta[\{Q\}_s] = \pi_{\delta+1}[\{Q\}_{s+1}], \quad (1.19)$$

where δ labels the topological dimension and s , taken only modulo 2 (8) labels the symmetry

class for complex (real) classes. This is the nature of the Bott periodicity, evident in Table. 1.1 as ladder structures. It can be conveniently represented by an eight hour Bott clock, shown in Fig. 1.3.

1.1.4. Topological invariants

Chern number

In the absence of chiral symmetry, we can define a Chern number, $C(Q_k)$, in terms of the flat Hamiltonian $Q(k)$ given by the projector [40, 58, 64],

$$Q(k) = \mathbb{1} - 2 \sum_{\text{occ. n}} |\psi_n(k)\rangle\langle\psi_n(k)|, \quad (1.20)$$

resulting in

$$C(Q_k) \propto \int_{S^\delta} d^\delta k \epsilon^{\alpha_1, \dots, \alpha_\delta} \text{tr} [Q_k^{-1} \partial_{\alpha_1} Q_k \cdot Q_k^{-1} \partial_{\alpha_2} Q_k \cdots Q_k^{-1} \partial_{\alpha_\delta} Q_k]. \quad (1.21)$$

with ϵ the fully antisymmetric tensor. In a chiral symmetric Hamiltonian, the Chern invariant defined above is always vanishing.

Winding number

The existence of chiral symmetry S , guarantees that the Hamiltonian can be brought to an off-diagonal form in a basis where S is diagonal, denoted *chiral basis*. It follows from the anticommutation of S with the Hamiltonian, that S is a proper unitary symmetry of $H^2(k)$. In this basis we have [40, 58, 64, 65]

$$H(k) = \begin{pmatrix} 0 & D(k) \\ D(k)^\dagger & 0 \end{pmatrix}. \quad (1.22)$$

The eigenstates $\psi_n(k)$ of $H(k)$ can be calculated by diagonalizing $H^2(k)$. We find the conditions

$$D(k)D^\dagger(k)u_n(k) = E_n^2(k)u_n(k), \quad D(k)^\dagger D(k)v_n(k) = E_n^2(k)v_n(k), \quad (1.23)$$

allowing us to rewrite

$$\psi_n(k) = \frac{1}{\sqrt{2}} \begin{pmatrix} u_n(k) \\ \text{sgn}(E_n(k))v_n(k) \end{pmatrix}, \quad (1.24)$$

for $E_n(\mathbf{k})$ the eigenenergies. Performing an adiabatic deformation of the Hamiltonian such that its bands are flattened with eigenvalues $\tilde{E}_n(\mathbf{k}) = \pm 1$, we get

$$Q(\mathbf{k}) = \begin{pmatrix} 0 & q(\mathbf{k}) \\ q(\mathbf{k})^\dagger & 0 \end{pmatrix}, \quad (1.25)$$

with the flattened off-diagonal block

$$q(\mathbf{k}) = \sum_{\text{occ. n}} \frac{1}{E_n(\mathbf{k})} u_n(\mathbf{k}) u_n^\dagger(\mathbf{k}) D(\mathbf{k}). \quad (1.26)$$

Under this transformation, the redundancy introduced by chiral symmetry is removed and the topological character of $H(\mathbf{k})$ is fully encoded in $q(\mathbf{k})$. The winding number, which is only well defined in odd dimensions, takes the general form

$$W(q_{\mathbf{k}}) \propto \int_{S^\delta} d^\delta \mathbf{k} \epsilon^{\alpha_1, \dots, \alpha_\delta} \text{tr} [q_{\mathbf{k}}^{-1} \partial_{\alpha_1} q_{\mathbf{k}} \cdot q_{\mathbf{k}}^{-1} \partial_{\alpha_2} q_{\mathbf{k}} \cdots q_{\mathbf{k}}^{-1} \partial_{\alpha_\delta} q_{\mathbf{k}}]. \quad (1.27)$$

\mathbb{Z}_2 invariants

The reality conditions TRS and PHS applied to the above invariants can lead to their cancellation (for example class AI in two dimensions) resulting in the trivial classification “0”. However, for some symmetry classes TRS or PHS results in the appearance of a binary topological index \mathbb{Z}_2 [40, 64–70]. \mathbb{Z}_2 invariants can be obtained as descendants of Chern and winding \mathbb{Z} invariants at higher dimensions. A detailed derivation can be found, for example, in Ref. [40]. However, simple forms of the invariant can be derived based on Pfaffian indices, well defined in the presence of an antiunitary symmetry squaring to -1 [68, 71]. Since TRS and PHS relate each at \mathbf{k} to a state at $-\mathbf{k}$, it is sufficient to define the \mathbb{Z}_2 index on half of the Brillouin zone, or effective BZ (EBZ). Focusing as an example on the symmetry class AII in two dimensions (spin Hall effect), Kane and Mele [68] have shown that we can define the antisymmetric *sewing matrix* which relates the time-reversal partners,

$$\psi_a(-\mathbf{k}) = [w_{ab}(\mathbf{k})]^* \mathcal{T} \psi_b(\mathbf{k}), \quad \Rightarrow \quad w_{ab}(\mathbf{k}) = \langle \psi_a(-\mathbf{k}) | \mathcal{T} \psi_b(\mathbf{k}) \rangle. \quad (1.28)$$

The existence of a single boundary mode can be inferred by the properties of the sewing matrix at time-reversal invariant momenta (TRIM) in the EBZ (Λ_i), where $|\det[w(\Lambda_i)]| = 1$,

$$N[w] = \prod_i \frac{\text{Pf}[w(\Lambda_i)]}{\sqrt{|\det[w(\Lambda_i)]|}}. \quad (1.29)$$

In the presence of both TRS and PHS, the chiral symmetry operator S guarantees the

above invariant vanishes. This follows from noting that the symmetry operators (1.5) respect $\mathcal{TS} = \alpha S\mathcal{T}$ with $\alpha = \mathcal{T}^2\mathcal{C}^2$. For $\alpha = -1$, as in classes DIII and CI, one can use the anticommutation relation to show that $w(\mathbf{k}) = -w(\mathbf{k}) = 0$. A different topological invariant must be defined in this context. A convenient way to do this is through the off-diagonal structure defined above. In this basis where the flattened off-diagonal block satisfies $q(\mathbf{k}) = -q^T(-\mathbf{k})$ at TRIMs, one can define the analogous \mathbb{Z}_2 index [40, 58, 64, 65]

$$N[q] = \prod_i \frac{\text{Pf}[q(\Lambda_i)]}{\sqrt{\det[q(\Lambda_i)]}}. \quad (1.30)$$

1.2. Disorder

A striking characteristic of topological phases of matter is their intrinsic robustness against local perturbations. These include local uncorrelated or correlated disorder [72]. Boundary modes protected by the topological invariants introduced in the previous section, will remain ballistic even if an impurity is found on their way [9, 10]. This is in clear contrast with normal metallic phases, for which disorder generally leads to diffusion or localization. Here, we introduce the wave function properties of disordered metals, which, in parallel to topological phases, depend crucially on their symmetry and dimension. This is preceded by a discussion contrasting normal metals to metallic boundary modes, which are protected by a bulk topological invariant.

1.2.1. Wave function localization

Classically, the diffusive properties of conducting systems are described by the Boltzmann equation and the Fermi-liquid theory of metals [73]. Charge (or spin) transport can be described by the conductivity σ , limited by scattering events due to electron-phonon or electron-electron interactions. A pioneering work by Anderson [74] introduced the concept of wave-function localization, showing that a strong enough random potential $V(\mathbf{r})$ would lead to a collapse of extended states onto well separated states in space and energy. These localized states decay exponentially in space with the decay rate ξ ,

$$|\Psi(\mathbf{r})|^2 \propto \exp\{-(\mathbf{r} - \mathbf{r}_0)/\xi\}. \quad (1.31)$$

For moderate disorder, however, the possibility of having both localized and extended states arises, as low-energy eigenstates become less affected by a strongly fluctuating disorder potential. The energy below which all states are extended is called the *mobility edge*. The metal to insulator transition driven by disorder can be understood in terms of a single parameter scaling, $\beta(g) = d(\ln g)/d(\ln L)$, where g is the dimensionless conductance and L^d the system size in d -dimensions. This celebrated work by the ‘‘gang of four’’ [75] evidences the critical role of dimensionality in transport. The scaling of the conductance can be computed for a metal and an insulator, which correspond to the so-called diffusive and localized regimes, respectively.

$$g(L) \propto \sigma L^{d-2}, \quad \text{diffusive regime,} \quad (1.32a)$$

$$g(L) \propto \exp\{-L/\xi\}, \quad \text{localized regime,} \quad (1.32b)$$

One can immediately conclude that in one-dimension $d = 1$, all states are localized and consequently, no metallic state can exist. In two dimensions, the critical dimension, one cannot make a concrete statement about the localization of the states. Finally, in three dimensions a metal-insulator transition is expected to happen, for a for a critical value of the conductance g_c .

This picture is, however, very simplified. The effect of quantum fluctuations becomes critically important in order to predict if a metal-insulator transition occurs. In particular, a logarithmic correction to the conductivity can emerge due to such interference effects. In a perturbation theory language, different quasiparticle paths can interfere constructively or destructively, according to the symmetry constraints on the single-particle propagators. This effect is called *weak (anti-)localization*. Such corrections become particularly important in two-dimensions, where (1.32) does not provide sufficient information. In the presence of time-reversal symmetry breaking terms, such as an applied magnetic field, the destructive interference due to self-crossing diagrams of a 2D electron gas is lifted, leading to the experimentally observed negative magnetoresistance [76], a puzzling result that deeply shows the importance of quantum interference to the total conductivity.

Furthermore, in this analysis the effects of topological protection are not accounted for, where Anderson localization can be fully avoided [58, 77]. In particular, the edges of a quantum Hall state are effectively one-dimensional systems that evade localization. At a practical level, one can numerically detect Anderson localized states in a numerical simulation of a lattice Hamiltonian by calculating the participation ratio

$$P(\Psi) = \frac{1}{\mathcal{N}} \frac{\left(\sum_i |\Psi(r_i)|\right)^2}{\sum_i |\Psi(r_i)|^4}, \quad (1.33)$$

where \mathcal{N} is the total number of sites on the lattice and $\Psi(r_i)$ the electron's wave function at a given site. This expression estimates the real-space extension of a given state. Being close to zero for a state that occupies a single site in the lattice (localized state), while close to one for an extended, delocalized state.

1.2.2. Role of symmetry in transport

Quantum localization leads to a Poisson distribution of the spectral spacings, this means that once states get localized they do not feel any repulsion from other localized states, and the universality of the diffusive regime is washed away. Above we mentioned that in two-dimensions breaking TRS leads to an increase in bulk conductivity. It is natural to think that such behavior is tied to both dimensionality and symmetry class of the system in

study. In the following I will very briefly summarize the different symmetry classes that show fundamentally distinct localization properties which coincide with the ten-fold way, described in the previous section [37, 39, 78] (cf. Table 1.1).

Wigner-Dyson symmetry classes

Classes with just TRS are commonly denoted the Wigner-Dyson (WD) classes, or the (*three fold way*) [79]. These classes were the first to be studied and identified to have fundamentally distinct properties, justifying their simple nomenclature A, AI and AII, or unitary, orthogonal and symplectic classes. WD classes are distinguished by the action of TRS, and consequently their description of real, complex or spinful (quaternionic) states. It is a well established experimental fact that the three types of systems differ in their diffusive behavior, and consequently show different transport properties. The scattering elements allowed in a given symmetry class will be translated into a signature in the energy spectrum of a random (chaotic) Hamiltonian. The energy spectrum of a diffusive mesoscopic system can be qualitatively well described by a random Hamiltonian provided the eigenstates span the entire phase space allowed in the symmetry class. A signature of scattering is the avoidance of energy degeneracies, usually denoted by *level repulsion*. The degree of repulsion is measured by the level spacing distribution $P(s)$, given by

$$P(s) \propto s^\beta, \quad \text{for } s \rightarrow 0 \quad (1.34)$$

and showing a Gaussian dependence for large s . Here, β , is determined by the symmetry class of the Hamiltonian H , being linear ($\beta_{\text{AI}} = 1$), quadratic ($\beta_{\text{A}} = 2$) or quartic ($\beta_{\text{AII}} = 4$). The level spacing distributions are universal within each symmetry class, that is, independent of the details of the system provided a large enough statistical sample is studied. This is the foundation of random matrix theory (RMT) [37, 80], asserting the connection between energy level dynamics and maximum entropy in random Hamiltonians, respecting certain symmetry constraints.

Chiral symmetry classes

Adding chiral symmetry to the above classes, means that there exist a matrix S such that $\{H, S\} = 0$. As discussed in Sec. 1.1, in a basis where S is diagonal, the Hamiltonian can be brought to a block off-diagonal form. It follows immediately a energy spectrum of such that the Hamiltonian is symmetric with respect to $E = 0$. In terms of the above discussion, the chiral classes AIII, BDI and CII, or alternatively chiral-orthogonal, chiral-unitary and chiral-symplectic, should have an anomalous behavior around $E = 0$. That is, there will

be an added repulsion exponent for the dependence on the absolute value of the eigenstates, instead of simply the distance between them,

$$P(s, E) \propto s^\beta, \text{ for } s \rightarrow 0, \text{ and } P(s, E) \propto |E|^\alpha, \text{ for } E \rightarrow 0. \quad (1.35)$$

Such variation is small but detectable, as we will see in Chp. 4.

BdG symmetry classes

Altland and Zirnbauer [39, 78] completed the classification of matrix Hamiltonians by identifying the missing Bogliubov-de Gennes classes. Particle-hole symmetry \mathcal{C} emerges in the context of superconducting states as it will be discussed in the following chapter. Here, Andreev scattering allows for coupling between an electron with energy E and a hole with energy $-E$. It is then pertinent to consider a basis that includes both contributions — the Nambu representation, where

$$\Psi = (c, c^\dagger)^T. \quad (1.36)$$

The first-quantized Hamiltonian H acting on Ψ can be decomposed into the BdG form

$$H = \begin{pmatrix} h & \Delta \\ \Delta^\dagger & -h^T \end{pmatrix}, \quad (1.37)$$

where the anomalous term Δ represents the coupling between the two sectors. In this representation, the states Ψ have the intrinsic symmetry

$$(\sigma^1 \Psi)^T = \Psi^\dagger, \quad (1.38)$$

where σ^1 is the first Pauli matrix acting on Nambu space. This condition allows for a basis transformation into a Majorana basis, i.e.,

$$\Gamma = (\gamma^+, \gamma^-)^T = \frac{1}{2}(c + c^\dagger, -i(c - c^\dagger))^T, \quad (1.39)$$

respecting $\gamma^\chi = \gamma^{\chi^\dagger}$, for $\chi = \pm$ the chirality of the Majorana state, defined by $S\gamma^\chi S^{-1} = \chi\gamma^\chi$. Majorana states can be spatially separated from their partners, resulting in a single Majorana state with $E = 0$, which is its own antiparticle $\gamma = \gamma^\dagger$ [81], that is, they are effectively “half” fermions with occupation number $\gamma\gamma^\dagger = 1/2$. The appearance of such unpaired Majoranas affirms the non-trivial topological nature of the bulk system.

As in the chiral classes, BdG classes will result in the correction (1.35) to the level repulsion profile. In Chps. 4 and 5 we will be concerned with the symmetry class DIII, where there is a

correction to the Wigner surmise with $\alpha = 1$ and $\beta = 4$ [37].

1.2.3. Nature of Anderson phase transitions

At the transition from a diffusive to a localized regime (cf. Eq. (1.32)) the system undergoes a metal to insulator transition, characterized by the conductivity σ or the localization length ξ , when approaching from the metallic or insulating side, respectively [77]. The critical scaling followed by both these quantities as they approach the critical point indicates that the Anderson transition is a continuous phase transition [82],

$$\xi \propto (E - E_c)^{-\nu}, \quad \sigma \propto (E - E_c)^s, \quad (1.40)$$

where E_c indicates the mobility edge energy. The critical exponents of the two functions are related by $s = \nu(d - 2)$. It turns out, in contrast with usual phase transitions, Anderson transitions are characterized by not a single but a continuous function of universal exponents. This is usually referred to as multifractality of the wave functions at the Anderson transition critical point [77], where there is no natural length scale associated with the spatial distribution of the wave functions. This leads to a characteristic distribution of the local density of states [83], which can be detected in numerical simulations.

The symmetry and dimension of the wave functions at the critical point dictates the energy dependence of the density of states, which for chiral symmetric Hamiltonians can show a singularity at $E = 0$. This singularity, known as the Dyson singularity [84] in one dimension, results from the increased probability of random states with zero energy at the critical transition. From this singular behavior, one can additionally infer the parity of the scattering channels involved in the transition. That is, the singularity will show a different divergent profile for an even or odd number of channels. In particular, for one-dimensional systems in symmetry class BDI with an odd number of channels, the density of states $\rho(E)$ at the critical value of disorder respects,

$$\rho(E) = |E\tau \ln^3 |E\tau||^{-1}, \quad (1.41)$$

where τ is the average scattering time. In Chp. 4.2 of this thesis, we will observe such singular behavior as disorder is included on the edge of a topological superconductor. The boundary mode assures that the total number of scattering channels at the edge is odd. Even though our results are consistent with this prediction, our numerical method has the drawback of being fundamentally a bulk calculation, making it very hard to resolve small variations in the type of singularity. For this reason, we study the distribution of the wave functions at varying disorder strength to further identify the presence of a critical transition of the Anderson type.

1.2.4. Types of disorder

The effects of disorder on metallic or topological boundary states depends not only on the symmetry and dimension considered but also on the type of disorder [85]. We can imagine that disorder emerges everywhere in the sample as fluctuations of the background electrostatic potential or, conversely, that impurities are dilute but very strong, due to element substitutions or vacancies on the lattice. The different types of disorder will determine the observed density of states, which, in turn, can be experimentally observed by the differential tunneling conductance in scanning tunneling microscopy (STM).

In a tight-binding Hamiltonian, we can define the impurity potential V_q [86],

$$V_q = \frac{1}{\mathcal{N}} \sum_{i=1}^{\mathcal{N}} \sum_{j=1}^N V_0 \delta_{ij} e^{-iq \cdot r_i}, \quad (1.42)$$

for a lattice with \mathcal{N} sites and N impurities. It is convenient to define the density of impurities $\rho_{\text{imp}} = N/\mathcal{N}$, and the probability of having a number of impurities n at a given site i , given by the Poisson distribution,

$$p_{\rho_{\text{imp}}}(n) = \frac{1}{n!} (\rho_{\text{imp}})^n e^{-\rho_{\text{imp}}}. \quad (1.43)$$

The effective disorder strength ζ is then given by

$$\zeta = \rho_{\text{imp}} V_0^2. \quad (1.44)$$

It is therefore convenient to consider two limits:

- i *Gaussian limit* $\rho_{\text{imp}} \approx 1$, and $V_0 \ll T$,
- ii *Unitary limit* $\rho_{\text{imp}} \approx 0$, and $V_0 \gg T$,

where T is the energy scale characteristic of the tight-binding model, that is, the bandwidth. In Chps. 4 and 5 we will encounter evidence for a quite different behavior between these two disorder limits. We will see in particular that Gaussian disorder can interfere with the topological surface states (being even fatal in the absence of chiral or particle-hole symmetry), while unitary disorder generally leads to the burial of the topological states into deeper layers of the sample.

1.2.5. Topology in disordered systems

In Sec. 1.1 we have discussed topological properties of Hamiltonians with well defined momentum \mathbf{k} , i.e., translational invariance was assumed. In the presence of disorder, the

wavefunctions lose their sharply defined momentum and hence the band picture becomes invalid. Concepts such as the band gap become ill defined, and an alternative understanding of the topological character must emerge. After the discovery of the QHE, where the topological nature of a disordered electron gas emerges as quantized values of conductivity through the edges, Laughlin [87] argued that in the presence of disorder a mobility gap emerges around the Fermi level, within which all states are localized. The existence of a topological invariant guarantees that upon threading a flux through an annulus geometry, a charge can be transferred adiabatically from the inner to the outer ring, changing the total polarization by a quantum of charge, and revealing the topological transition from a sector characterized by a Chern number C to one with $C + 1$. These states fall inside the mobility gap and are fully delocalized around the annulus edges. Laughlin's argument for the QHE can be understood for general disorder or interactions that do not constitute an impediment for adiabatic transport. Exceptions to this picture are strong interactions that can lead to ground state degeneracy as in the fractional QHE, or strong disorder that localizes all the states leading to a trivial insulator.

Restating, the dissipationless transport in topological phases is guaranteed by the fact that it is carried through the ground state and there is no change in the occupancy of the different excited states. In a field-theoretical description of the disordered systems, this ground state is guaranteed by the existence of a topological term in the action, which is independent of the details of the bulk system. For completeness, but not diving into details, such terms are denoted Wess-Zumino-Witten (WZW) terms (\mathbb{Z} invariants) and theta (θ) terms (\mathbb{Z}_2 invariants) in the language of the non-linear sigma model describing the disorder averaged transport properties according to the ten symmetry classes. An extensive discussion on Anderson transitions and the role of topological invariants can be found in Ref. [77].

In many ways, disorder can lead to the increased stability of topological phases. The quantum Hall effect owes its existence to disorder, as the energetic difference between boundary and bulk states is accentuated, legitimizing the description of the two in an independent way.

1.2.6. Topology in disordered nodal systems

Topologically protected nodal structures are affected by arbitrarily small amounts of local disorder (small momentum transfer q), as momentum becomes ill defined around the Fermi level. This results in a less sharp dispersion close to the nodal points, which can be understood in terms of a broadening of the single particle Green's function. Despite that, this effect is confined within a small energy window around the nodal points, and the topological invariant is still well defined when evaluating the Berry curvature around, but far enough,

from the nodal structure. If the disorder strength is comparable to the gap magnitude, such an approximation is no longer valid. It is therefore pertinent to study clean bulk systems, where disorder is confined to the surface.

On the other hand, long-range correlated disorder with large q can be destructive to the topological properties of nodal systems. This is in view to the fact that the nodal structures with opposite topological invariants are allowed to couple, becoming topologically trivial and opening a full gap around the node. Restricting the disorder potential to the surface will also avoid this problem, as the q vectors become constrained. We will consider in Chp. 5 the effects of long range disorder by simulating finite size quantum dots with irregular boundaries.

Finally, If the surface disorder is symmetry breaking, a small mobility gap can be opened at the nodal regions. This effect should become negligible as the system size increases and the bulk's wave function become less present on the boundary.

1.3. A very short introduction to superconductivity

1.3.1. BCS superconductivity

Rather than providing an exhaustive description of the many phenomena and models associated with superconductivity, this chapter will focus solely on symmetry aspects of various types of superconductivity, and the topological structures that can emerge. Bardeen, Cooper and Schrieffer [4] have described a superconducting state as paired electrons forming a bosonic condensate. In conventional superconductors (*s*-wave) the glue binding the two fermions can be understood as a retarded charge dislocation in the ionic background caused by a moving electron, which then creates an electrostatic potential that can pull a second electron, creating an effectively attractive interaction between the two. The paired fermions behave like an emergent bosonic excitation, which for low enough temperatures can form a condensate by Bose-Einstein condensation (BEC). Below a critical temperature T_c , the $U(1)$ gauge symmetry is broken, resulting in phase coherence along the sample. A macroscopic quantum state is formed.

Due to the Cooper pair formation, superconductivity results in a symmetry between particle and hole operators, represented by $c_{k\sigma}c_{-k\sigma}^{-1} = c_{-k\sigma}^\dagger$, that is particle-hole symmetry. This symmetry can be explicitly built into the single-particle Hamiltonian by writing

$$\mathcal{H} = \sum_{k\sigma} \left(\varepsilon_k c_{k\sigma}^\dagger c_{k\sigma} - \varepsilon_{-k} c_{-k\sigma} c_{-k\sigma}^\dagger \right), \quad (1.45)$$

where we have imposed a redundancy by identifying a single state with two energy levels $+\varepsilon_k$ and $-\varepsilon_{-k}$ for electron and hole-like parts, respectively. This decomposition is very useful to describe the effect of four-point interactions of the general form

$$\mathcal{H}^{\text{int}} = \frac{1}{2} \sum_{kk'} U_{\sigma\tau\tau'\sigma'}(k, k') c_{k\sigma}^\dagger c_{-k\tau}^\dagger c_{-k'\tau'} c_{k'\sigma'}. \quad (1.46)$$

At the mean-field level, the full Hamiltonian can be re-expressed in the form of a Bogliubov-de Gennes Hamiltonian, already introduced in the context of symmetry constrained random matrices in Sec. 1.2.2,

$$\mathcal{H} = \sum_{kk'} \Psi_k^\dagger \begin{pmatrix} h_k & \Delta_k \\ \Delta_k^\dagger & -h_{-k}^T \end{pmatrix} \Psi_k, \quad (1.47)$$

where $\Psi_k^\dagger = \{c_{k\uparrow}^\dagger, c_{k\downarrow}^\dagger, c_{-k\uparrow}, c_{-k\downarrow}\}$ is the Nambu spinor, h_k the normal state Hamiltonian found in (1.45), which for a tight-binding model in d dimensions with hopping $t/2$ and

chemical potential μ takes the form

$$\varepsilon_{\mathbf{k}} = t \sum_{i=1}^d \cos k_i - \mu. \quad (1.48)$$

The anomalous contribution $\Delta_{\mathbf{k}}$ follows from the opening of a gap around the Fermi level due to the interaction (1.46). The gap opens where the two bands $\varepsilon_{\mathbf{k}}$ and $-\varepsilon_{-\mathbf{k}}$ cross, allowing for the gain of *condensation energy* at the expense of breaking particle number conservation. Δ is a local order parameter given by the expectation value of the pairing amplitude

$$\Delta(\mathbf{k})_{\sigma\tau} = \sum_{\mathbf{k}'\sigma'\tau'} U_{\sigma\tau\tau'\sigma'}(\mathbf{k}, \mathbf{k}') \langle c_{-\mathbf{k}'\tau'} c_{\mathbf{k}'\sigma'} \rangle. \quad (1.49)$$

As originally developed for singlet superconductors, BCS theory is derived from a local interaction that is $U_{\sigma\tau\tau'\sigma'}(\mathbf{k}, \mathbf{k}') \rightarrow U_{\uparrow\downarrow\uparrow\downarrow}$ and consequently $\Delta_{\mathbf{k}} \rightarrow \Delta$, without a momentum dependence. Since the total wave function of a Cooper pair must be odd under exchange of its fermionic components, the momentum part of the wavefunction, which is even in k must be combined with a singlet spin wavefunction. We conclude the pairing Hamiltonian is given by

$$\mathcal{H}_{\Delta}^{\text{MF}} = \sum_{\mathbf{k}} \Delta c_{\mathbf{k}\uparrow}^{\dagger} c_{-\mathbf{k}\downarrow}^{\dagger} + \text{h.c.} \quad (1.50)$$

1.3.2. Unconventional superconductivity

Allowing for a pairing mechanism that is more general than the phonon-mediated one, the pairing symmetry is no longer bound to form an isotropic s -wave singlet state. In particular, once interactions can be of longer range, Cooper pairing is allowed for higher angular momentum channels, eventually with nodal structures [16]. Moreover, the Cooper pairs can carry a magnetic moment, breaking time reversal symmetry, for example by forming a spin-triplet and pairing through an odd function of momentum. In both cases, the pairing is “exotic” in the sense that it has lower symmetry than the normal state Hamiltonian, belonging not to the trivial, but to higher representations of the system’s point group \mathcal{G}_{pg} . It also highlights that the analogy to simple BEC fails, as Cooper pairs, in contrast with normal bosons, carry internal degrees of freedom [88].

Let us imagine the case of Cooper pairs forming a spin-triplet state. Then the orbital part, $\Delta(\mathbf{k})$ must be odd under exchange. With these conditions we can write a p -wave

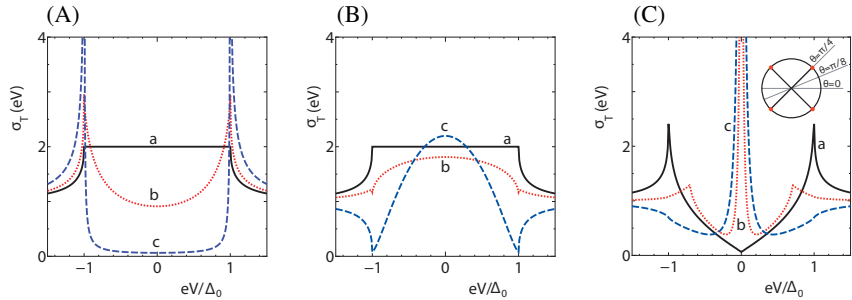


Figure 1.4. Figure adapted from Ref. [93]. (A)-(B) Tunnelling conductance dI/dV at various barrier strengths Z (a: $Z = 0$, b: $Z = 1$ and c: $Z = 5$) for a topological trivial s -wave superconductor (A) and a topological $(p_x + ip_y)$ -wave superconductor with a chiral edge state inside the gap (blue, c). (C) Tunnelling conductance dI/dV at $Z = 5$ for a topological $d_{x^2-y^2}$ -wave superconductor, showing flat band edge states leading to a zero bias conductance peak at surfaces oriented with angles (b) $\theta = \pi/8$ and (c) $\theta = \pi/4$, while not showing any state at the nodal direction $\theta = 0$ (black, a).

superconductor

$$\mathcal{H}_{\Delta}^{p+ip} = \sum_{\mathbf{k}} \Delta(k_x + ik_y) c_{\mathbf{k}\uparrow}^{\dagger} c_{-\mathbf{k}\uparrow}^{\dagger} + \text{h.c.} \quad (1.51)$$

Such a system breaks explicitly TRS, belonging to the symmetry class D, as shown in Table. 1.1 it can host non-trivial topological phases. Class D includes the one-dimensional p -wave superconductor with Majorana bound states and the two-dimensional $(p_x + ip_y)$ -wave superconductor which allows for propagating chiral edge modes, leading to the appearance of a broad peak in the ingap region of the surface density of states, see Fig. 1.4(B). Majorana fermions in one-dimensional systems have been engineered by inducing superconductivity in semiconductor wires by proximity to a conventional superconductor [89]. Transport experiments show indeed a zero-energy peak when the wire is in a topological phase, however the results are still the subject of heavy discussion. Another approach is the creation of magnetic impurity chains on top of a superconductor, effectively obtaining a p -wave superconductor at the interface between the chain and the superconductor. Scanning tunneling microscopy (STM) on this heterostructure shows a peak at zero energy [90] localized on the wire ends, leading to the same interpretation. For the two-dimensional case, some experimental evidence show that strontium ruthenate Sr_2RuO_4 is a candidate to show such chiral edge modes without any applied external field [91, 92]. However, a direct observation of the edge states continues to be sought after.

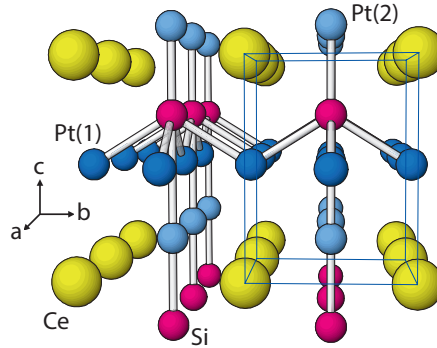


Figure 1.5. Adapted from Ref. [94]. Crystal structure of CePt_3Si . The bonds indicate the pyramidal coordination $[\text{Pt}_5]\text{Si}$ around the Si atom. The evident lack of inversion symmetry along the c -axis creates a strong crystal field leading to strong asymmetric spin-orbit coupling.

An example of a pairing state that preserves TRS but with a higher angular momentum wavefunction occurs in the cuprate high temperature superconductors (high- T_c SC) for which the pairing is known to be of $d_{x^2-y^2}$ -wave type. That is, the pairing function can be written as

$$\mathcal{H}_{\Delta}^{\text{high-}T_c} = \Delta(\cos k_x - \cos k_y)c_{k\uparrow}^{\dagger}c_{-k\downarrow}^{\dagger} + \text{h.c.}, \quad (1.52)$$

with nodal points at the BZ diagonal directions. Each of these points are locally described by a Dirac point which is the source of a Berry flux. The Berry phase as a function of k can be found explicitly in Fig. 1.1.

Historically, the surface states arising from this nontrivial character of the nodal structure, were understood as edge bound states due to Andreev scattering, that is scattering processes that transform holes into electrons and vice-versa at the interface between a superconductor and a normal insulator. A good understanding of these bound states can be obtained through quasiclassical calculations, and were predicted much before restating the problem as a topological phenomenon. A celebrated tunneling experiment on the high temperature cuprate superconductors showed a zero-bias peak due to Andreev bound states only at certain surface orientations, signature of the d -wave character, and the topological nature of its nodal structure [12]. A detailed compilation of experimental results for phase-sensitive measurements in cuprates is found in the chapter by Tsui and Kirtley in Ref. [88]. The expected tunneling conductance can be found in Fig. 1.4 (C).

1.3.3. Noncentrosymmetric superconductors

Noncentrosymmetric superconductors, as the name indicates, are characterized by a lack of inversion center. This condition generally leads to a non-zero crystal field gradient and consequently antisymmetric spin-orbit coupling, $\mathbf{g}(\mathbf{k})$, of Rashba type [16, 95]. Antisymmetric SOC breaks inversion symmetry by imposing $\mathbf{g}(\mathbf{k}) = -\mathbf{g}(-\mathbf{k})$, and, consequently, renders parity ill-defined in the system. In the presence of this type of spin-orbit coupling, the normal state Hamiltonian is given by

$$h(\mathbf{k}) = \varepsilon(\mathbf{k})\sigma^0 + \mathbf{g}(\mathbf{k}) \cdot \boldsymbol{\sigma}. \quad (1.53)$$

It follows that lack of inversion center results in no constraint in the orbital pairing's parity. That being so, an admixture of even and odd pairing parts is allowed. Due to the total odd character of the Cooper pair wave function under exchange of its fermionic components, the symmetry of the order parameter $\Delta(\mathbf{k})$ will necessarily be either even or odd if a Cooper pair is formed in the spin-singlet or spin-triplet channel, respectively. Once inversion symmetry is explicitly broken, it is natural to expect the two to coexist, varying their relative strengths. The gap function $\Delta(\mathbf{k})$ is a combination of both odd and even parity, most conveniently expressed by

$$\Delta(\mathbf{k}) = f(\mathbf{k})(\psi(\mathbf{k})\sigma^0 + \mathbf{d}(\mathbf{k}) \cdot \boldsymbol{\sigma})i\sigma^2, \quad (1.54)$$

with $\boldsymbol{\sigma} = \{\sigma^1, \sigma^2, \sigma^3\}$, $\psi(\mathbf{k})$ the even contribution multiplying the singlet part ($c_{\mathbf{k}\uparrow}^\dagger c_{\mathbf{k}\downarrow}^\dagger - c_{\mathbf{k}\downarrow}^\dagger c_{\mathbf{k}\uparrow}^\dagger$), and $\mathbf{d}(\mathbf{k})$ being the odd pairing with three components, one for each of the three triplet pairing terms ($c_{\mathbf{k}\uparrow}^\dagger c_{\mathbf{k}\downarrow}^\dagger + c_{\mathbf{k}\downarrow}^\dagger c_{\mathbf{k}\uparrow}^\dagger$), ($c_{\mathbf{k}\uparrow}^\dagger c_{\mathbf{k}\uparrow}^\dagger + c_{\mathbf{k}\downarrow}^\dagger c_{\mathbf{k}\downarrow}^\dagger$) and ($c_{\mathbf{k}\uparrow}^\dagger c_{\mathbf{k}\uparrow}^\dagger - c_{\mathbf{k}\downarrow}^\dagger c_{\mathbf{k}\downarrow}^\dagger$). $f(\mathbf{k})$ is an overall form factor encoding the higher angular momentum dependence, e.g., $f(\mathbf{k}) = (\cos k_x - \cos k_y)$ for $d_{x^2-y^2}$ superconductivity. It is worth to notice that in the case of broken inversion symmetry, time-reversal symmetry must be present. This follows from the condition that in the normal state $h(\mathbf{k})$, the Fermi surface must be symmetric upon inversion of momentum \mathbf{k} , achieved by both TRS and inversion symmetry. Without any of these symmetries, the it is not possible to form a zero-momentum Cooper pair and the instability is largely reduced. The vector $\mathbf{d}(\mathbf{k})$ cannot, therefore, break TRS. In the presence of TRS, $\mathbf{d}(\mathbf{k}) \cdot \boldsymbol{\sigma}$ looks a lot like a spin-orbit-coupling term, and in fact, it is quite intimately related. Lack of inversion center leads to the Rashba spin orbit coupling introduced above. Its exact form can be obtained by crystal symmetry restrictions, that is it will depend on the point group \mathcal{G}_{pg} of the material we are considering [16, 66, 96]. A list of possible $\mathbf{g}(\mathbf{k})$ vectors for the various \mathcal{G}_{pg} symmetries can be found in the Appendix A.

The antisymmetric spin-orbit coupling will lift the spin degeneracy of the electronic bands

into helical bands, for which the Bloch wave functions have strongly momentum dependent spin textures. When the system enters a superconducting state, the $\mathbf{d}(\mathbf{k})$ -vector will be parallel to the spin-orbit coupling $\mathbf{g}(\mathbf{k})$ -vector, as it determines the full magnetic character of the electronic wave functions in the normal state. For other $\mathbf{d}(\mathbf{k})$ vector orientations, the spin orbit coupling would have a pair-breaking effect [97]. The strong spin anisotropy of the helical bands will be reflected in the emergent topological boundary modes. These inherit a highly unusual helical spin texture, where the spin direction varies as a function of surface momentum [98–103].

The specific properties of each type of surface state reflect the topological nature of the nodal structure of the superconducting gap. Determining these properties for specific $\mathbf{g}(\mathbf{k})$ and $\mathbf{d}(\mathbf{k})$ vectors will be the focus of Chp. 2.

Fig. 1.5 shows the crystal structure of cerium platinum-3 silicon CePt_3Si , discovered in 2004 [94], which was the first heavy-fermion noncentrosymmetric to be detected. It is a quasi-two dimensional system with a tetragonal point group (C_{4v}), allowing for a Rashba SOC of the form $\mathbf{g}(\mathbf{k}) = k_y \hat{\mathbf{x}} - k_x \hat{\mathbf{y}}$. This is one of many crystals without inversion symmetry that show superconductivity. Below, the most relevant groups of materials showing noncentrosymmetric superconductivity are listed. For a more complete list with crystallographic details and a comprehensive summary of the available experimental data, the reader is referred to the chapter by Bauer and Rogl in [16].

i *Strong electronic correlations*

» Heavy fermion superconductors:

Heavy fermion superconductors are characterized by strong electronic correlations and flat electron dispersions, where Kondo and RKKY interactions become important [104]. Consequently, the pairing mechanism relies solely on electron-electron correlations, and pairing of the s -wave type is disfavored. Strong spin-orbit coupling is expected in these materials, and therefore a helical structure of the Fermi surface. In this category fall the compounds CePt_3Si [94], CeIrSi_3 [105], and CeRhSi_3 [106].

ii *Weak electronic correlations*

» Sesquicarbides:

Carbon based compounds such as Y_3C_3 and La_2C_3 [107] show strong distortions in their unit cells, resulting in strong spin-orbit coupling and multigap structures. However, these systems usually exhibit high-frequency phonon modes which leads to dominant s -wave superconductivity.

» Metallic alloys:

Metallic alloys with extremely large unit cells (composed of $\sim 10^3$ atoms) show strong spin-orbit coupling and an effective cubic structure, however, their weak coupling also leads to dominant s -wave pairing [108].

» $\text{LiPt}_{3-x}\text{Pd}_x\text{B}$ and $\text{Mo}_3\text{Al}_2\text{C}$:

These distorted perovskite compounds show strong signs of unconventional superconductivity with a cubic point group [109–112]. The first compound is particularly interesting as the substitution of Pd atoms for Pt atoms results in a greater distortion due to its larger radius. Remarkably, this substitution allows to tune the SOC strength from 30 meV for LiPd_3B up to 200 meV in LiPt_3B [16]. The latter shows a linear temperature dependence in the London penetration depth, compatible with nodal structures [109], and has a distinctly smaller T_c .

» BiPd:

Bismuth paladium attracted some enthusiasm as evidence for a multigap structure appeared in the literature [113, 114]. However, these results are in contradiction with more recent STM measurements, where a BCS gap is observed [115]. Nonetheless, the strong SOC anisotropy leads to a surface Dirac state in the normal regime, and in the presence of superconductivity zero-energy bound states emerge trapped in vortices, possibly indicating Majorana fermions.

iii *Heterostructures*

Two-dimensional topological superconductors can also be engineered in heterostructures [116, 117], for example, by depositing a material with strong SOC on a conventional s -wave superconductor. Moreover, strong evidence indicates that the $\text{LaAlO}_3/\text{SrTiO}_3$ interface could be best described by noncentrosymmetric ($d_{xy} + p$)-wave superconductivity [118].

1.3.4. Superfluid ^3He

Superfluid helium, in contrast with the compounds mentioned above, forms a condensate of charge neutral molecules rather than a condensate of electrons on a periodic lattice. This introduces fundamental differences between these two states of matter, however, the former can still be well approximated by a TRS preserving p -wave superconductor, following (1.54) with $\psi = 0$, as parity is conserved. Due to its virtual lack of impurities, ^3He is an ideal host of topological bound states, and a remarkably ideal system for their detection. However, preserving TRS, both the superfluid helium's and the NCSs surface states are quite hard to detect with transport measurements, as no net charge or spin can be transferred, that

is the Majorana state does not couple to the electromagnetic field. Their nonzero thermal conductivity given by the Wiedemann–Franz law $\kappa/\sigma T = 3k_B^2/2e^2$ [119] can, despite that, be detected by effectively changing the gravitational field through temperature gradients [120–122].

The two different phases of superfluid helium, A and B , interestingly, host different $d(\mathbf{k})$ vectors, and consequently different “point-group” symmetries. In fact the A -phase of ${}^3\text{He}$ has Fermi points, which carry a topological \mathbb{Z} invariant (class D, $\delta = 2$ in Table 1.1), and the B phase is fully gapped, hosting helical Majorana states protected by a \mathbb{Z} invariant (class DIII, $\delta = 3$).

1.4. This thesis

A striking characteristic of topological phases is their robustness to perturbations and weak interactions. After having established in this chapter the main concepts for the study of topological systems, the remaining of this thesis is focused on numerical and analytic calculations of the behavior of topological materials in the presence of disorder and interactions. Naturally, this discussion is not exhaustive and many interesting questions are left to future research. The following calculations will be centered on a prototype model of topological superconductors without inversion center, with their inversion symmetric counterparts (singlet and triplet superconductors) as special limits.

We conclude with a general discussion on the role of interactions on the bulk of topological materials, and the possibility of a breakdown of the single-particle topology which consequently leads to the disappearance of the otherwise expected boundary modes.

Here I present a few points that this thesis will be focused on clarifying.

- Q1 Which types of boundary states exist in gapped and gapless topological phases?
- Q2 What are the experimental signatures of gapped and gapless disordered topological phases?
- Q3 Are topological boundary states robust to disorder?
- Q4 Does the bulk boundary correspondence hold for systems without translational symmetry?
- Q5 Are degenerate topological boundary states robust to symmetry preserving electron-electron interactions?
- Q6 Is the bulk's topology destroyed by symmetry preserving electron-electron interactions?

2. Topological surface states in noncentrosymmetric superconductors

In this Chapter we discuss the bulk boundary correspondence in noncentrosymmetric superconductors, and their properties of the boundary states.

At different energy scales, systems can show dramatically different behavior. For topological band Hamiltonians this is once again true. For energies well above the gap $E > \Delta$ the physics is dominated by bulk-like states, and for energies well below the gap $E < \Delta$, boundary states dominate. Sufficiently weak disorder is defined as local fluctuations that do not mix these two sectors, and we can say that the boundary states are independent from the bulk states. In the following we assume this condition to hold in order to study the topological protection of boundary states, arising from symmetry arguments. It is clear, however, that in nodal systems, this condition is somewhat artificial, as the bulk gap is zero at some manifold in the Brillouin zone. However, studying the boundary states independently of bulk physics leads to a good insight in the structure and properties of these states. In the following chapters, the validity of this approach is put to the test by studying the interplay between both boundary and bulk states numerically.

We start by deriving different topological invariants emerging in two and three dimensional time-reversal invariant topological superconductors, and calculate their effective low-energy theory. This is followed by an analysis of possible scattering events among the boundary states, based on symmetry arguments.

2.1. Bulk-boundary correspondence in nodal systems

In Section 1.1.2, we have shown that gapless regions in the Brillouin zone must be protected by topological invariants preventing a gap to open around these regions. Given a momentum defect with co-dimension D_{def} , one can define a δ -dimensional sphere for $\delta = d - D_{\text{def}}$ surrounding the defect that captures its Berry flux. Through the bulk-boundary correspondence one expects any non-trivial feature in the single particle Hamiltonian to be transcribed into boundary excitations. However, in the case of nodal systems, it is not transparent how it occurs.

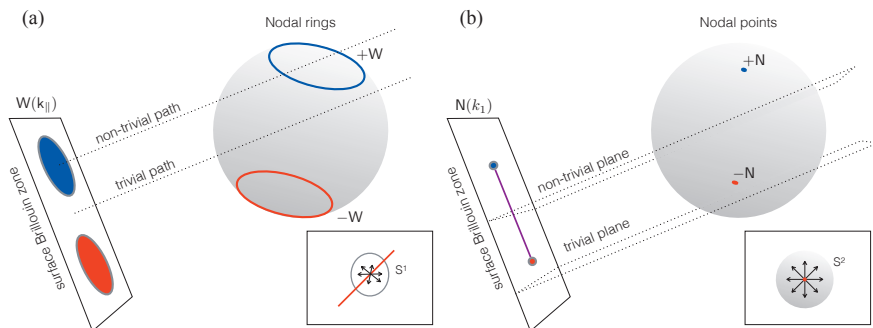


Figure 2.1. Projection of the nodal structure in the surface Brillouin zone (k_{\parallel}). Red and blue denote the chirality of the rings (points), as well as the resulting surface states. (a) Nodal rings in 3D give rise to surface flat bands for momenta within the projected area in the surface BZ. Each path ($\delta = 1$) for fixed k_{\parallel} belongs to the symmetry class AIII with broken TRS and PHS, but with the combination $S = \mathcal{TC}$. The flat bands are protected by a winding number $W(k_{\parallel})$. (b) Nodal points in 3D are projected to points in the surface BZ (k_1, k_2), connected by an arc surface state in the surface BZ. Each plane ($\delta = 2$) is analogous to a 2D fully gapped superconductor with TRS and PHS, as both k_2 and $-k_2$ belong to the $\delta = 2$ surface. The arc state is consequently protected by a \mathbb{Z}_2 index $N(k_1)$ in the class DIII.

Without loss of generality, let us look at the three-dimensional case as discussed in Ref. [64], where both nodal points (monopoles) or nodal lines (vortex lines) can appear.

i *Line nodes:* $\delta = 1$

A closed line node (nodal ring) is a source of Berry flux and is analogous to a magnetically charged wire producing a radial magnetic field. The stability of the nodal ring is ensured by the topological nature of the Hamiltonian $H(\mathbf{k})$ constrained to a 1-sphere S^1 enclosing the ring, as shown in Fig. 2.1 (a-inset). That is, the topological invariant results from the nontrivial homotopy group $\pi_1[U(n)] = \mathbb{Z}$ (cf. Sec. 1.1.3). It arises from the topological nature of one-dimensional Hamiltonians in class AIII, parametrized by k . In the continuum limit, we consider a deformation of this path to a semicircle defined by a straight line crossing the surface BZ coordinate (k_1, k_2) , $\mathcal{C}(t) = (k_1, k_2, R(2t - 1))$ for $t \in [-R, R]$, followed by a closing arc parametrized by $\mathcal{C}_{\phi}(\theta) = R(\sin \theta \cos \phi, \sin \theta \sin \phi, \cos \theta)$. In the latter, we choose an azimuthal angle ϕ such that the path does not cross any other nodal points, thus this deformation does not change the topological invariant. Since the total chirality in the system must vanish, we can find a continuous gauge transformation that fixes a constant phase everywhere at infinity. Taking $R \rightarrow \infty$ the arc does not contribute to the total Berry phase, leaving us

with a one dimensional contour along k_{\perp} , for fixed (k_1, k_2) , which can be regarded as parameters in the Hamiltonian space of $d = 1$ with AIII symmetry, as considered in the previous chapter. As long as the surface momenta are well defined, breaking translational symmetry along k_{\perp} , by considering a finite number of slabs N_{\perp} , simply leads to the appearance of bound states at the surfaces $r_{\perp} = 1$ and $r_{\perp} = N_{\perp}$.

This argument is valid for all path deformations that do not cross the nodal rings, establishing a topological distinction between paths with k_{\parallel} inside and outside the projection of the nodal rings. This is represented in Fig. 2.1(a). In the presence of periodic boundary conditions, this argument is harder to justify for directions that are misaligned with the nodal rings, and I will not attempt it. This subject is addressed in Chp. 5 numerically.

ii *Point nodes:* $\delta = 2$.

A point source of Berry flux in a three-dimensional Brillouin zone is enclosed by a 2-sphere S^2 surface surrounding the point. Again, we consider the surface Brillouin zone defined by $k_{\parallel} = (k_1, k_2)$ while along the perpendicular direction r_{\perp} , translational symmetry is broken and momentum is not a good quantum number. The stability of nodal points is guaranteed by the topological nature of the $\delta = 2$ Hamiltonians in class DIII, with a \mathbb{Z}_2 invariant, (cf. Table 1.1). With an analogous argument as before, we can deform the S^2 sphere into a half-sphere with fixed k_1 , such that as $R \rightarrow \infty$ all coordinates (k_2, k_{\perp}) belong to the diametral plane. During this transformation we can still define TRS and PHS taking $k_2 \rightarrow -k_2$. The resulting Hamiltonian is a one dimensional DIII symmetric Hamiltonian $H(k_1)$, parametrized by the surface momentum k_1 . We can infer from this example that \mathbb{Z}_2 invariants can only protect nodal points ($D_{\text{def}} = 1$) in all dimensions. As it is seen in Fig. 2.1(b), within the projection of the nodal points in the surface BZ, an arc surface state emerges, flat along k_1 and linearly dispersive along k_2 .

A generalization of the arguments above can be made for any dimension of both defect and Brillouin zone [18, 64, 123]. It is a general feature that boundary states will appear for regions within the projected nodal manifold in the surface Brillouin zone. This constitutes the *generalized bulk-boundary correspondence*.

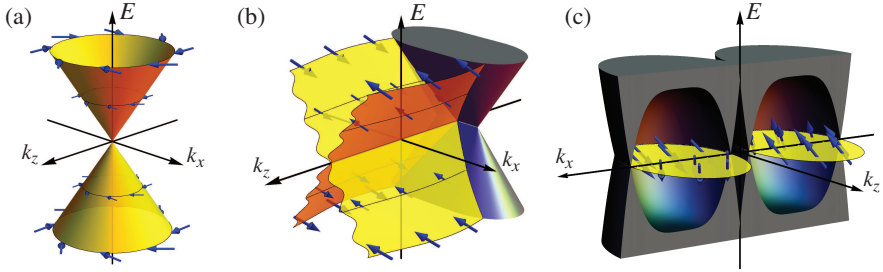


Figure 2.2. Schematic representation of the possible surface states in three dimensional superconductors. (a) Helical Majorana state, protected by a $\delta = 3$, \mathbb{Z} winding number in the symmetry class DIII. (b) Arc surface state, protected by a $\delta = 2$, \mathbb{Z}_2 index from class DIII. (c) Flat band surface states protected by a $\delta = 1$, \mathbb{Z} winding number in the symmetry class AIII.

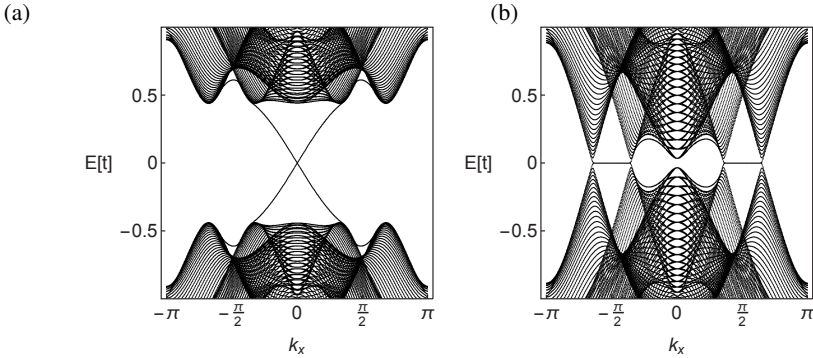


Figure 2.3. Representative band structures of the two possible edge states in two dimensional superconductors. (a) Helical Majorana state, protected by a $\delta = 2$, \mathbb{Z}_2 index in the symmetry class DIII. (b) Flat band surface states protected by a $\delta = 1$, \mathbb{Z} winding number in the symmetry class AIII. (a) $(s + p)$ -wave superconductor with $f(\mathbf{k}) = 1$. (b) $(d_{xy} + p)$ -wave superconductor with form factor $f(\mathbf{k}) = \sin k_x \sin k_y$. Described by (2.1) with parameters $t = \mu = 2\lambda = 2d$ and $\psi = 0$.

2.2. Overview of the different types of topological surface states in 2D and 3D

In this chapter we focus our attention to noncentrosymmetric superconductors in two and three-dimensions. Due to the existence of strong spin-orbit coupling, these superconductors have time-reversal symmetry $\mathcal{T}^2 = -1$ (spinful fermions) and particle-hole symmetry $\mathcal{C}^2 = +1$, belonging to the symmetry class DIII, where chiral symmetry S is always present. Apart from unitary symmetries, these superconductors are fully determined by the topological invariants summarized in the table below [66, 103],

class DIII	$\delta = 1$	$\delta = 2$	$\delta = 3$
$d = 2$	\mathbb{Z} (AIII)	\mathbb{Z}_2 (DIII)	–
$d = 3$	\mathbb{Z} (AIII)	\mathbb{Z}_2 (DIII)	\mathbb{Z} (DIII)

where d labels the BZ dimension and δ the topological dimension, as defined in the previous chapter. A schematic view of the three different surface states in three dimensions can be seen in Fig. 2.2 (a) Helical Majorana state protected by a \mathbb{Z} DIII invariant, (b) Arc surface state, protected by a \mathbb{Z}_2 DIII invariant and (c) Flat band surface states protected by a \mathbb{Z} AIII invariant. The exact band structure for two examples of two-dimensional NCS superconductors is shown in Fig. 2.3. These are representatives of the two types of edge states in two-dimensional nodal systems: (a) Helical Majorana state protected by a \mathbb{Z}_2 DIII invariant and (b) flat band edge states, protected by a \mathbb{Z} AIII invariant.

2.3. Model: Noncentrosymmetric superconductors

As introduced in Sec. 1.3, superconductors without inversion center are described at a phenomenological level by the 4×4 Bogliubov-de Gennes Hamiltonian

$$H_{\mathbf{k}} = \begin{pmatrix} h_{\mathbf{k}} & \Delta_{\mathbf{k}} \\ \Delta_{\mathbf{k}}^{\dagger} & -h_{\mathbf{k}}^T \end{pmatrix}, \quad (2.1a)$$

acting on the Nambu spinor

$$\Psi(\mathbf{k}) = (c_{\mathbf{k}\uparrow}, c_{\mathbf{k}\downarrow}, c_{-\mathbf{k}\uparrow}^{\dagger}, c_{-\mathbf{k}\downarrow}^{\dagger})^T, \quad (2.1b)$$

with spin and charge degrees of freedom. Due to inversion symmetry breaking, an antisymmetric spin orbit coupling emerges and the normal state Hamiltonian takes the form

$$h(\mathbf{k}) = \varepsilon(\mathbf{k})\sigma^0 - \lambda \mathbf{g}(\mathbf{k}) \cdot \boldsymbol{\sigma}, \quad (2.1c)$$

acting on both electron and hole parts symmetrically. The kinetic energy is given by

$$\varepsilon_{\mathbf{k}} = \sum_{i=1}^d t \cos(k_i) - \mu, \quad (2.1d)$$

describing particles on a square or cubic lattice, hopping to the nearest-neighbours with amplitude $t/2$, and μ determines the chemical potential. Momenta are measured in units of the inverse lattice spacing a^{-1} , set to $a = 1$. Finally, $\mathbf{g}(\mathbf{k}) \cdot \boldsymbol{\sigma}$ is the Rashba spin-orbit coupling with strength λ . $\mathbf{g}(\mathbf{k})$ is strongly restricted by the symmetries of the noncentrosymmetric lattice, belonging to an irreducible representation of its crystallographic point group \mathcal{G}_{PG} as summarized in App. A. In the following we consider two- and three-dimensional NCSs with point groups O , C_{4v} and C_2 (cf. Sec. 1.3 for examples) as for these cases we find representative Hamiltonians with all the three different topological boundary states. The choice of $\mathbf{g}(\mathbf{k})$ vector favours simplicity, and consequently we will look at each type of surface state in the simplest context it can appear. In three dimensions, we choose the lowest order term from each point group.

i 3D Cubic point group O

$$\mathbf{g}(\mathbf{k}) = \sin k_x \hat{\mathbf{x}} + \sin k_y \hat{\mathbf{y}} + \sin k_z \hat{\mathbf{z}}. \quad (2.1e)$$

ii Quasi-2D Tetragonal point group C_{4v}

$$\mathbf{g}(\mathbf{k}) = \sin k_y \hat{\mathbf{x}} - \sin k_x \hat{\mathbf{y}}. \quad (2.1f)$$

iii 3D Monoclinic point group C_2

$$\mathbf{g}(\mathbf{k}) = (\sin k_x + \sin k_y)(\hat{\mathbf{x}} + \hat{\mathbf{y}}) + \sin k_z \hat{\mathbf{z}}. \quad (2.1g)$$

In the absence of inversion symmetry, the superconducting gap function $\Delta_{\mathbf{k}}$ contains both spin-singlet and spin-triplet pairing components,

$$\Delta(\mathbf{k}) = f(\mathbf{k})(\psi \sigma^0 + d \mathbf{g}(\mathbf{k}) \cdot \boldsymbol{\sigma})(i\sigma^2), \quad (2.1h)$$

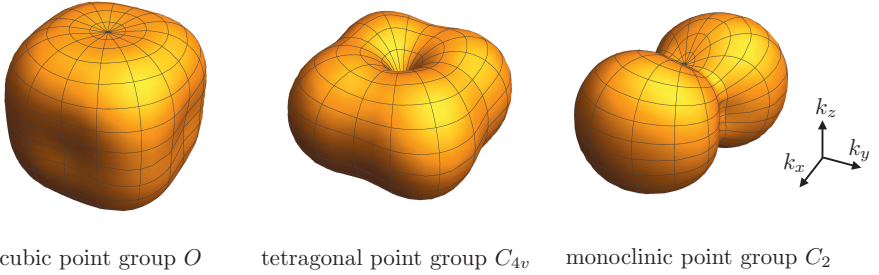


Figure 2.4. Angular dependence of the $\mathbf{g}(\mathbf{k})$ vector in the three point group symmetries considered. The absolute value was fixed in all cases to $|\mathbf{g}(\mathbf{k})| = 1.5$.

where we consider a momentum independent spin-singlet pairing amplitude¹ ψ and the triplet pairing vector $\mathbf{d}(\mathbf{k})$, assumed to be aligned with the spin-orbit pseudovector $\mathbf{g}(\mathbf{k})$ with amplitude d . This choice is a natural choice as $\mathbf{g}(\mathbf{k})$ is the only magnetic direction bias in the model, and it has been shown that it maximizes the superconducting transition temperature [97]. For convention, we take the pairing amplitudes ψ and d to be real and positive.² Furthermore we consider higher harmonics of angular momentum through the multiplication of a form factor $f(\mathbf{k})$, which is given by,

- i $f(\mathbf{k}) = 1$, for $(s + p)$ -wave superconductors,
- ii $f(\mathbf{k}) = \sin k_x \sin k_y$, for $(d_{xy} + p)$ -wave superconductors.

The resulting system has a Fermi surface which is split into two helical bands due to spin-orbit coupling, thus we can conveniently describe each helical band separately, for which the normal state energy $\xi(\mathbf{k})$ and the superconducting condensation energy $\Delta(\mathbf{k})$ are given by,

$$\xi^\pm(\mathbf{k}) = \varepsilon(\mathbf{k}) \mp \lambda g(\mathbf{k}), \quad (2.2a)$$

$$\Delta^\pm(\mathbf{k}) = f(\mathbf{k})(\psi \pm d g(\mathbf{k})), \quad (2.2b)$$

for $g(\mathbf{k}) = |\mathbf{g}(\mathbf{k})|$. Consequently the total energy at each band is given by,

$$E^\pm(\mathbf{k})^2 = \xi^\pm(\mathbf{k})^2 + \Delta^\pm(\mathbf{k})^2. \quad (2.2c)$$

¹To agree with the literature, we have chosen to represent the singlet and triplet pairing amplitude by ψ and d , a confusion can occur as general eigenvectors are also represented by ψ , and d commonly stands for dimension. This problem should be clarified by the context in which they occur.

²Note that an overall phase factor of $\Delta_{\mathbf{k}}$ can be absorbed by a $U(1)$ gauge transformation of the fermion operators.

In this basis, the Hamiltonian (2.1) has the symmetries $\tilde{U}_T = i\sigma^2 \otimes \sigma^0$, $\tilde{U}_C = \sigma^0 \otimes \sigma^1$ and $\tilde{S} = -i\sigma^2 \otimes \sigma^1$, however, we can perform a basis transformation such that the chiral operator is diagonal

$$W\tilde{S}W^\dagger = S, \quad S = -i\sigma^0 \otimes \sigma^3, \quad \text{and} \quad W = \frac{1}{\sqrt{2}} \begin{pmatrix} +\sigma^0 & -\sigma^2 \\ +i\sigma^2 & +i\sigma^0 \end{pmatrix}, \quad (2.2d)$$

resulting in $U_C = -i\sigma^0 \otimes \sigma^1$, $U_T = i\sigma^0 \otimes \sigma^2$ and for which the Hamiltonian achieves the off-block diagonal form (1.22) with the off-diagonal block

$$D(\mathbf{k}) = (b(\mathbf{k})\sigma^0 + a(\mathbf{k})\mathbf{g}(\mathbf{k}) \cdot \boldsymbol{\sigma})(-i\sigma^2), \quad (2.2e)$$

with the scalar functions $a(\mathbf{k})$ and $b(\mathbf{k})$ given by,

$$a(\mathbf{k}) = -\lambda + idf(\mathbf{k}), \quad b(\mathbf{k}) = \varepsilon(\mathbf{k}) + i\psi f(\mathbf{k}), \quad (2.2f)$$

reducing the energies (2.2c) to

$$E^\pm(\mathbf{k}) = |b(\mathbf{k}) \pm a(\mathbf{k})g(\mathbf{k})|. \quad (2.2g)$$

By performing an adiabatic transformation such that the energy spectrum of $H(\mathbf{k})$ takes only values $\tilde{E}^\pm(\mathbf{k}) = \pm 1$, we find the simplified form of the off-diagonal block (cf. Eq. (1.26)) [64, 66]

$$q(\mathbf{k}) = \sum_{\text{occ. n}} \frac{1}{E_n(\mathbf{k})} u_n(\mathbf{k}) u_n^\dagger(\mathbf{k}) D(\mathbf{k}), \quad (2.3)$$

which is simplified to

$$q(\mathbf{k}) = \frac{1}{E(\mathbf{k})} D(\mathbf{k}), \quad (2.4)$$

in the absence of spin-orbit coupling.

DIII \mathbb{Z} -invariant in $\delta = 3$

In three dimensions, the integral is performed over all three momenta in the BZ, and consequently the topological invariant is a constant. Reducing the integral (1.27) we get [64, 66, 67, 124–130]

$$W^{3D} = \int_{S^3} \frac{d^3\mathbf{k}}{24\pi^2} \epsilon^{\nu\rho\sigma} \text{tr} [q_{\mathbf{k}}^{-1} \partial_\mu q_{\mathbf{k}} \cdot q_{\mathbf{k}}^{-1} \partial_\nu q_{\mathbf{k}} \cdot q_{\mathbf{k}}^{-1} \partial_\rho q_{\mathbf{k}}]. \quad (2.5)$$

Using the above form of $q(\mathbf{k})$ and the properties of the fully antisymmetric tensor $\epsilon^{\nu\mu\rho}$, and moreover, noticing that the winding number must have a jump at some parameter values and be independent of details otherwise, we can conclude the following:

i *Centrosymmetric singlet pairing*

If $\psi \gg d$, which originates from the limit $\lambda \rightarrow 0$, we get $q(\mathbf{k}) = \exp\{i \arg(\epsilon_{\mathbf{k}} + i\psi)\}(-i\sigma^2)$. Due to the antisymmetric tensor in (2.5), we can see that the winding number vanishes. For dominant singlet superconductors, we expect no topological surface states emerging from a 3D winding number.

ii *Centrosymmetric triplet pairing*

If $d \gg \psi$, and $\lambda \rightarrow 0$, we get $q(\mathbf{k}) = (E_{\mathbf{k}})^{-1}(\epsilon_{\mathbf{k}}\sigma^0 + id \mathbf{g}_{\mathbf{k}} \cdot \boldsymbol{\sigma})(-i\sigma^2)$. Here we note that for the same reason as above the first term is not important, and the second term, by including all Pauli matrices in $\mathbf{g}_{\mathbf{k}} \cdot \boldsymbol{\sigma}$ can have a non-trivial 3D winding number. In particular, for the SOC vector given in (2.1e), there will be a unity winding number. For dominant triplet pairing, we expect to find a topological surface state in the cubit point group O .

DIII \mathbb{Z}_2 -invariant in $\delta = 2$

Here we study the \mathbb{Z}_2 invariant emerging for 2D fully gapped, and 3D nodal ($s + p$)-wave superconductors with point group C_{4v} . In the latter case, we can establish the symmetry relation of the Hamiltonian

$$D(k_x, k_y, k_z) = -D^T(-k_x, -k_y, k_z), \quad (2.6)$$

which represents an effective TRS acting on the $\mathbf{k} \equiv (k_x, k_y)$ plane. This is possible for any SOC vector respecting

$$\mathbf{g}(k_x, k_y, +k_z) = \mathbf{g}(k_x, k_z, -k_z). \quad (2.7)$$

The three dimensional \mathbb{Z}_2 invariant introduced in Sec. 1.1.4 is reduced to [66]

$$N = \text{sign}[\Delta_{k_z}^+] \text{sign}[\Delta_{k_z}^-] \quad (2.8)$$

with $\text{sign}[\Delta_{k_z}^{\pm}]$ the sign of the gap at the k_z -projecting plane in the positive or negative helicity bands, respectively (cf. Fig. 2.2). In the limit $k_z = 0$ the two dimensional invariant is obtained. N is trivial when the gap in the two helical bands have the same sign and topological

otherwise. It follows from (2.2b) that for purely singlet superconductors it is always trivial, while it can have a nontrivial value in the triplet case.

All \mathbb{Z} -invariant in $\delta = 1$

The one-dimensional invariant follows from the same discussion for $\delta = 3$, since both have odd dimensions and consequently a winding number. Fixing the surface Brillouin zone coordinates $\mathbf{k}_{\parallel} = (k_1, k_2)$, we get

$$W(\mathbf{k}_{\parallel}) = \frac{i}{2\pi} \int_{S^1} dk_{\perp} \operatorname{tr} [g_{\mathbf{k}}^{-1} \partial_{k_{\perp}} q_{\mathbf{k}}]. \quad (2.9)$$

This invariant is well defined for both 2D and 3D flat bands, except for the exact momentum values where $E^{\pm}(\mathbf{k}) = 0$, the projection of a nodal point (ring). Here $q(\mathbf{k})$ is not well defined and a topological transition might occur. Using the general form of $q(\mathbf{k})$ [65]

$$q(\mathbf{k}) = \frac{1}{2E_{\mathbf{k}}^{+} E_{\mathbf{k}}^{-}} \left[(E_{\mathbf{k}}^{+} b_{\mathbf{k}} - E_{\mathbf{k}}^{-} a_{\mathbf{k}} g_{\mathbf{k}}) - \frac{1}{g_{\mathbf{k}}} (E_{\mathbf{k}}^{-} b_{\mathbf{k}} - E_{\mathbf{k}}^{+} a_{\mathbf{k}} g_{\mathbf{k}}) \mathbf{g}_{\mathbf{k}} \cdot \boldsymbol{\sigma} \right], \quad (2.10)$$

we find that the winding number is simplified to,

$$W(\mathbf{k}_{\parallel}) = \frac{1}{2\pi} \int_0^{2\pi} dk_{\perp} \sum_{\alpha=\pm} \partial_{k_{\perp}} \arg(\xi_{\mathbf{k}}^{\alpha} + i\Delta_{\mathbf{k}}^{\alpha}). \quad (2.11)$$

A representation of the winding number density is shown below, in Fig. 2.6, where we can observe singularities at the nodal points of the superconductor in both helical bands.

2.3.1. Impurity Hamiltonian

To include weak perturbations in our system, we consider that the scattering centers are dilute enough that a single scattering event occurs, with a momentum transfer of \mathbf{q} . For magnetic impurities, this can occur together with spin flip in the final wave-function, hence, the scattering potential Hamiltonian comprises the matrix form,

$$H_{\text{imp}}^{\beta} = \sum_{\mathbf{k}\mathbf{q}} \Psi_{\mathbf{k}}^{\dagger} V_{\mathbf{q}}^{\beta} \Psi_{\mathbf{k}+\mathbf{q}}, \quad \text{with} \quad V_{\mathbf{q}}^{\beta} = (1/N) \sum_j v(\mathbf{r}_j) S^{\beta} e^{-i\mathbf{q}\cdot\mathbf{r}_j}, \quad (2.12)$$

for $S^{\beta} = (S^0, S^i)$ the charge and spin operators in Nambu space, explicitly given by

$$S^{\beta} = (\sigma^3 \otimes \sigma^0, \sigma^3 \otimes \sigma^1, \sigma^0 \otimes \sigma^2, \sigma^3 \otimes \sigma^3), \quad (2.13)$$

denoting the Fourier transform of impurity potentials $v(x_j)S^\beta$ at the surface sites r_j with strengths $v(x_j)$. Here, N stands for the number of lattice sites and $V^{\beta=0}$ correspond to nonmagnetic ($\beta = 0$) and magnetic ($\beta = \{x, y, z\}$) scattering. For simplicity, we assume that the magnetic impurities are all fully polarized along the β spin axis by a small external magnetic field of strength $H \ll H_{c2}$.

2.4. Helical Majorana states

In this section, we derive the low-energy effective Dirac Hamiltonian describing the helical Majorana surface states both for the three-dimensional and two-dimensional topological NCSs. It is our goal to understand the form and characteristics of the topological edge (surface) states and their profile as they decay into the bulk. We are nonetheless required to make simplifications to our initial model, as the calculation of the full spin dependence of edge states with spin-orbit coupling is demanding with no reward of physical insight. As we have understood in the previous section, for a triplet dominated ($s + p$)-wave superconductor, the topological invariant arises from the Dirac structure of $q(\mathbf{k})$ which is not very dependent on the details of the functions a_k and b_k , as long as the second term in (2.10) is non vanishing. With these considerations, we can justify replacing our problem with the centrosymmetric equivalent, where we adiabatically set the SOC strength λ and the spin-singlet component ψ of the superconducting gap to zero. The derivation of the surface states of topological centrosymmetric superconductors proceeds along similar lines as for the case of topological insulators [131, 132].

2.4.1. Helical Majorana state in 2D

The topological edge state in a two-dimensional system with point group C_{4v} can be obtained by first performing a small-momentum expansion near $k_x = k_y = 0$. The superconductor is described in the natural basis by

$$\tilde{H}(\mathbf{k}) = \begin{pmatrix} \tilde{\varepsilon}_k \sigma^0 & -d(k_y \sigma^3 + i k_x \sigma^0) \\ -d(k_y \sigma^3 - i k_x \sigma^0) & -\tilde{\varepsilon}_k \sigma^0 \end{pmatrix}, \quad (2.14)$$

where

$$\tilde{\varepsilon}_k = 2t - \mu - \frac{t}{2}(k_x^2 + k_y^2). \quad (2.15)$$

In order to find a localized solution at the surface $y = 0$, we consider the following ansatz for the wave function

$$\Psi(y) = \Psi(\kappa)e^{\kappa y}, \quad (2.16)$$

displaying a decay profile into the bulk with the inverse decay length κ . The real space solution is obtained following the eigenvalue equation

$$\tilde{H}(k, -i\partial_y)\psi(y) = E\psi(y), \quad (2.17)$$

where we have replaced k_y by its operator form $-i\partial_y$. This problem amounts to solving the secular equation

$$\det \left[\tilde{H}(k_x, -i\kappa) - E\mathbb{1} \right] = 0. \quad (2.18)$$

We get four solutions for $\kappa(E)$ denoted as $\beta\kappa_\alpha(E)$, with $\alpha \in \{1, 2\}$, $\beta \in \{+, -\}$,

$$\kappa_\alpha(E) = \frac{1}{t} \left[2d^2 - 2L + k_x^2 t^2 + (-1)^\alpha 2R \right]^{\frac{1}{2}}, \quad (2.19)$$

where we introduce the shorthand notation $R = \sqrt{d^4 - 2d^2L + E^2t^2}$, and $L = (2t - \mu)t$. The edge wave function can be any linear combination of these solutions, hence, we write the general form

$$\Psi(k_x, y) = \sum_{\alpha, \gamma \in \{1, 2\}} \sum_{\beta = \pm} C_{\alpha\beta\gamma} \psi_{\alpha\beta\gamma} e^{\beta\kappa_\alpha y}, \quad (2.20)$$

where two independent basis vectors $\psi_{\alpha\beta\gamma}$ form the kernel of the secular equation,

$$\psi_{\alpha\beta 1} = \begin{pmatrix} 0 \\ -idt(\beta\kappa_\alpha + k_x) \\ 0 \\ Et - L + \frac{t^2}{2}(k_x^2 - \kappa_\alpha^2) \end{pmatrix}, \quad \psi_{\alpha\beta 2} = \begin{pmatrix} +idt(\beta\kappa_\alpha - k_x) \\ 0 \\ Et - L + \frac{t^2}{2}(k_x^2 - \kappa_\alpha^2) \\ 0 \end{pmatrix}. \quad (2.21a)$$

A surface state occurs if the coefficients $C_{\alpha\beta\gamma}$ can be chosen such that the wave function $\Psi(k_x, y)$ satisfies the boundary conditions $\Psi(k_x, y = 0) = 0$ and $\Psi(k_x, y \rightarrow +\infty) = 0$. After some algebra, this leads to the condition,

$$2L = (k_x^2 + \kappa_1\kappa_2)t^2. \quad (2.22)$$

Combining Eqs. (2.40) and (2.22) gives the dispersion $E_{\pm}(k_x) = \pm d k_x$. For the surface-state wave functions at $k_x = 0$, we find

$$\Psi_{1\text{D}}^{\pm}(k_x = 0, y) = \varphi_{1\text{D}}^{\pm} [e^{-\kappa_1(0)y} - e^{-\kappa_2(0)y}], \quad (2.23a)$$

where

$$\varphi_{1\text{D}}^{\pm} = \frac{1}{\sqrt{2}} \begin{pmatrix} -i \\ 0 \\ +1 \\ 0 \end{pmatrix}, \quad \varphi_{1\text{D}}^{\mp} = \frac{1}{\sqrt{2}} \begin{pmatrix} 0 \\ +i \\ 0 \\ +1 \end{pmatrix}, \quad (2.23b)$$

where $\kappa_{\alpha}(0)$ is given by (2.40). For $d^2 > 2L > 0$, the zero-energy wave functions (2.23) decay exponentially and monotonically into the bulk, whereas for $2L > d^2$ the exponential wave function decay is modulated by periodic oscillations with frequencies $\text{Im}[\kappa_{\alpha}(0)]$. Projecting $\tilde{H}(\mathbf{k})$ in (2.14) onto the subspace $\Psi_{1\text{D}} = \{\varphi_{1\text{D}}^-, \varphi_{1\text{D}}^+\}$ yields a low-energy effective Hamiltonian for Majorana edge states, as expected it corresponds to a one-dimensional Dirac Hamiltonian

$$\langle \Psi_{1\text{D}} | \tilde{H}(\mathbf{k}) | \Psi_{1\text{D}} \rangle = -d k_x \sigma^3. \quad (2.24)$$

The disorder potential $V_{\mathbf{q}}^{\beta}$, see (2.12) within the surface-state subspace Ψ_{AS} reads

$$\langle \Psi_{1\text{D}} | V_{\mathbf{q}}^{\beta} | \Psi_{1\text{D}} \rangle = \begin{cases} -v_{\mathbf{q}} \sigma^1 & \text{if } \beta = 1, \\ 0 & \text{otherwise,} \end{cases} \quad (2.25)$$

whereas the projected electronlike parts of the charge and spin operators (2.13) are given by

$$\langle \Psi_{1\text{D}} | P_e S^{\alpha} | \Psi_{1\text{D}} \rangle = \frac{1}{2} (-1)^{\alpha} \sigma^{\alpha}, \quad (2.26)$$

where $P_e = \frac{1}{2} (\mathbb{1} + \sigma^3 \otimes \sigma^0)$. At this point we note that we can relax the restriction on the initial Hamiltonian. We find that the ‘‘non-topological’’ singlet contribution is projected to zero. Apart from modulations in the decay profile of the edge states, the general form of the low-energy Hamiltonian is given by

$$\tilde{H}_{k_x}^{1\text{D}} = \langle \Psi_{1\text{D}} | H_{\mathbf{k}} | \Psi_{1\text{D}} \rangle = -d k_x \sigma^3, \quad (2.27)$$

where $\Psi^{1\text{D}}$ is the space formed by the edge modes, which is spanned by (2.23b). Time-reversal and particle-hole symmetry in the edge-mode subspace read $\tilde{T}_{1\text{D}} = -i\sigma^2\mathcal{K}$ and $\tilde{C}_{1\text{D}} = -i\sigma^3\mathcal{K}$, respectively. As before, we find that there is no symmetry-allowed mass

term that can be added to the edge Hamiltonian (2.27), indicating that the helical Majorana edge modes are robust against disorder with strength no bigger than the superconducting gap. To demonstrate that the two-dimensional topological NCS has a \mathbb{Z}_2 -type topological characteristic, let us consider a doubled version of the edge Hamiltonian (2.27), i.e., $d k_x \sigma^3 \otimes \sigma^0$. In contrast to Hamiltonian (2.27) the doubled Hamiltonian $d k_x \sigma^3 \otimes \sigma^0$, can be fully gapped out by the symmetry preserving mass term $m \sigma^2 \otimes \sigma^2$. That is, two-dimensional topological NCSs are characterized by an odd number of Kramers pairs of Majorana edge states.

2.4.2. Helical Majorana state in 3D

Let us repeat the steps from the two-dimensional case. In three-dimensions a fully gapped superconductor can be found for the cubic crystallographic point group O , i.e., Hamiltonian (2.1) with $\lambda = 0$, $\psi = 0$, and \mathbf{g} -vector given by (2.1e). Focusing on low energies, we again perform a small-momentum expansion near the Γ point. This yields

$$\tilde{H}(\mathbf{k}) = \begin{pmatrix} \tilde{\varepsilon}_{\mathbf{k}} \sigma^0 & id(\mathbf{k} \cdot \boldsymbol{\sigma}) \sigma^2 \\ -id \sigma^2 (\mathbf{k} \cdot \boldsymbol{\sigma}) & -\tilde{\varepsilon}_{\mathbf{k}} \sigma^0 \end{pmatrix}, \quad (2.28)$$

where $\tilde{\varepsilon}_{\mathbf{k}} = 3t - \mu - \frac{t}{2}(k^2 + k_y^2)$ and $k^2 = k_x^2 + k_z^2$. With the ansatz $\psi(y) = \psi_{\kappa} e^{\kappa y}$, we obtain the eigenvalue equation

$$\tilde{H}(k, -i\partial_y)\psi(y) = E\psi(y), \quad (2.29)$$

where we have replaced k_y by $-i\partial_y$. Solving the secular equation we get

$$\kappa_{\alpha}(E) = \frac{1}{t} \left[2d^2 - 2L + k^2 t^2 + (-1)^{\alpha} 2R \right]^{\frac{1}{2}}, \quad (2.30)$$

where now $L = (3t - \mu)t$ and $R = \sqrt{d^4 - 2d^2 L + E^2 t^2}$. The kernel of the secular equation is spanned by the two independent basis vectors

$$\psi_{\alpha\beta 1} = \begin{pmatrix} dtk_z \\ dt(\beta\kappa_{\alpha} + k_x) \\ 0 \\ Et - L + \frac{t^2}{2}(k^2 - \kappa_{\alpha}^2) \end{pmatrix}, \quad \psi_{\alpha\beta 2} = \begin{pmatrix} dt(\beta\kappa_{\alpha} - k_x) \\ dtk_z \\ Et - L + \frac{t^2}{2}(k^2 - \kappa_{\alpha}^2) \\ 0 \end{pmatrix}. \quad (2.31a)$$

With this, we obtain the ansatz for the surface state,

$$\Psi(\mathbf{k}_{\parallel}, y) = \sum_{\alpha, \gamma \in \{1, 2\}} \sum_{\beta = \pm} C_{\alpha\beta\gamma} \psi_{\alpha\beta\gamma} e^{\beta\kappa_{\alpha} y}, \quad (2.32)$$

where $\mathbf{k}_{\parallel} = (k_x, k_z)$ and the coefficients $C_{\alpha\beta\gamma}$ are determined by the boundary conditions. We get the constraint

$$2L = (k^2 + \kappa_1\kappa_2) t^2, \quad (2.33)$$

which together with (2.30) yields the dispersion for the surface states

$$E_{\pm}(\mathbf{k}_{\parallel}) = \pm d k. \quad (2.34)$$

The surface state wave functions at the Γ point are found to be

$$\Psi_{2\text{D}}^{\pm}(\mathbf{k}_{\parallel} = 0, y) = \varphi_{2\text{D}}^{\pm} [e^{-\kappa_1(0)y} - e^{-\kappa_2(0)y}], \quad (2.35a)$$

with

$$\varphi_{2\text{D}}^+ = \frac{1}{\sqrt{2}} \begin{pmatrix} 1 \\ 0 \\ 1 \\ 0 \end{pmatrix}, \quad \varphi_{2\text{D}}^- = \frac{1}{\sqrt{2}} \begin{pmatrix} 0 \\ 1 \\ 0 \\ 1 \end{pmatrix}, \quad (2.35b)$$

and $\kappa_{\alpha}(0)$ as defined in (2.30). From condition (2.33) it follows that zero-energy surface states can exist if $\kappa_1(0)$ and $\kappa_2(0)$ are either both real or complex conjugate partners. In the former case, i.e., when $d^2 > 2L > 0$, the wave functions decay monotonically into the bulk with the decay lengths $\kappa_{\alpha}^{-1}(0)$. For $d^2 < 2L$, on the other hand, $\kappa_{\alpha}(0)$ are complex, which leads to an oscillatory decay of the wave functions with inverse decay length $\text{Re}[\kappa_{\alpha}(0)] = d/t$ and oscillation frequencies $\text{Im}[\kappa_{\alpha}(0)]$. An effective low-energy Hamiltonian for the surface states $\Psi_{2\text{D}}^{\pm}(\mathbf{k}_{\parallel})$ can be derived by projecting $\tilde{H}(\mathbf{k})$, see (2.28), onto the subspace $\Psi_{2\text{D}} = \{\varphi_{2\text{D}}^+, \varphi_{2\text{D}}^-\}$ formed by the two surface-state wave functions (2.35). This yields an effective 2×2 Hamiltonian:

$$\langle \Psi_{2\text{D}} | \tilde{H}(\mathbf{k}) | \Psi_{2\text{D}} \rangle = d (k_z \sigma^1 - k_x \sigma^3), \quad (2.36)$$

which has the same dispersion as (2.34). Projecting the impurity potential $V_{\mathbf{q}}^{\beta}$ (2.12) onto the surface-state subspace Ψ_{MS} we find

$$\langle \Psi_{2\text{D}} | V_{\mathbf{q}}^{\beta} | \Psi_{2\text{D}} \rangle = \begin{cases} v_{\mathbf{q}} \sigma^2 & \text{if } \beta = 2 \\ 0 & \text{otherwise.} \end{cases} \quad (2.37)$$

Remarkably, it follows that nonmagnetic scattering is absent, whereas for magnetic impurities only the out-of-plane spin component couples to the surface states. Finally, the charge and

spin operators (2.13) within the surface-state subspace are redefined to

$$\langle \Psi_{\text{MS}} | P_e S^\alpha | \Psi_{\text{MS}} \rangle = \frac{1}{2} \sigma^\alpha, \quad (2.38)$$

where $P_e = \frac{1}{2} (\mathbb{1} + \sigma^3 \otimes \sigma^0)$. Once again, we project the unsimplified Hamiltonian onto the same subspace and get

$$\tilde{H}_k^{2\text{D}} = \langle \Psi_{2\text{D}} | H_k | \Psi_{2\text{D}} \rangle = d (k_z \sigma^1 - k_x \sigma^3). \quad (2.39)$$

Time-reversal and particle-hole symmetry operators in the subspace formed by the surface modes are given by $\tilde{T}_{2\text{D}} = -i\sigma^3 \mathcal{K}$ and $\tilde{C}_{2\text{D}} = -i\sigma^1 \mathcal{K}$, respectively. Hence, (2.39) describes a single valley DIII Dirac Hamiltonian. The two symmetries of class DIII severely restrict the possible perturbations that can be added to the surface Hamiltonian (2.39) [33]. We find that the mass term $m\sigma^2$ is prohibited by time-reversal symmetry, whereas the chemical potential $\mu\sigma^0$ is forbidden by particle-hole symmetry. Moreover the $U(1)$ gauge potentials $A_x\sigma^3$ and $A_z\sigma^1$ are disallowed since they break both time-reversal and particle-hole symmetry. The only symmetry-allowed perturbations are variations of the spin-triplet amplitude d which are odd in momentum \mathbf{k} . These momentum-dependent perturbations can be neglected in the long-wave-length approximation.

2.5. Arc surface states

Next, we study arc surface states that exist, for example, at the surface of centrosymmetric superconductors with point nodes in the BdG excitation spectrum. For concreteness, we consider a system with a $\mathbf{g}(\mathbf{k})$ -vector given by (2.1f). Which we notice is precisely the same as in Sec. 2.4.1. Here we focus only on the differences between the two cases. Within a small-momentum expansion near $k_x = k_y = 0$, that is, with fixed k_z , the superconductor is described by 2.14, where now $\tilde{\epsilon}_k = 2t + t \cos k_z - \mu - \frac{t}{2}(k_x^2 + k_y^2)$. We notice that k_z enters in the form of L and therefore affects the decay profile of the wave function. Here, the solutions of the secular equation are given by

$$\kappa_\alpha(E) = \frac{1}{t} \left[2d^2 - 2L + k_x^2 t^2 + (-1)^\alpha 2R \right]^{\frac{1}{2}}, \quad (2.40)$$

with $\alpha \in \{1, 2\}$, $R = \sqrt{d^4 - 2d^2 L + E^2 t^2}$, and $L = (2t + t \cos k_z - \mu) t$. The form of the eigenstates is exactly given by (2.23). The condition $d^2 > 2L > 0$ becomes

$$\arccos \left[(d^2 / (2t) - 2t + \mu) / t \right] < |k_z| < \arccos \left[(\mu - 2t) / t \right], \quad (2.41)$$

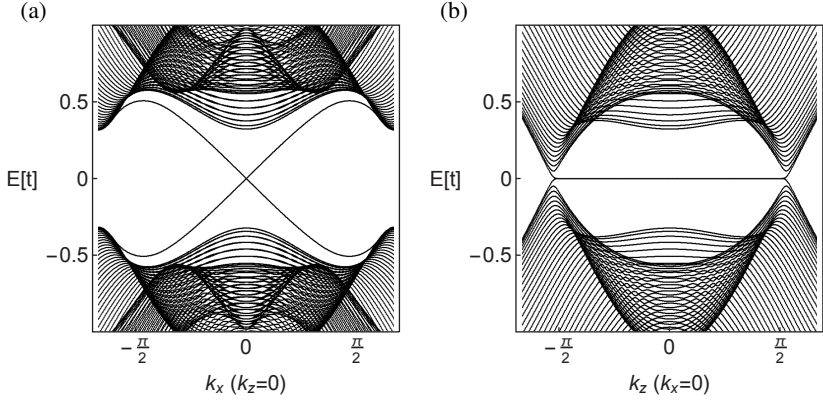


Figure 2.5. Band structure of the arc surface state present in the (010) surface of the $(s+p)$ -wave noncentrosymmetric superconductor with point group symmetry C_{4v} and parameters $(t, \mu, \lambda, \psi, d) = (1, 2, 0.5, 0.125, 0.5)$.

the zero-energy wave functions (2.23) decay exponentially and monotonically into the bulk, whereas for $2L > d^2$ the exponential wave function decay is modulated by periodic oscillations with frequencies $\text{Im}[\kappa_\alpha(0)]$. The transition point corresponds to the projection of the nodal point in the surface Brillouin zone (see Fig. 2.5). Projecting $\tilde{H}(\mathbf{k})$, see (2.14), onto the subspace $\Psi_{AS} = \{\varphi_{AS}^-, \varphi_{AS}^+\}$ yields a low-energy effective Hamiltonian for the arc surface states,

$$\langle \Psi_{AS} | \tilde{H}(\mathbf{k}) | \Psi_{AS} \rangle = -dk_x \sigma^3. \quad (2.42)$$

The disorder potential V_q^β , see (2.12), within the surface-state subspace Ψ_{AS} reads

$$\langle \Psi_{AS} | V_q^\beta | \Psi_{AS} \rangle = \begin{cases} -v_q \sigma^1 & \text{if } \beta = 1, \\ 0 & \text{otherwise.} \end{cases} \quad (2.43)$$

2.6. Flat-band edge-states

Derivation of flat band wave functions

Deriving the zero energy flat band wave functions is a little more subtle, this is because we cannot neglect spin orbit coupling, as without it flat bands would not exist. Here, we follow an analogous procedure as in the previous sections, however, we are forced to use some simplifications in the treatment, as we wish to find the surface states of a 4×4 Hamiltonian

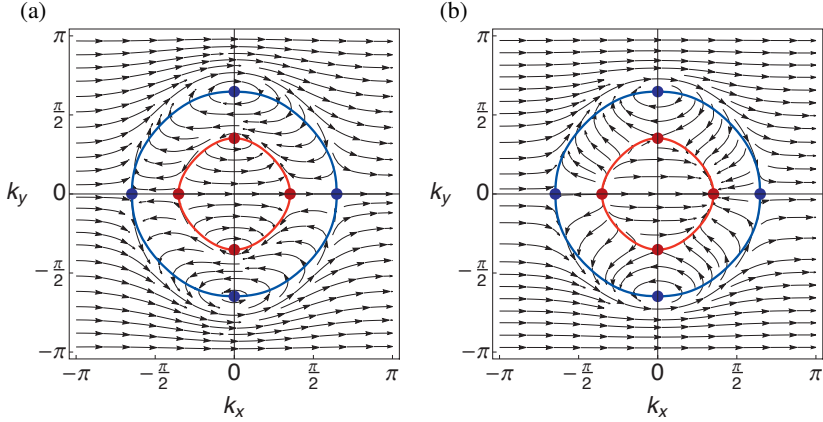


Figure 2.6. Momentum dependence of $\text{tr arg } q(\mathbf{k})$ holding singularities at the nodal points of the $(d_{xy} + p)$ -wave superconductor, for dominant singlet pairing (a) and dominant triplet pairing (b). The inner Fermi surface changes its chirality, contributing additively (a) or destructively (b) to the phase winding imposed by the outer shell. The region in between the two shells always have $W = \pm 1$, while close to the origin it can have $W = \pm 2$ (a) or $W = 0$ (b). (b) corresponds to the band structure presented in Fig. 2.3(b).

with 5 independent parameters, bound to be a hard problem. We resort to the quasiclassical approximation, for which the fast modes are determined by the Fermi momenta. This is a valid approximation as long as the coherence length ξ is significantly larger than $(k_F)^{-1}$ [133].

We start by determining the secular equation as above, considering the Hamiltonian (2.1) on the semi-infinite plane $y > 0$, with the (01) edge located at $y = 0$. The ansatz for the nondegenerate edge-state wave function is taken to be

$$\Psi_{k_x} = \sum_{\alpha, \beta} C_{\beta}^{\alpha} \psi_{\beta}^{\alpha} e^{\kappa_{\beta}^{\alpha} y} e^{i k_x x}, \quad (2.44)$$

which decays exponentially into the bulk with inverse decay lengths $\text{Re}[\kappa_{\beta}^{\alpha}] < 0$. In the off-diagonal basis, cf. Eq. 1.22, the general wave function $\Psi_{k_x} = (\chi_{k_x}, \eta_{k_x})^T$ can be split into a part $(\chi_{k_x}, 0)^T$ with positive chirality and a part $(0, \eta_{k_x})^T$ with negative chirality. Since all the eigenstates of $H_{\mathbf{k}}$ can be chosen to have definite chirality, it follows that $\eta_{k_x} = 0$ whenever $\chi_{k_x} \neq 0$ and vice versa [126, 127, 134]. In addition, we observe that for every edge-state wave function $\Psi_{k_x}^+$ with edge momentum k_x and positive chirality there is a

time-reversed partner $\Psi_{k_x}^-$ with edge momentum $-k_x$ and negative chirality, related by

$$\Psi_{k_x}^+ = \begin{pmatrix} \chi^{k_x} \\ 0 \end{pmatrix}, \quad \Psi_{k_x}^- = \begin{pmatrix} 0 \\ i\sigma^2 \chi_{-k_x}^* \end{pmatrix}. \quad (2.45)$$

In order to derive the form of the flat band eigenfunctions, we perform a small momentum expansion of the tight-binding Hamiltonian (2.1), around the Γ -point. This yields a continuum model with quadratic dispersions in the normal state and Fermi wave vectors

$$k_F^\alpha = -\alpha m \lambda + \sqrt{(m\lambda)^2 + 2m\tilde{\mu}}, \quad (2.46)$$

where $m = -1/t$, $\tilde{\mu} = \mu - 2t$, and $\alpha \in \{+, -\}$ labels the two helical Fermi surfaces. We consider a (01) edge located at $y = 0$, where the superconductor and the vacuum occupy the half-spaces $y > 0$ and $y < 0$, respectively. As in the previous section, the zero-energy edge states can be determined by solving the equation $H(k_x, -i\partial_y)\Psi_{k_x} = 0$, with the wave function ansatz $\Psi_{k_x} = \Psi_{\kappa x} e^{\kappa y}$. In the following, we focus on solutions with positive chirality, which exist within the interval $-k_F^+ < k_x < -k_F^-$. In that case, the secular equation, $\det [H(k_x, -i\kappa)] = 0$, can be reexpressed as

$$\det [D^\dagger(k_x, -i\kappa)] = [\kappa k_x \psi + \tilde{\mu} + \frac{1}{2m}(\kappa^2 - k_x^2)]^2 + (\lambda - \kappa k_x d)^2 (\kappa^2 - k_x^2) = 0, \quad (2.47)$$

which is a polynomial equation of fourth degree in κ . By solving it numerically, one can resolve in momentum k_x the existence of flat bands (that is, the number of solutions with $\text{Re}[\kappa_\beta^\alpha] < 0$), and, the spin polarization and depth profile of the resulting edge bound states. However, to help understand which are the dominant contributions to the above equation, we shall simplify it in quasiclassical terms. In this approximation, the main contribution to the roots of (2.47) comes from the Fermi momentum, which can be inferred, from the free term of (2.47),

$$a_0 = \frac{1}{4m^2}(k_x^2 - k_F^{-2})(k_x^2 - k_F^{+2}), \quad (2.48)$$

where k_x is restricted to the momentum span to $-k_F^+ < k_x < -k_F^-$, we have $a_0 < 0$, and consequently analyzing (2.47) and (2.48) one concludes that as long as $d > \psi$, (2.47) has two real roots and two complex conjugate roots. That is, the solutions of (2.47) are given

after some manipulation by

$$\kappa_{\beta}^{+} = -k_{\perp}^{+} - (-1)^{\beta} i \frac{k_{\text{F}}^{+}}{k_{\perp}^{+}} \sqrt{\frac{\widetilde{\Delta}_{+}^{2}(k_x, ik_{\perp}^{+})}{\lambda^2 + 2\widetilde{\mu}/m}}, \quad \kappa_{\beta}^{-} = (-1)^{\beta+1} ik_{\perp}^{-} - \frac{k_{\text{F}}^{-}}{k_{\perp}^{-}} \sqrt{\frac{\widetilde{\Delta}_{-}^{2}(k_x, k_{\perp}^{-})}{\lambda^2 + 2\widetilde{\mu}/m}}, \quad (2.49)$$

in line with Refs. [66, 126, 127]. Here, $\beta \in \{1, 2\}$, the transverse momenta $k_{\perp}^{+} = \sqrt{k_x^2 - (k_{\text{F}}^{+})^2}$ and $k_{\perp}^{-} = \sqrt{(k_{\text{F}}^{-})^2 - k_x^2}$, and $\widetilde{\Delta}_{\pm}(k) = (k_{\text{F}}^{\pm} d \pm \psi) k_x k_y$. We observe that κ_1^{+} and κ_2^{+} are purely real, while κ_1^{-} and κ_2^{-} form a complex conjugate pair. Furthermore, the maximum decay length $\max\{-\text{Re}[\kappa_{\beta}^{\pm}]^{-1}\}$ rapidly increases as $k_x \rightarrow -k_{\text{F}}^{\pm}$. The wave functions are well confined to the edge for k_x in the middle of the interval $[-k_{\text{F}}^{+}, -k_{\text{F}}^{-}]$, whereas as k_x approaches the boundaries of the interval the flat-band states start to penetrate over longer distances into the bulk, extending through the entire slab at $k_x = k_{\text{F}}^{\pm}$.

For each of the four roots κ_{β}^{\pm} , the kernel of the secular equation is spanned by one basis vector ψ_{β}^{\pm} , which in the off-diagonal basis in Eq. (1.22) reads,

$$\psi_{\beta}^{+} = \begin{pmatrix} 2 - \beta \\ \frac{i(2 - \beta)k_{\text{F}}^{+}}{k_{\perp}^{+} - k_x} \\ \frac{\beta - 1}{\beta - 1} \\ \frac{i(\beta - 1)k_{\text{F}}^{+}}{k_{\perp}^{+} - k_x} \end{pmatrix}, \quad \psi_{\beta}^{-} = \begin{pmatrix} 1 \\ -k_{\text{F}}^{-} \\ \frac{ik_x + (-1)^{\beta}k_{\perp}^{-}}{0} \\ 0 \end{pmatrix}, \quad (2.50)$$

with $\beta \in \{1, 2\}$. With this, the ansatz for the flat-band edge states can be written as a linear combination of the basis states (2.50) as in (2.44) where the coefficients C_{β}^{α} are fixed by the boundary conditions

$$\Psi(k_x, y = 0) = 0, \quad \Psi(k_x, y = \infty) = 0. \quad (2.51)$$

The latter condition implies $C_2^{+} = 0$, since $\text{Re}[\kappa_2^{+}] > 0$, but there exists a nonzero solution for $(C_1^{+}, C_1^{-}, C_2^{-})$ that satisfies the boundary conditions. After some algebra, we find that in the off-diagonal basis, (1.22), the zero-energy edge-state wave function with positive chirality is given by $\Psi_{k_x}^{+} = (\chi^{k_x}, 0)^T$, with

$$\chi^{k_x} = \begin{pmatrix} -2k_{\text{F}}^{+}k_{\perp}^{-}e^{\kappa_1^{+}y} + b_1e^{\kappa_2^{-}y} + b_1^{*}e^{\kappa_1^{-}y} \\ 2ia_1k_{\perp}^{-}e^{\kappa_1^{+}y} - a_2ie^{\kappa_1^{-}y} - a_2^{*}ie^{\kappa_2^{-}y} \end{pmatrix} e^{ik_x x}, \quad (2.52a)$$

where

$$a_1 = k_{\perp}^+ + k_x, \quad (2.52b)$$

$$a_2 = a_1(k_{\perp}^- + ik_x) + ik_{\text{F}}^+ k_{\text{F}}^-, \quad (2.52c)$$

$$b_1 = k_{\text{F}}^+(k_{\perp}^- + ik_x) + ik_{\text{F}}^- a_1. \quad (2.52d)$$

Similarly, we can derive solutions of the equation $H(k_x, -i\partial_y)\Psi_{k_x} = 0$ with negative chirality, which exist within the interval $k_{\text{F}}^+ < k_x < k_{\text{F}}^-$. Repeating similar steps as above, we find that the negative chirality edge-state wave function is given by $\Psi_{k_x}^- = (0, \eta_{k_x})^T$, with

$$\eta_{k_x} = \begin{pmatrix} -2i\tilde{a}_1 k_{\perp}^- e^{\kappa_1^+ y} + \tilde{a}_2 i e^{\kappa_1^- y} + \tilde{a}_2^* i e^{\kappa_2^- y} \\ 2k_{\text{F}}^+ k_{\perp}^- e^{\kappa_1^+ y} - \tilde{b}_1^* e^{\kappa_1^- y} - \tilde{b}_1 e^{\kappa_2^- y} \end{pmatrix} e^{ik_x x}, \quad (2.52e)$$

where

$$\tilde{a}_1 = k_{\perp}^+ - k_x \quad (2.52f)$$

$$\tilde{a}_2 = \tilde{a}_1(k_{\perp}^- - ik_x) + ik_{\text{F}}^- k_{\text{F}}^+ \quad (2.52g)$$

$$\tilde{b}_1 = k_{\text{F}}^+(k_{\perp}^- - ik_x) + ik_{\text{F}}^- \tilde{a}_1. \quad (2.52h)$$

As expected, the wave functions $\Psi_{k_x}^+ = (\chi_{k_x}, 0)$ and $\Psi_{k_x}^- = (0, \eta_{k_x})$ transform into each other by time-reversal symmetry, i.e.,

$$\begin{pmatrix} 0 & i\sigma^2 \\ i\sigma^2 & 0 \end{pmatrix} \Psi_{k_x}^+(y) = [\Psi_{-k_x}^-(y)]^*, \quad (2.52i)$$

where we have used the fact that κ_1^+ is purely real and (κ_1^-, κ_2^-) are complex conjugate partners. An expression similar to (2.52) can be derived for the zero-energy edge states on the opposite edge, i.e., for the Hamiltonian (2.1) on $y < 0$, which supports zero-energy flat band states with opposite chirality as compared to (2.52).

In closing, we remark that for other edge orientations the flat-band states can be derived in a similar manner. For any given edge orientation we can define the momentum parallel to the edge as $k_{\parallel} = k_x \sin(\varphi) + k_y \cos(\varphi)$. Correspondingly, the secular equation for the positive chirality edge states reads $\det[D^{\dagger}(k_{\parallel}, -i\kappa)] = 0$. Within the continuum approximation, we find that for dominant triplet pairing, $d > \psi$, the flat bands are always of single degeneracy. Zero-energy states appear in regions of the edge Brillouin zone that are bounded by the projected nodal points. Hence, the density of edge states per unit length can be approximated

by

$$\frac{dN}{dt} = |k_0^- \sin \varphi - k_0^+ \cos \varphi| - |k_0^- \cos \varphi - k_0^+ \sin \varphi|, \quad (2.53)$$

where $\varphi \in [0, \pi/4[$ is the angle between the considered edge orientation and the nearest (01) or (10) direction.

Spin polarization of flat-band edge states

For the (01) edge of the $(d_{xy} + p)$ -wave superconductor one finds that the flat-band states are strongly polarized in the yz -spin plane, but have a vanishing spin component along the x axis [101–103]. Using the same projection procedure used in above sections, with the flat band wave functions $\Psi_{k_x}^\pm$ defined by (2.52), we find it has the following properties

$$\langle \Psi_{k_x}^\pm | \tilde{S}^x | \Psi_{k_x}^\pm \rangle = 0, \quad \langle \Psi_{k_x}^\pm | \tilde{S}^{y,z} | \Psi_{k_x}^\pm \rangle \neq 0, \quad (2.54)$$

for all k_x with $k_F^+ < |k_x| < k_F^-$. Here, \tilde{S} denotes the spin operator in the off-diagonal basis. Moreover, one finds that the y component of the spin expectation value is much larger than the z component and that the sign of the y -spin polarization correlates with the chirality Γ of the flat-band edge state, such that $\text{sgn}[\langle \Psi_{k_x}^\pm | \tilde{S}^y | \Psi_{k_x}^\pm \rangle] = \mp 1$. Finally, we note that the two flat-band edge states $\Psi_{-k_x}^+$ and $\Psi_{k_x}^-$, which have opposite edge momenta, have opposite spin polarization. That is,

$$\langle \Psi_{-k_x}^+ | \tilde{S}^{y,z} | \Psi_{-k_x}^+ \rangle = - \langle \Psi_{k_x}^- | \tilde{S}^{y,z} | \Psi_{k_x}^- \rangle, \quad (2.55)$$

for all k_x with $k_F^+ < |k_x| < k_F^-$, which is consistent with time-reversal symmetry.

Impurity scattering among flat-band edge states

First, we observe that impurity scattering processes connecting flat-band edge states to bulk nodal quasiparticles are strongly suppressed, since the bulk density of states vanishes linearly as it approaches the nodal point. A rough estimate for the effects of impurity scattering among the zero-energy edge states can be obtained from the matrix elements of the impurity potential $V_{q_x}^\beta$ between two flat-band edge-state wave functions. Because the edge spectrum of the $(d_{xy} + p)$ -wave superconductor has in general two flat bands with opposite chirality, it is useful to distinguish between ‘‘inband’’ scattering between states with the same chirality and ‘‘interband’’ scattering between states with opposite chirality. From

$$\{V_{q_x}^0, \tilde{S}\} = 0, \quad (2.56)$$

and

$$\langle \Psi_{k_x}^\pm | \widetilde{V}_{k'_x - k_x}^0 | \Psi_{k'_x}^\pm \rangle = 0, \quad \text{for all } k_x, k'_x, \quad (2.57)$$

where $\widetilde{V}_{q_x}^0$ is given by (2.12) in the off-diagonal basis. It follows that edge flat bands are protected against nonmagnetic intraband scattering by chiral symmetry. In other words, since nonmagnetic onsite disorder preserves the total chirality number of the superconductor, it can remove edge states only in pairs of opposite chirality. Magnetic impurities, on the other hand, break chiral symmetry, i.e.,

$$\{V_{q_x}^{x,y,z}, \widetilde{S}\} \neq 0, \quad (2.58)$$

and therefore allow for strong intraband scattering. For the case of impurity scattering between edge flat bands with opposite chirality we find by use of Eq. (2.45) that time-reversal invariance forbids nonmagnetic backscattering between the time-reversed partners $\Psi_{k_x}^-$ and $\Psi_{-k_x}^+$. That is,

$$\langle \Psi_{-k_x}^+ | \widetilde{V}_{2k_x}^0 | \Psi_{k_x}^- \rangle = 0, \quad (2.59)$$

for all k_x with $k_F^+ < k_x < k_F^-$. Moreover, for two flat-band edge states with nearly opposite momenta k_x and $-k'_x$ (i.e., $0 < |k_x - k'_x| < k_F^- - k_F^+$), one finds that the corresponding matrix element $\langle \Psi_{-k'_x}^+ | \widetilde{V}_{k_x + k'_x}^0 | \Psi_{k_x}^- \rangle$ is nonzero but small, due to the mismatch between the almost opposite spin polarizations of the two edge states. In the presence of magnetic impurities, however, spin-flip scattering is allowed, and hence scattering between states with opposite spin polarizations is possible.

The above considerations suggest that moderately strong nonmagnetic disorder, with strength γ_{imp} smaller or of the same order as the superconducting gaps $|\Delta_\pm| = |\psi \pm d|$, has only weak effects on the flat-band edge states. Magnetic impurities, however, which lift the symmetry protection of the flat-band states, are expected to strongly reduce the number of edge states. To test these expectations, we show in Chp. 5 numerical simulations of the $(d_{xy} + p)$ -wave superconductor in the presence of different types of edge disorder.

Zero energy flat bands in three dimensions are analogous to the ones in two-dimensions. In particular, one can consider the solution in (2.52) to be valid for a cut $k_2 = 0$ in the three dimensional case. However, calculating the full dependence in the entire two-dimensional surface BZ is demanding and does not contribute any new insight. We should note, however, that the phase space for intra-band scattering events is substantially enlarged, and we expect robustness to impurities to decrease accordingly. In the following chapter we study this effects numerically for dilute impurities.

2.7. Conclusion

We have studied both fully gapped and nodal topological superconductors and considered three different types of surface states: helical Majorana modes, arc surface states, and zero-energy flat bands. Due to SOC, these surface states exhibit an intricate helical spin texture, where the spin polarization strongly depends on the surface momentum. Time-reversal invariance ensures that surface states with opposite momenta have opposite spin polarizations, which leads to the absence of backscattering from nonmagnetic impurities. Furthermore, we have derived the low-energy properties of the various types of NCSs, allowing for the identification of characteristic scattering events due to their spin polarization. In the following chapter, we use this knowledge to predict experimental signatures.

3. Quasiparticle interference: Experimental signatures of topological surface states

3.1. Introduction

One of the most challenging journeys for the community studying topological matter is to find a smoking gun experiment that clearly tells apart topologically trivial from non-trivial states. A good control over topological edge states in superconductors could allow not only for the study of extremely exotic new particles with non-abelian exchange statistics [135, 136], but also possibly manipulating them in a directed way. Among important proposals are the computation of de-coherence free quantum algorithms [137], memory devices [138] as well as spintronics [139], using their characteristic spin polarization.

In this chapter, we proceed to propose an experimental setup to facilitate the detection of principal characteristics of topological surface states in nodal superconductors. We have seen in the previous chapters, that due to time-reversal invariance, surface quasiparticles with opposite momenta have opposite spin polarizations. This in turn leads to the absence of elastic backscattering from nonmagnetic impurities, since scattering processes involving spin flips are forbidden unless time-reversal symmetry is broken.

A signature of the allowed and forbidden scattering channels at any material can be tested by observing the fluctuations of the diffusive state. Absence of backscattering is imprinted in the allowed momentum transfers between quasiparticles and is tested experimentally using Fourier-transform scanning tunneling spectroscopy (FT-STs) [140–144]. This experimental technique uses the presence of dilute impurities to probe the electronic properties of surface quasiparticles at finite momenta q through the analysis of interference patterns resulting from impurity scattering processes. It resorts to a local probe in real space which can image the surface local density of states, and, if the tip is spin polarized, it can also recover information about the quasiparticle's spin.

We present an analytical derivation and numerical simulations of the quasiparticle interference (QPI) on the surface of both nodal and fully gapped topological superconductors.

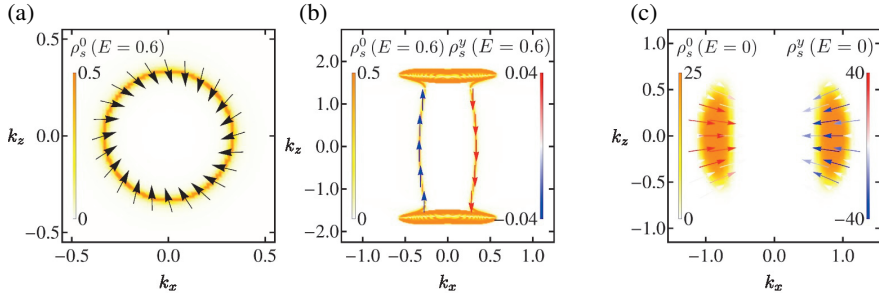


Figure 3.1. Energy spectrum and spin texture $\rho_s^\alpha(E, \mathbf{k}_\parallel)$ (given in (3.1)) of the helical Majorana mode (a) and the arc state (b) on the (010) surface of a topological superconductor with point groups O and C_{4v} , respectively, cf. (2.1). Here we set $\lambda = -2.0$ and $\psi = 0.5$. The arrows on the surface states indicate the magnitude and direction of the spin polarization. (c) Spin texture $\rho_s^\alpha(E = 0, \mathbf{k}_\parallel)$ of the zero-energy flat bands on the surface of a nodal NCS with point group C_2 , $\lambda = 0.5$, and $\psi = 4.0$. In-plane and out-of-plane components of the spin polarization are represented by arrows and the color scale, respectively. Evaluated for a slab of thickness $N = 10^2$ with intrinsic broadening $\eta = 0.005$. The sum is taken over the first $n_0 = 10$ layers, approximately the decay length of the surface states.

Even though our focus will be restricted to single-band centrosymmetric and noncentrosymmetric superconductors, our results can be generalized in a straightforward manner to any time-reversal invariant topological superconductor, e.g., to multiband superconductors with dominant spin-triplet pairing [38].

In the following, we study the QPI patterns for the three types of topological surface states introduced in Chp. 2 in the presence of both magnetic and nonmagnetic impurities, and identify their universal features in the ordinary and spin-resolved FT-STs response. Such universal behavior, allows for the distinction among the three types of surface states.

The dispersion and spin polarization of the ingap states appearing at the surface of a topological superconductor can be directly calculated by the density of states. This is shown in Fig. 3.1, which displays the spin-, momentum-, and energy-resolved surface density of states of the three possible surface states, given by

$$\rho_s^\alpha(E, \mathbf{k}_\parallel) = -\frac{\hbar}{4\pi} \text{Im} \sum_{n=1}^{n_0} \text{tr} \{ S^\alpha G_{nn}^{(0)}(E, \mathbf{k}_\parallel) \}. \quad (3.1)$$

Here,

$$G_{nn}^{(0)}(E, \mathbf{k}_\parallel) = [E + i\eta - H_{nn}(\mathbf{k}_\parallel)]^{-1}, \quad (3.2)$$

is the zero-temperature Green's function of the Hamiltonian (2.1) in a slab geometry with surface perpendicular to the y axis,

$$H_{nn'}(\mathbf{k}_{\parallel}) = \frac{1}{2\pi} \int dk_y e^{ik_y(n-n')} H_{\mathbf{k}}, \quad (3.3)$$

and $\mathbf{k}_{\parallel} = (k_x, k_z)$ denotes the surface momentum. As a result of the strong SOC and the nontrivial topology of the bulk wave functions, these surface states possess an intricate helical spin texture. A summary of the results from the last chapter is listed below.

Helical Majorana modes.

Fully gapped time-reversal invariant topological superconductors with dominant triplet pairing and \mathbf{g} -vector of the form (2.1e) exhibit linearly dispersing helical Majorana modes (cf. Sec. 2.4 and Fig. 3.1(a)) [98, 145, 146]. Similar to the surface states of topological insulators [131, 132], the linearly dispersing Majorana modes of topological superconductors exhibit a helical spin texture, with the spin and momentum directions locked to one another. In the absence of spin orbit coupling, they are locked at a 90 degree angle, while for general values of λ and ψ this is no longer the case. Interestingly, the spin of the helical Majorana mode is polarized entirely in the surface plane at all energies, which leads us to expect a divergent signal in the QPI pattern for magnetic impurities polarized in the perpendicular plane.

Arc surface states.

Nodal NCSs with $d > \psi$ and \mathbf{g} -vector given by (2.1f) support arc surface states, i.e., zero-energy states forming one-dimensional open arcs in the surface Brillouin zone, connecting the projections of two nodal points (rings) of the bulk gap (Fig. 3.1(b)). We find that the arc states show a strong spin polarization in the yz spin-plane, with a vanishing component along the x axis. In the centrosymmetric limit, scattering is expected to occur for magnetic impurities polarized along x .

Zero-energy flat bands.

Zero-energy flat bands generically occur at the surface of three-dimensional nodal NCSs whose triplet pairing component is comparable to or larger than its singlet pairing component. One possible \mathbf{g} -vector supporting these states is given by (2.1g). These flat-band surface states appear within regions of the surface Brillouin zone that are bounded by the projections of the bulk nodal lines (Fig. 3.1(c)). Strong SOC together with the nontrivial bulk topology

lead to an intricate three-dimensional spin-texture of the flat-band surface states, as indicated by the arrows and color scale in Fig. 3.1(c), hence, it is expected that magnetic impurities will lead to strong interband scattering. On the other hand, due to the very large phase space in which scattering might occur, flat bands are also expected to show intraband scattering, even for non-magnetic impurities.

3.2. Local density of states with dilute impurities

In the following, the Born approximation [141–143] is employed to calculate the QPI spectra of subgap states on the (010) surface of topological superconductors. A good approximation for the Fourier-transformed differential conductance tensor dI_α/dV , is given by

$$\delta\rho_s^{\alpha\beta}(E, \mathbf{q}_\parallel) = -\frac{1}{2\pi i} \left[\Lambda^{\alpha\beta}(E, \mathbf{q}_\parallel) - \left\{ \Lambda^{\alpha\beta}(E, -\mathbf{q}_\parallel) \right\}^* \right], \quad (3.4)$$

with $(\alpha = 0)$ ordinary and $(\alpha = 1, 2, 3)$ spin-resolved FT-STs response for $\mathbf{q}_\parallel = (q_x, q_z)$ the momentum transfer along the surface and

$$\Lambda^{\alpha\beta}(E, \mathbf{q}_\parallel) = \int \frac{d^2 k_\parallel}{(2\pi)^2} \sum_{n=1}^{n_0} \text{tr}_\sigma \left[S^\alpha \delta G_{nn}^\beta(E, \mathbf{k}_\parallel, \mathbf{q}_\parallel) \right]_{11}. \quad (3.5)$$

In (3.5) the subscript “11” represents indices in Nambu particle-hole space, tr_σ is the trace in spin space, and δG_{nn}^β denotes the change in the BdG Green’s function $G_{nn}^{(0)}$ due to scattering processes. For weak impurity potentials V_q^β , disorder scattering can be treated within the Born approximation yielding

$$\delta G_{nn}^\beta(E, \mathbf{k}_\parallel, \mathbf{q}_\parallel) = \sum_{n'n''} G_{nn'}^{(0)}(E, \mathbf{k}'_\parallel) V_{n'n''}^\beta G_{n''n}^{(0)}(E, \mathbf{k}_\parallel), \quad (3.6)$$

with $\mathbf{k}'_\parallel = \mathbf{k}_\parallel + \mathbf{q}_\parallel$. The Fourier-transformed disorder potential

$$V_{nn'}^\beta = \frac{1}{2\pi} \int dq_y e^{iq_y(n-n')} V_q^\beta = v_0 S^\beta \sum_{n''=1}^{n_0} \delta_{n,n''} \delta_{n',n''}, \quad (3.7)$$

describes onsite impurities with strength v_0 . For our numerical simulations, we consider the fixed value of $v_0 = 0.2$, assumed to be equally distributed among the $n_0 = 10$ outermost layers of the superconductor.

With the possibility of resolving spin, using spin-polarized scanning tunneling spectroscopy, all the components of the response tensor $\delta\rho_s^{\alpha\beta}(E, \mathbf{q}_\parallel)$ can, in principle, be measured. The α -spin conductance channel can be selected via the polarization direction of the spin-polarized

tunneling tip, whereas the component β of the spin scattering channel is determined by the direction of the external magnetic field.

3.3. Analytical result in the centrosymmetric limit

Before discussing numerical simulations of QPI patterns on the surface of noncentrosymmetric superconductors, it is instructive to first consider centrosymmetric topological systems. It was shown in Sec. 2.4 that in this limit, the surface states can be described by simple Dirac-type Hamiltonians with spin and momentum locking. It was also shown that a single polarization of the magnetic impurities enables backscattering, widely simplifying our results. Due to the simple nature of these surface Hamiltonians, it is possible to derive analytical expressions for the QPI patterns, as it will be shown in the following.

Helical Majorana modes

The universal properties of helical Majorana surface states in superconductors with inversion symmetry are described by the massless Dirac Hamiltonian, cf. Eqs. (2.36) and (2.37),

$$H_{\text{MS}}(\mathbf{k}_{\parallel}) = d(k_z\sigma^1 - k_x\sigma^3) + v_0\sigma^2, \quad (3.8)$$

where $v_0\sigma^2$ is an onsite disorder potential describing impurity spins polarized along the y axis. The helical Majorana mode is spin polarized only in the inplane direction k_{\parallel} . For the surface state (3.8), we find that spin and momentum directions are inclined at a right angle to each other. This is in contrast to helical Majorana states of noncentrosymmetric superconductors, where spin and momentum are in general locked to each other at an angle different from $\pm\pi/2$, see Fig. 3.1(a) and discussion in Sec. 3.4.

The QPI patterns of the Majorana state (3.8) are obtained from (3.4) upon replacing $\Lambda^{\alpha\beta}(E, \mathbf{q}_{\parallel})$ by

$$\Lambda_{\text{MS}}^{\alpha\beta=2}(E, \mathbf{q}_{\parallel}) = \frac{v_0}{2} \int \frac{d^2 k_{\parallel}}{(2\pi)^2} \text{tr} \left[\sigma_{\alpha} G_{\text{MS}}^{(0)}(i\varpi, \mathbf{k}'_{\parallel}) \sigma_2 G_{\text{MS}}^{(0)}(i\varpi, \mathbf{k}_{\parallel}) \right]_{i\varpi \rightarrow E+i\eta}, \quad (3.9)$$

where $\mathbf{k}'_{\parallel} = \mathbf{k}_{\parallel} + \mathbf{q}_{\parallel}$, ϖ denotes the Matsubara frequency, and

$$G_{\text{MS}}^{(0)}(i\varpi, \mathbf{k}_{\parallel}) = [i\varpi - d(k_z\sigma^1 - k_x\sigma^3)]^{-1}, \quad (3.10)$$

is the bare Green's function of the helical Majorana mode. In deriving (3.9) we have made use of (2.38) from Chp. 2. Note that since the surface state (3.8) only couples to y -polarized impurity spins, the FT-STs signal $\delta\rho_s^{\alpha\beta}$ vanishes for $\beta \neq 2$. Inserting the definition of the

Green's function $G_{\text{MS}}^{(0)}$ into (3.9) we obtain the integral

$$\Lambda_{\text{MS}}^{\alpha 2} = \int \frac{d^2 k_{\parallel}}{(2\pi)^2} \frac{(-v_0)L_{\text{MS}}^{\alpha}}{[\varpi^2 + d^2 k_{\parallel}^2][\varpi^2 + d^2 (\mathbf{k}_{\parallel} + \mathbf{q}_{\parallel})^2]}, \quad (3.11)$$

where the numerator is given by $L_{\text{MS}}^{\alpha} = (0, d\varpi q_x, d^2 \mathbf{k}_{\parallel} \cdot \mathbf{k}'_{\parallel} + \varpi^2, d\varpi q_z)$. The explicit solution to this integral can be found using the Feynman parametrization [147],

$$\Lambda_{\text{MS}}^{\alpha 2}(i\varpi, \mathbf{q}_{\parallel}) = \begin{cases} \frac{v_0}{2\pi d^2} \frac{q_x}{|\mathbf{q}_{\parallel}|} \zeta \mathcal{F}(\zeta) & \text{if } \alpha = 1 \\ -\frac{v_0}{2\pi d^2} \left[\frac{1}{2} \ln \left(1 + \frac{\Omega^2}{\varpi^2} \right) + \mathcal{F}(\zeta) \right] & \text{if } \alpha = 2 \\ \frac{v_0}{2\pi d^2} \frac{q_z}{|\mathbf{q}_{\parallel}|} \zeta \mathcal{F}(\zeta) & \text{if } \alpha = 3, \end{cases} \quad (3.12)$$

and $\Lambda_{\text{MS}}^{\alpha\beta} = 0$ otherwise. Equation (3.12) is expressed in terms of the function

$$\mathcal{F}(\zeta) = \frac{1}{\sqrt{-\zeta^2 - 1}} \arctan \frac{1}{\sqrt{-\zeta^2 - 1}}, \quad (3.13)$$

with the dimensionless variable $\zeta = 2\varpi / (\Delta_T |\mathbf{q}_{\parallel}|)$ and Ω is a momentum cutoff that sets the range of validity for the Dirac-type Hamiltonian (3.8).

We find the ordinary FT-STs signal $\delta\rho_s^{0\beta}$ in the presence of weak magnetic impurities vanishes identically. The spin-resolved FT-STs response $\delta\rho_s^{\alpha 2}$, with $\alpha \in \{1, 2, 3\}$, on the other hand, is nonzero and exhibits an inverse square-root singularity at the momenta $|\mathbf{q}_{\parallel,0}| = 2E/d$ (cf. Fig. 3.2). This singularity arises due to backscattering processes between states at momenta $+\mathbf{q}_{\parallel,0}/2$ and $-\mathbf{q}_{\parallel,0}/2$. Furthermore, $\delta\rho_s^{12}$ and $\delta\rho_s^{32}$ have an interesting angular dependence on the momentum transfer \mathbf{q}_{\parallel} with a twofold symmetry and nodes along the q_z and q_x axes, respectively. In contrast, $\delta\rho_s^{22}$ is circularly symmetric in \mathbf{q}_{\parallel} .

Arc surface states

At probe energies $E \ll d$, the universal physics of the arc surface states of centrosymmetric superconductors can be captured by the effective low-energy Hamiltonian

$$H_{\text{AS}}(\mathbf{k}_{\parallel}) = -dk_x \sigma^3 - v_0 \sigma^1, \quad (3.14)$$

where the surface momentum $\mathbf{k}_{\parallel} = (k_x, k_z)$ is restricted to the range $|k_z| < k_z^0$ and k_z^0 is half the length of the arc state in the surface Brillouin zone. In (3.14) the onsite potential $v_0 \sigma^1$ describes impurity spins polarized along the x axis. Interestingly, all other scattering

channels are absent due to symmetry constraints. We observe that the surface state (3.14) is fully polarized along the z spin axis, in contrast to arc states in noncentrosymmetric superconductors, which in general show finite spin polarizations both along the y and z directions, see Fig. 3.1(b).

Let us now compute the FT-STs response function for the arc state (3.14). Combining (3.14) with (2.26) we find that the QPI signal is given by (3.4) with $\Lambda^{\alpha\beta}(E, \mathbf{q}_{\parallel})$ replaced by

$$\Lambda_{\text{AS}}^{\alpha\beta=1}(E, \mathbf{q}_{\parallel}) = -\frac{v_0}{2}(-1)^\alpha \int \frac{dk_{\parallel}}{(2\pi)^2} \text{tr} \left[\sigma_\alpha G_{\text{AS}}^{(0)}(i\varpi, \mathbf{k}'_{\parallel}) \sigma_1 G_{\text{AS}}^{(0)}(i\varpi, \mathbf{k}_{\parallel}) \right]_{i\varpi \rightarrow E+i\eta},$$

where

$$G_{\text{AS}}^{(0)}(i\varpi, \mathbf{k}_{\parallel}) = \Theta(k_z^0 - |k_z|) [i\varpi + dk_x \sigma^3]^{-1} \quad (3.15)$$

is the Green's function of the unperturbed system, Θ denotes the unit step function, and $\mathbf{k}'_{\parallel} = \mathbf{k}_{\parallel} + \mathbf{q}_{\parallel}$. Because the arc state (3.14) only interacts with x -polarized magnetic impurities, the QPI pattern $\delta\rho_s^{\alpha\beta}$ is identically zero for $\beta \neq 1$. We now evaluate the above integral by first inserting the bare Green's functions and then performing the k_z integration. This gives

$$\Lambda_{\text{AS}}^{\alpha 1} = \int \frac{dk_x}{(2\pi)^2} \frac{v_0(|q_z| - 2k_z^0)\Theta(2k_z^0 - |q_z|)L_{\text{AS}}^\alpha}{[\varpi^2 + d^2k_x^2][\varpi^2 + d^2(k_x + q_x)^2]}, \quad (3.16)$$

where we have introduced the shorthand notation

$$L_{\text{AS}}^\alpha = (0, d^2k_x(k_x + q_x) + \varpi^2, d\varpi q_x, 0). \quad (3.17)$$

This integral can be computed explicitly to

$$\Lambda_{\text{AS}}^{\alpha 1}(i\varpi, \mathbf{q}_{\parallel}) = \begin{cases} \frac{v_0\varpi(|q_z| - 2k_z^0)\Theta(2k_z^0 - |q_z|)}{\pi d(4\varpi^2 + d^2q_x^2)} & \text{if } \alpha = 1 \\ \frac{v_0q_x(|q_z| - 2k_z^0)\Theta(2k_z^0 - |q_z|)}{2\pi(4\varpi^2 + d^2q_x^2)} & \text{if } \alpha = 2, \end{cases} \quad (3.18)$$

and zero otherwise.

Once again, we find the non-spin-resolved QPI patterns resulting from weak magnetic impurities are vanishing. The spin-polarized FT-STs signals, however, are finite and show an interesting dependence on momentum transfer \mathbf{q}_{\parallel} (cf. Fig. 3.3). For $\alpha \in \{1, 2\}$, $\delta\rho_s^{\alpha 1}$ exhibits a $1/q_x$ divergence at $|q_{x,0}| = 2E/d$. This singularity is due to backscattering processes among states with x momentum component $+q_{x,0}/2$ and $-q_{x,0}/2$. In addition,

we find that $\delta\rho_s^{11}$ is an even function of q_x , whereas $\delta\rho_s^{21}$ is odd in q_x .

3.4. Numerical results for noncentrosymmetric superconductors

In this section, we perform numerical simulations in noncentrosymmetric superconductors with both spin-orbit coupling (λ) and an admixture of singlet (ψ) and triplet (d) pairing symmetries. Unless stated otherwise, we set $(t, \mu, \lambda, \psi, d) = (4.0, 8.0, 2.0, 0.5, 2.0)$ for our numerical calculations and study the QPI patterns as a function of different types of SOC potentials. Since the spin polarization of the surface states is generic to NCSs and the absence of nonmagnetic backscattering is a consequence of time-reversal symmetry, different values for the parameters $(t, \mu, \lambda, \psi, d)$ do not qualitatively alter our results.

Helical Majorana modes

In Fig. 3.2 is shown the FT-STs response $\delta\rho_s^{\alpha\beta}$ of a helical Majorana mode on the surface of an O point-group NCS to nonmagnetic ($\beta = 0$) and magnetic impurities ($\beta \in \{1, 2, 3\}$). As opposed to centrosymmetric superconductors, we find that Majorana modes of NCSs couple to both nonmagnetic and magnetic scatterers with arbitrary spin polarization (cf. Sec. 3.3). Hence, $\delta\rho_s^{00}$ and $\delta\rho_s^{\alpha\beta}$ with $\alpha, \beta \in \{1, 2, 3\}$ are in general nonzero, whereas $\delta\rho_s^{0\beta}$ and $\delta\rho_s^{\alpha 0}$ with $\alpha, \beta \in \{1, 2, 3\}$ are, due to time-reversal invariance, vanishing within the Born approximation. Furthermore, we find that four pairs of elements of the FT-STs response tensor are related to each other by crystallographic point-group symmetries. Thus, we plot in Fig. 5.1 only the six independent nonzero elements of $\delta\rho_s^{\alpha\beta}$, which are either purely real or purely imaginary.

Interestingly, nonmagnetic impurities give rise to only a weak, nonsingular FT-STs response, see Figs. 3.2(a) and 3.2(g). This is due to the absence of elastic backscattering processes between states at momenta $+\mathbf{q}_{\parallel,0}/2$ and $-\mathbf{q}_{\parallel,0}/2$, where $|\mathbf{q}_{\parallel,0}| = 2E/d$. These nonmagnetic backscattering processes are prohibited by time-reversal symmetry, due to the opposite spin polarizations of states at opposite momenta. As a result, $\delta\rho_s^{00}$ only exhibits a kink at $|\mathbf{q}_{\parallel,0}|$, but no singularity. In the presence of magnetic impurities, however, spin-flip scattering processes are allowed. This leads to an inverse square-root singularity in $\delta\rho_s^{\alpha\beta}$ at $|\mathbf{q}_{\parallel,0}| = 2E/d$, see Figs. 3.2(h)–(l).

In passing, we point out some interesting features in the angular dependence of $\delta\rho_s^{\alpha\beta}$ on momentum transfer q_{\parallel} . As in the centrosymmetric case, the dependence of $\delta\rho_s^{\alpha\beta}$ on q_{\parallel} in Figs. 3.2(b)–(e) exhibits a π rotational symmetry about the origin, i.e., $\delta\rho_s^{\alpha\beta}(q_{\parallel}) = [\delta\rho_s^{\alpha\beta}(-q_{\parallel})]^*$. Twofold symmetries with high-symmetry lines along the vertical or horizontal axes, however, are absent. We observe that the different angular dependence between the

centrosymmetric and noncentrosymmetric cases is due to differences in the spin polarization, see Fig. 3.1(d). While in the centrosymmetric case, spin and momentum of the Majorana mode (3.12) are locked to each other at a right angle, in NCSs the angle between spin and momentum directions of the Majorana surface states differs by $\pm\pi/2$ and, moreover, varies strongly as a function of distance from the surface layer. This dependence of the spin polarization on layer index n results in the absence of any twofold mirror symmetries in the QPI patterns of Figs. 3.2(b)–(e).

Arc surface states

The FT-STs response of an arc state on the surface of a C_{4v} point-group NCS is shown in Fig. 3.3. In order to discuss energy and momentum dependence of these QPI patterns, we first point out that the arc surface state can essentially be viewed as a quasi-one-dimensional analog of the two-dimensional Majorana mode of the previous subsection. In other words, a description of the arc state can be obtained from the O point-group NCS by interchanging x and y components of the spin operator and by setting $k_z = 0$, see Eqs. (2.1e) and (2.1f). This explains the similarities in the QPI patterns of Fig. 3.3 with the response at $q_z = 0$ shown in Fig. 3.2.

As in Figs. 3.2(a) and 3.2(g), we find that the FT-STs signal produced by nonmagnetic impurities is weak and nonsingular, since spin-flip backscattering is prohibited by time-reversal symmetry. Hence $\delta\rho_s^{00}$ in Figs. 3.3(a) and 3.3(g) only shows a nondivergent kink- or peaklike feature at $|q_{x,0}| = 2E/d$. Magnetic impurities, on the other hand, give rise to a strong and divergent response in the spin-resolved FT-STs [see Figs. 3.3(b)–(f) and 3.3(h)–(l)]. Similar to (3.18), there is a divergence in $\delta\rho_s^{\alpha\beta}$ at $|q_{x,0}| = 2E/d$. We note that due to the different dimensionality of the momentum phase space, this is not an inverse square-root singularity as in Figs. 3.2(h)–(l), but shows a $1/q_x$ dependence.

Zero-energy flat bands

Finally, we discuss the FT-STs response of zero-energy flat bands on the surface of a C_2 point-group NCS, which is shown in Fig. 3.4. As before, we find that due to time-reversal symmetry the only nonzero elements of the response tensor $\delta\rho_s$ are $\delta\rho_s^{00}$ and $\delta\rho_s^{\alpha\beta}$ with $\alpha, \beta \in \{1, 2, 3\}$. Since lattice point-group symmetries relate four pairs of entries of $\delta\rho_s$ to each other [103], we plot in Fig. 3.4 only the six independent nonzero elements of $\delta\rho_s^{\alpha\beta}$.

The C_2 point-group NCS as defined by Eqs. (2.1) and (2.1g) exhibits two different zero-energy flat bands on the (010) surface, one with negative surface momentum $k_x < 0$ and one with positive momentum $k_x > 0$, see Figs. 3.1(c) and 3.1(f). Hence, in the presence of

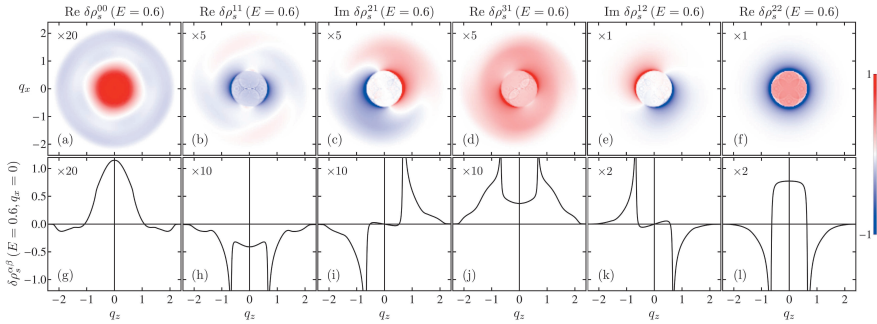


Figure 3.2. Ordinary and spin-resolved FT-STs interference patterns $\delta\rho_s^{\alpha\beta}(E, \mathbf{q}_{\parallel})$ arising from magnetic and nonmagnetic scattering processes on the surface of a fully gapped topological superconductor with cubic point group O . The top row shows density plots of $\delta\rho_s^{\alpha\beta}(E = 0.6, \mathbf{q}_{\parallel})$ as a function of momentum transfer $\mathbf{q}_{\parallel} = (q_x, q_z)$. The bottom row gives the corresponding cuts along the $q_x = 0$ line. Here we set $\lambda = -2.0$ and $\psi = 0.5$. The color scale for the density plots in panels (a)-(d) and the vertical scale in panels (g)-(l) have been multiplied by a factor as indicated for clarity.

impurities, it is useful to distinguish between interband scattering with momentum transfer $|q_x| \lesssim 1.0$ and intraband scattering with $|q_x| \gtrsim 1.0$, as indicated in Figs. 3.4(g)–(l) by the green dotted and black dashed ellipses, respectively.

Due to the opposite spin polarizations of the two zero-energy flat bands, time-reversal-preserving interband scattering is considerably suppressed [102]. Hence the part of the ordinary FT-STs signal $\delta\rho_s^{00}$ that corresponds to interband scattering [green dotted ellipses in Fig. 3.4(a)] is very weak, whereas the one corresponding to intraband scattering [black dashed ellipses in Fig. 3.4(a)] is strong and divergent. Magnetic impurities, on the other hand, give rise to both strong inter- and intraband backscattering. Consequently, the FT-STs response shown in Figs. 3.4(b)–(f) and 3.4(h)–(l) exhibits strong divergences both for large and small momenta transfer, i.e., within the regions in Figs. 3.4(b)–(f) bounded by green dotted and black dashed lines, respectively.

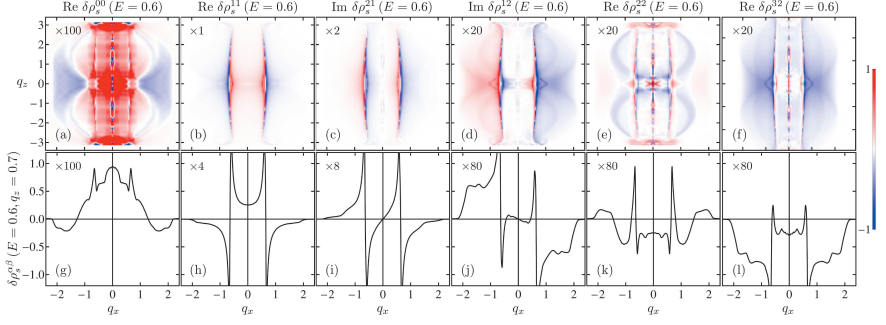


Figure 3.3. Ordinary and spin-resolved FT-STs response $\delta\rho_s^{\alpha\beta}(E, \mathbf{q}_{\parallel})$ for a nodal NCS with tetragonal point group C_{4v} , $\lambda = -2.0$, and $\psi = 0.5$. Top and bottom rows show density plots and cuts along the $q_z = 0.7$ line, respectively. The color scale for the density plots in (a)–(f) and the vertical scale in (g)–(l) have been multiplied by a factor as indicated for clarity.

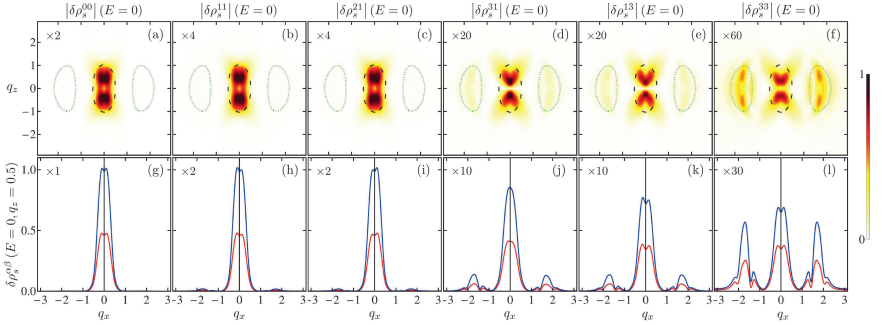


Figure 3.4. Amplitude of the ordinary and spin-resolved FT-STs signal $\delta\rho_s^{\alpha\beta}(E, \mathbf{q}_{\parallel})$ for a nodal NCS with flat-band surface states. Here, the SOC vector \mathbf{l}_k is given by (2.1g), $\lambda = 0.5$, and $\psi = 4.0$. The top row shows density plots of $\delta\rho_s^{\alpha\beta}(E = 0, \mathbf{q}_{\parallel})$ as a function of \mathbf{q}_{\parallel} for an intrinsic broadening $\eta = 0.005$. Green dotted and black dashed lines indicate the boundary of the regions corresponding to inter- and intraband scattering, respectively. Panels (g)–(l) display cuts of $\delta\rho_s^{\alpha\beta}(E = 0, \mathbf{q}_{\parallel})$ along the line $q_z = 0$ for $\eta = 0.005$ (red) and $\eta = 0.0025$ (blue). The color scale for the density plots in (b)–(f) and the vertical scale in (h)–(l) have been multiplied by a factor as indicated for clarity.

3.5. Conclusion

In summary, we have determined the universal features in the QPI patterns produced by magnetic and nonmagnetic impurities on the surface of time-reversal invariant topological superconductors. An explicit analytical expression was found for the energy and momentum dependence of the QPI patterns on the surface of centrosymmetric topological superconductors. For noncentrosymmetric systems, on the other hand, we have numerically determined the ordinary and spin-resolved FT-STs response.

Interestingly, for helical Majorana modes and arc surface states, we find that the ordinary QPI patterns resulting from nonmagnetic impurities are weak and nonsingular, which is in line with the expected absence of elastic backscattering. Similarly for flat-band surface states, the absence of backscattering suppresses the signal produced by scattering processes with large momentum transfer, hence, the non-spin-resolved FT-STs signal produced by nonmagnetic scattering processes connecting states with opposite momentum signs vanishes.

Magnetic impurities, on the other hand, give rise to a strong and divergent signal in the spin-resolved FT-STs for all three types of surface states. In the case of the helical Majorana modes, the divergent QPI patterns exhibit inverse square-root singularities at the momenta $|\mathbf{q}_{\parallel,0}| = 2E/d$, whereas for the arc surface states, the divergences in the FT-STs response at $|q_{x,0}| = 2E/d$ show a $1/q_x$ dependence.

Our results highlight the unique power of the FT-STs technique to detect topological surface states in unconventional superconductors. We have demonstrated that the FT-STs response allows us to clearly distinguish between the three different types of surface states that generically occur in time-reversal invariant topological superconductors. Moreover, the analysis of QPI patterns can be used to infer information about the pairing symmetry and the topological characteristics of the superconducting state [103].

4. Beyond low energy: Dirac edge and surface states

In this chapter, we ask ourselves how clean must a sample be in order to show topological surface states and how much the robustness of its surface states reveals about their topological nature. To this end, we consider fluctuations in the surface potential that are so large, that impurity states emerging from bulk-like states can localize on the sample's surface, with energies within the band gap. This follows from considering a strongly fluctuating disorder potential on the surface that explicitly breaks translational symmetry but neither of the global symmetries (cf. Sec. 1.2), which for noncentrosymmetric superconductors are time-reversal and particle-hole symmetries.

While the effects of disorder on topological superconductor surface states have been investigated extensively in terms of low-energy effective Dirac theories [77, 119, 148–150], the study of disordered Majorana states at the surface of bulk lattice models has remained an open problem. This is of relevance for experiments, since surfaces of unconventional superconductors are often intrinsically disordered, or can be disordered on purpose by depositing impurity atoms causing, for example, sputtering techniques.

To better appreciate the result in topological superconductors, we first make a digression into topological insulators, where experimental evidence of topological surface states is well established, and we can directly compare our predictions to direct measurements.

4.1. Bi_2Se_3 : A 3D topological insulator

The existence of a protected topological surface state in the form of chiral Dirac cones connecting valence and conduction bands has been verified for numerous topological insulators (TI) [19–23] by angle-resolved photoemission spectroscopy (ARPES). The predicted helical spin-structure and the influence of the lattice symmetry thereon has been experimentally verified by means of spin-resolved ARPES [24–28]. Its band structure is effectively well

described by a four-band model courtesy of Zhang *et. al.* [151, 152], which reads

$$\mathcal{H} = \frac{1}{2} \sum_{\mathbf{k}} \Phi_{\mathbf{k}}^{\dagger} H_{\mathbf{k}} \Phi_{\mathbf{k}}, \quad (4.1a)$$

with basis vector

$$\Phi_{\mathbf{k}} = (|p_{z,\mathbf{k}}^1, \uparrow\rangle, |p_{z,\mathbf{k}}^1, \downarrow\rangle, |p_{z,\mathbf{k}}^2, \uparrow\rangle, |p_{z,\mathbf{k}}^2, \downarrow\rangle)^T, \quad (4.1b)$$

corresponding to a four band vector including the hybridized p_z -orbitals of Bi and Se atoms. The single-particle Hamiltonian $H_{\mathbf{k}}$ is given by

$$H_{\mathbf{k}} = \epsilon_{\mathbf{k}} \sigma^0 \otimes \tau_0 + m_{\mathbf{k}} \sigma^0 \otimes \tau_3 + \sum_{i=0}^2 a_{\mathbf{k}}^i \sigma^i \otimes \tau_1, \quad (4.1c)$$

where the σ - and τ -matrices are Pauli matrices acting on spin and band space, respectively. The lattice has a rhombohedral unit cell with a lattice constants a in the ab-plane and c along the c-axis. This lattice model includes a kinetic term

$$\epsilon_{\mathbf{k}} = D_1(1 - \cos(k_z c)) + D_2(3 - 2 \cos(k_x \sqrt{3}a/2) \cos(k_y a/2) - \cos(k_y a)) - \mu, \quad (4.1d)$$

a mass term

$$m_{\mathbf{k}} = B_1(1 - \cos(k_z c) + B_2(3 - 2 \cos(k_x \sqrt{3}a/2) \cos(k_y a/2) - \cos(k_y a)) + M, \quad (4.1e)$$

and an inter-band coupling due to spin-orbit coupling,

$$a_{\mathbf{k}}^0 = A_0 \sin(k_z c), \quad (4.1f)$$

$$a_{\mathbf{k}}^1 = A_1 \sqrt{3} \sin(k_x \sqrt{3}a/2) \cos(k_y a/2), \quad (4.1g)$$

$$a_{\mathbf{k}}^2 = A_1 \cos(k_x \sqrt{3}a/2) \sin(k_y a/2) + A_1 \sin(k_y a). \quad (4.1h)$$

The parameters are fixed phenomenologically, in the numerical simulations we have used the same parameters as in Ref. [151]: $a = 4.08$; $c = 29.8$; $A_1 = 0.540$; $A_2 = 0.673$; $B_1 = 0.301$; $B_2 = 4.55$; $D_1 = 0.0391$; $D_2 = 1.57$; $\mu = -0.0068$; $M = 0.28$; In the absence of disorder, Eq. (4.1c) contains a spin polarized Dirac state (see Fig. 4.2(a)) on the crystal surface with origin in the band inversion at the Γ point, as has been widely reported for topological insulators. It has generally been the case, in these experiments, that only little attention has been given to the topological protection of the surface states against local disorder. The surface state protection is a property of the bulk TI: it comes from the non-trivial \mathbb{Z}_2

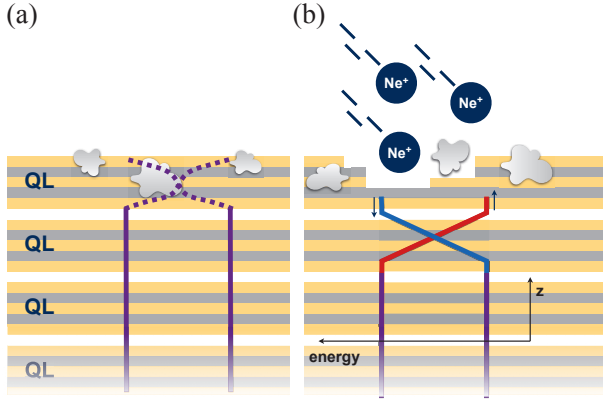


Figure 4.1. Scheme illustrating the sputtering by Neon ions of a Bi_2Se_3 surface with intrinsic contamination due to aging, water, or other depositions (represented as gray stains). Once the sample is sputtered, the topological surface states are forced into deeper layers in the crystal. QL stands for the quintuple layer unit cell of Bi_2Se_3 .

topological invariant defined for the bulk band structure [68]. Whenever in the topologically nontrivial phase a gapless Dirac mode emerges, localized at the interface, independent of the surface direction or interface chemistry. For Bi_2Se_3 the surface state appears not only for a Se terminated (111)-surface but also for any other chemically distinct surface [153]. Its existence can be probed indirectly by transport measurements on exfoliated thin films [154] and directly by ARPES, where the surface state of a Bi_2Se_3 thin film grown on a $\text{Si}(111) - (7 \times 7)$ substrate was fully mapped [155].

The surface of Bi_2Se_3 and other Bi-based topological insulators is found to adsorb H_2O or CO molecules upon exposure to air or carbon monoxide, respectively [156–158], introducing a large number of weak impurity scatterers on the surface and to surface doping. In turn, surface doping is known to induce a band bending and the development of two-dimensional surface quantum well states. Furthermore, the cleaving process is expected to create itself defects that can be either Se vacancies or distortions [27, 159]. In contrast with the topologically trivial quantum well states, the topological surface state is expected to withstand surface defects, keeping its ballistic nature. Nevertheless, it was reported in Ref. [159] that after gentle Neon sputtering not only the quantum well states but also the topological state disappears from the ultraviolet (UV) ARPES spectra. Explicit experimental evidence of the surface state protection is, hence, still missing. Here, we argue that the reason underlying

the reported disappearance of the topological surface state can be related to the limited probing depth of UV-ARPES, and show experimental evidence that the topological Dirac state survives a disordered environment.

We first determine numerically the robustness of topological surface states in Bi_2Se_3 , with a particular focus on the type of disorder, as it is clear from the discussion in Sec. 1.2 that the type of disorder can determine whether or not bound states get localized. We note that this question was first studied for a Gaussian disordered minimal model of topological insulators with cubic geometry and chiral symmetry, where it was shown that the surface states vanish for high enough disorder [160]. Here, we consider a realistic low-energy effective model for Bi_2Se_3 , and study the interplay between the two types of disorder introduced in Sec. 1.2.4. This analysis is complemented by the experimental results obtained via soft x-ray ARPES (SX-ARPES) for neon sputtered thin film samples. The ARPES signal is determined by calculating the momentum- and energy-resolved spectral weight, allowing for a good comparison to the experimental data. A scheme of the present scenario is found in Fig. 4.1.

The experimental data was collected by our collaborators J. Hugo Dil *et. al.* at the Swiss Light Source (SLS), and will be included in this manuscript.

4.1.1. Numerical simulation

The surface band structure of Bi_2Se_3 close to the center of the Brillouin zone is calculated by evaluating the Hamiltonian (4.1) discretized over a real space lattice, as defined in Eq. 3.3. In this way, surface defects such as the ones introduced by sputtering the crystal, can be included locally. Non-magnetic impurities will not lead to a disentanglement of these bands, nor to a change in the symmetry class of the sample, as only translational symmetry is broken. A slight broadening is expected to appear, but not enough to render the topological insulator trivial. That is to say the bulk topological invariant remains unchanged, and a topological surface state is inevitably expected.

We include perturbations in the model by considering a scattering potential that preserves time-reversal symmetry. This is generally defined by

$$\delta\mathcal{H} = \sum_{\mathbf{k}, \mathbf{q}_{\parallel}} \sum_{i=G,U} \Phi_{\mathbf{k}}^{\dagger} \sigma^0 \otimes (v_i^m(\mathbf{q}_{\parallel})\tau_3 + v_i^{\mu}(\mathbf{q}_{\parallel})\tau_0) \Phi_{\mathbf{k}+\mathbf{q}_{\parallel}}, \quad (4.2)$$

where $v_{G(U)}^{\mu(m)}(\mathbf{q}_{\parallel})$, labeling Gaussian (v_G) and unitary (v_U) disorder strength can be arbitrarily large and are obtained from the Fourier transformation of their real space definitions. Two contributions are considered for the total form of the impurity potential:

- i *Gaussian disorder*, consisting of uncorrelated random values taken from a box distribution

$v_G(\mathbf{r}) \in]-\gamma/2, \gamma/2[$ with strength γ at all surface sites, this type of disorder simulates fluctuations in the surface electrostatic potential as well as local gap fluctuations, which in turn simulate a general symmetry preserving surface aging and contamination.

- ii *Unitary disorder*, consisting of dilute strong scatterers, $v_U(\mathbf{r}) = \sum_i 10^5 \delta(\mathbf{r} - \mathbf{r}_i)$, where the sites \mathbf{r}_i 's are uniformly distributed in the sample's surface, which simulates the effect of sputtering by Neon atoms. These can result in both attachment of the Neon atom to the surface or mechanical removal of some of the surface constituents, resulting in very strong local and dilute impurities.

The disordered surface of the sample can be well recognized by calculating the momentum resolved density of states [160, 161].

$$I(\omega, k, l) = -\frac{1}{\pi\sqrt{\mathcal{N}}} \text{Im} \sum_{n\nu} \frac{\left| \sum_{r_{\parallel}} \Psi_{n,\nu l}(r_{\parallel}) e^{-ik \cdot \hat{\mathbf{k}} \cdot r_{\parallel}} \right|^2}{\omega - E_n + i\eta}, \quad (4.3)$$

with n, ν and l the eigenstate, band and layer indices, and η a small broadening parameter associated with the quasiparticle's lifetime (fixed in the numerical simulations to $\eta = 0.02$) and \mathcal{N} the total number of sites integrated over. The low-energy real space eigenfunctions $\Psi(\mathbf{r})$ and respective energies E_n are computed using the Arnoldi scheme [162]. The intensity is calculated at the binding energy ω and momentum k , which is taken along the crystallographic direction $\bar{\Gamma}-\bar{M}$, to coincide with the experimental data. All calculations were performed at zero temperature.

At very high sputtering intensities, the sample is expected to form crystal cracks introducing mismatches in the bulk unit cell orientations, and consequently leading to bulk disorder. This type of disorder was not considered in our numerical calculations. Yet, in this limit we expect the signal at Γ to become fuzzy, eventually opening a gap as the bulk topology is slowly destroyed.

We conclude that for moderate amounts of surface contamination, the surface density of states is not affected. Sputtering these samples has the same effect as sputtering clean ones, in particular it leads to a migration of intensity towards inner layers. The sharpness of the measurement should, however, remain unaffected. In contrast are surfaces contaminated with average electrostatic potentials well above the energy gap. These strong fluctuations allow for impurity bands to form on the surface of the sample, independent of the topological nature of the bulk. Ingap impurity states go beyond our treatment of low-energy Dirac states in chapters 2 and 3 as they are physically localized in the surface but do not have the dispersion or spin-momentum locking characteristic of the Dirac cone. Such impurity states allow for scattering channels not previously accounted for, resulting in avoided crossings and level

repulsion between states all states present in the surface. This can be clearly seen in Fig. 4.2 (c), where the sample with 5 eV surface contamination¹ shows a diffusive character rather than ballistic (cf. discussion in Sec. 1.2), that is the spin conductance associated with the boundary mode of the TI should not remain quantized. Consequently, sputtering the sample has a "cleaning" effect on the strongly diffusive surface, as it effectively increases the energy it takes an electron to populate the outer layer, successfully reducing the disorder potential felt by the quasiparticles by developing a dead layer at the surface. Again, the topological surface states are pushed down to clean layers, recovering their linear dispersion and sharp ARPES signal.

4.1.2. Experimental results²

Figure 4.3 shows the SX-ARPES spectra of Bi_2Se_3 along the $\bar{\Gamma}-\bar{M}$ crystallographic direction using photon energies of 380 eV and 725 eV. The sputtering was performed with Ne^+ ions at 0.7 keV and $3 \cdot 10^{-6}$ mbar for 7 s, 22 s, 52 s and 112 s. The samples were prepared at a temperature of 10 K and sputtered at room temperature to prevent the sputtering agent from freezing. To assure homogeneous aging, the time between cleaving, cooling and measuring was kept constant for all samples. These measurements were performed at the ADRESS beamline of the Swiss Light Source.

The spectra of the unsputtered sample shows a blurry bulk band at both photon energies, and the linearly dispersing branches cannot be clearly identified. In contrast, for a slightly sputtered surface (7 s – 22 s), a significant enhancement of the data quality of the measured band maps is observed. We note that for these sputtering times, the overall spectral intensity and signal to noise ratio are strongly increased in contrast to the reported UV-ARPES measurements with similar sputtering conditions [159]. For longer sputtering times (52 s in Fig. 4.3) the spectral intensities of the bulk states start to decrease again and the signal to noise ratio deteriorates. The same is true for the signal from the topological surface state, however it is still clearly visible. At 112 s, the defects introduced are of such high degree that the surface topography is changed. The crystal surface shows multiple tilted domains, leading to strongly varying normal emission angles depending on the location of the synchrotron light spot. This indicates that the domains are similar in size to the beam spot ($74 \times 30 \mu\text{m}$).

¹This value should not be directly compared with experiment, as the number of impurity states in the numerical calculation depends on the bandwidth of the model, which fits only accurately the Bi_2Se_3 band structure for small momenta and energies.

²The information contained in this section and the experimental data are of the authorship of our experimentalist collaborators Gabriel Landolt, J. Hugo Dil *et. al.* It is included in this thesis for completeness.

4.1.3. Discussion

The surface of Bi_2Se_3 is susceptible to large amounts of surface contamination due to the cleaving procedure and aging. Aging can be manifested for example by the adsorption of water vapour or other molecules, leading to surface doping and quantum well states [156–158]. This sort of sample contamination can lead to strong fluctuations of the electrostatic potential, for which we have demonstrated that the topological surface mode loses its sharp quasiparticle peak in Fourier space. Namely, it can lead to a fully smeared out signature in the momentum resolved spectral function, rendering it indistinguishable from a trivial phase with ARPES measurements. We have shown in our numerical analysis (cf. Fig. 4.2) that sputtering can circumvent this problem by eliminating the contaminated layer. The controlled introduction of unitary disorder will lead to a re-emergence of the fully delocalized topological surface state at inner layers.

Furthermore, we have shown experimental evidence for an astonishing robustness of the topological surface state of Bi_2Se_3 against sputtering induced defects, probed by SX-ARPES. This is in remarkably good agreement with our numerical simulations, where strong surface scatterers are distributed along the surface at a fixed average density. The random vacancies force the surface state into inner layers of the thin film, where potential fluctuations due to adsorbates and quantum well states is minimal. That is, the Gaussian contribution to the total disorder affecting the surface state is strongly suppressed and the ARPES signal becomes sharper. Furthermore, we note that the retreat of the topological surface state is most likely happening in steps of five atomic layer, i.e., the full unit cell of Bi_2Se_3 [27]. The resulting deep burial of the surface state can justify its immediate disappearance after slight sputtering when measured with low-probing depth techniques such as UV-ARPES [159]. The re-emergence of the ARPES signal after induced unitary disorder by sputtering provides a direct confirmation of both the topological origin and the characteristic robustness of the surface state. This is of importance for potential spintronics systems, which rely on stable spin channels.

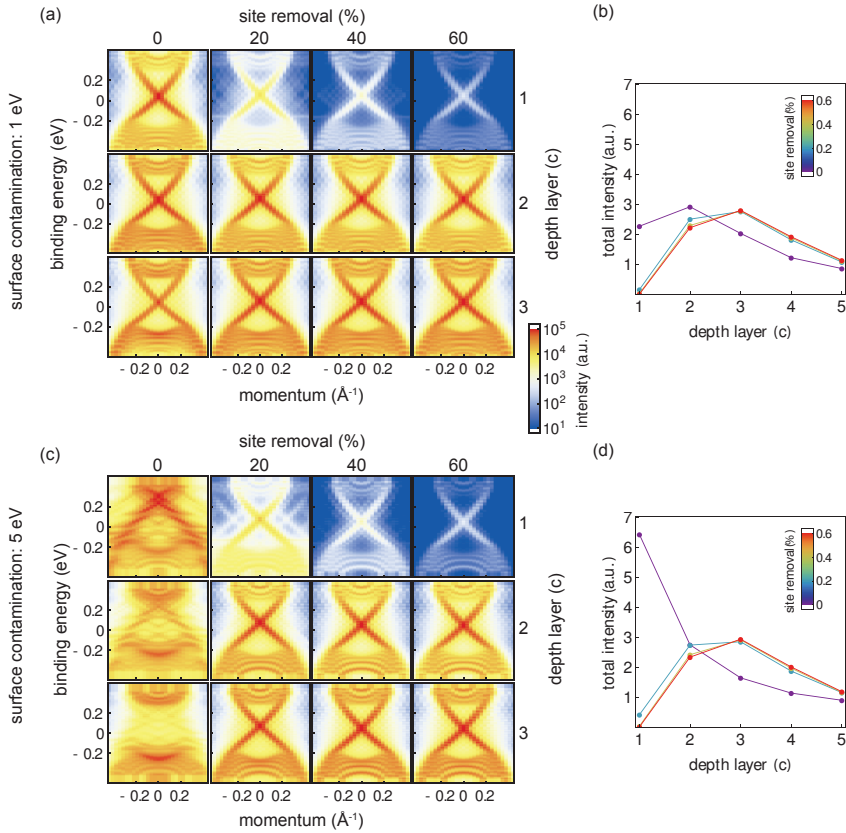


Figure 4.2. Numerical simulation of dirty Bi_2Se_3 for two values of surface contamination (a) 1 eV (2Δ), showing no sign of disturbance to the topological surface state. (b) 5 eV (10Δ), showing a coupling of the surface state with impurity states. Sputtering leads to site removal on the first layer and a consequent migration of the surface states to the second and third layers. (b) and (d) total intensity as a function of depth layer for plots (a) and (c), respectively.

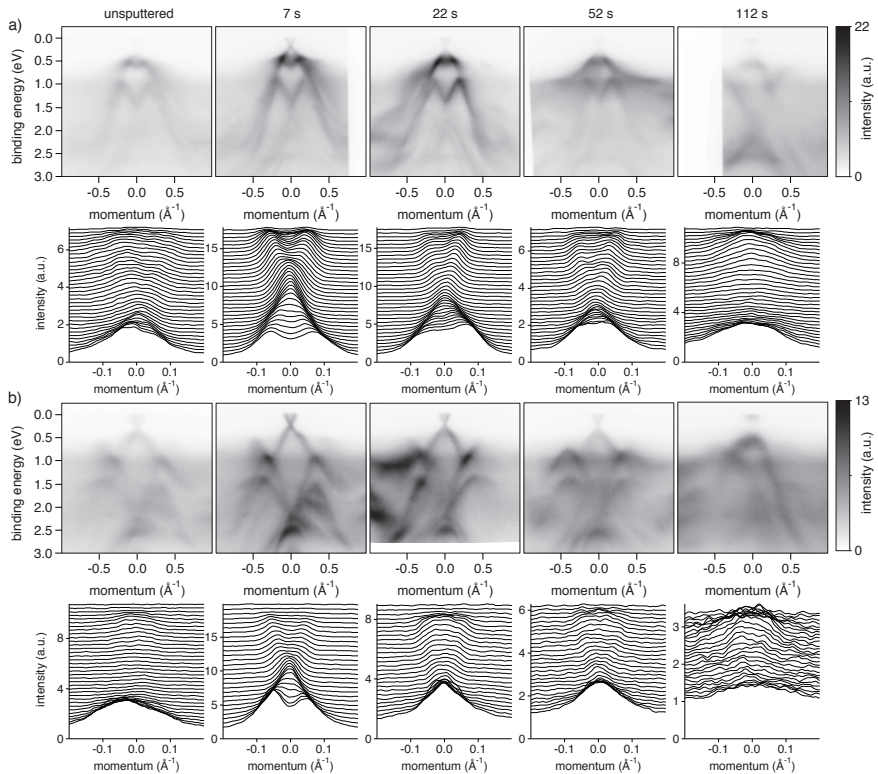


Figure 4.3. (a) Soft X-ray ARPES band map for 380 eV photon energy after different amounts of neon sputtering. The measurement conditions are held fixed for the different samples. The lower panels show constant energy cuts through the Dirac cone taken at 130 meV intervals. (b) Same as (a) but measured at 725 eV photon energy.

4.2. Topological superconductors:

${}^3\text{He}(\text{B})$ and NCS ($s + p$)-wave superconductor

Fully gapped noncentrosymmetric superconductors with strong spin-orbit coupling and the B phase of superfluid ${}^3\text{He}$ [56, 163, 164] have been proposed as candidate materials for time-reversal invariant topological superconductors and superfluids hosting helical Majorana states. In sections 2.4 and 3.4 we have shown the helical spin texture which protects them from backscattering off of nonmagnetic impurities. This is, however, fully analogous with Dirac states in topological insulators such as Bi_2Se_3 , for which we have shown in the previous section that strong enough surface disorder can be destructive. Furthermore, as the experimental results evidence, such disorder strengths are realistic in normal the aging and exposure processes to which topological insulators are subject.

In this section we study in detail whether Majorana surface states of three dimensional topological superconductors are robust to symmetry preserving disorder, comparing them to the Dirac states on the surface of topological superconductors.

First, let us note that in contrast with Dirac surface states, the Majorana mode does not couple to electromagnetic fields, its dispersion can thus only be detected by applying an effective gravitational field, i.e., a temperature gradient or rotations of the superconductor [120–122]. It has been proposed, as an example, that surface states could be observed by detecting gravitational waves in the spin relaxation rate of an electron bubble [165]. At zero energy one helical Majorana surface mode carries a quantized thermal conductance.

We have shown that no relevant or marginal time-reversal symmetric perturbation can be added to the surface Dirac Hamiltonian, making the helical Majorana state robust against the influence of weak disorder and interactions [77, 122, 148]. Only variations of the Fermi velocity are allowed as a symmetry preserving deformation of the effective Dirac equation describing the surface state, and hence an energy gap cannot be opened in the surface spectrum.

In the following, we consider surface disorder with strength γ which leads to a breakdown of the effective low-energy theory. Again, such a scenario is achieved by forcing a critical amount of impurity bound states onto the surface, with energies within the bulk gap. That is, we consider disorder with $\gamma \geq \Delta$ for which induced coupling between the surface and bulk states needs to be taken into account. We determine the role of particle hole symmetry in the protection of surface states, and we examine the ways in which two- and three-dimensional topological superconductors in the symmetry class DIII respond differently to strong disorder.

To investigate the effects of strong surface impurities on the surface and bulk quasiparticle wave functions, we employ large-scale numerical simulations of two- and three-dimensional

Bogoliubov-de Gennes (BdG) lattice Hamiltonians (2.1) and compute the local density of states and level spacing statistics of the wave functions, cf. Sec. 1.2.

4.2.1. Numerical simulation

For our numerical calculations, we set the model parameters to $t = 4.0$, $\lambda = 2.0$, $\psi = 0.5$, and $d = 2.0$. For the three-dimensional NCS with SOC (2.1e) we set the chemical potential to $\mu = 8.0$, whereas for the two-dimensional NCS with SOC (2.1f) we set $\mu = 4.0$. With this parameter choice the two- and three-dimensional boundary states decay into the bulk with a decay length of the order of three lattice spacings (cf., Sec. 2.4). Using exact diagonalization algorithms [162] we compute the eigenenergies E_n and eigenstates Ψ_n of $H_{\mathbf{k}}$, (2.1), in the presence of surface disorder described by (2.12). The effects of surface impurities are best revealed in the local surface density of states,

$$\rho_l(\omega, \mathbf{r}_{\parallel}) = -\frac{1}{\pi} \text{Im} \sum_{\nu=1}^4 \sum_m \frac{|\Psi_{n,\nu l}(\mathbf{r}_{\parallel})|^2}{\omega - E_n + i\eta}, \quad (4.4)$$

and the momentum-resolved spectral function given by (4.3). Here, instead, $\hat{\mathbf{k}}$ is taken along the $\hat{\mathbf{x}}$ direction, \mathbf{r}_{\parallel} are the surface sites, l represents the layer index, and ν is the combined spin and particle-hole index. The expressions (4.3) and (4.4) are evaluated in real space with an intrinsic broadening $\eta = 0.05$ for finite lattices of size $50 \times 20 \times 30$ in three dimensions and 1000×40 in two dimensions, unless otherwise stated. To compute the density of states of two-dimensional topological NCSs (Figs. 4.9 and 4.8), we employ the recursive Green's function technique described in Appendix B, which is numerically more efficient than direct diagonalization for low dimensions.

To obtain insight into the localization or delocalization properties of the surface states, it is useful to compute the probability distribution of the local density of states, $P[\tilde{\rho}_l(\omega)]$, and the level spacing distribution function $P(s)$, as discussed in Sec. 1.2. The probability distribution $P[\tilde{\rho}_l(\omega)]$ is defined in terms of the local density of states on the l -th layer normalized to its mean value $\langle \rho_l(\omega) \rangle$ [166],

$$\tilde{\rho}_l(\omega) = \rho_l(\omega) / \langle \rho_l(\omega) \rangle. \quad (4.5)$$

A distribution centered at $\tilde{\rho}_l(\omega) = 1$ corresponds to extended states, while a distribution peaked at zero indicates localized states. The level spacing distribution function $P(s)$ (1.33),

on the other hand, is given in terms of the normalized spacing

$$s = \frac{|E_n - E_{n+1}|}{\delta(E_n)}, \quad (4.6)$$

between two nearest levels E_n and E_{n+1} with $\delta(E_n)$ the mean level spacing near E_n . We note that for systems with a density of states that changes rapidly with energy [see, e.g., Fig. 4.5(a)], the normalization of the level spacing intervals by the mean level spacing $\delta(E_n)$ is particularly important [37, 167]. In a disordered quantum system the energy level distribution reflects the localization properties of the system [37, 39]. In a delocalized phase, nearby energy levels repel each other leading to a Wigner-Dyson-like level statistics. In a localized phase, however, different levels can be arbitrarily close to each other, which gives rise to Poisson statistics.

4.2.2. Three-dimensional topological NCS

We start by discussing the effects of nonmagnetic disorder on the helical Majorana states of three-dimensional topological NCSs. Figures 4.4(a)-(e) show the spectral function $I(\omega, k, l)$ integrated over the three outermost layers, which is of the order of the decay length of the ingap surface states. In the clean case, $\gamma = 0$, surface states exist at energies smaller than the bulk energy gap $\Delta = d - \psi = 1.5$ and form a helical Majorana cone, which is centered at the Γ point of the surface Brillouin zone, see Fig. 4.4(a). In accordance with the discussion of Sec. 2.4, we find that weak and even moderately strong disorder leaves the spectral function almost unchanged, apart from small broadening effects, as seen in Figs. 4.4(b) and 4.4(c). Conversely, strong surface disorder with strength of the order of the band width, $\gamma \simeq 5t$, completely destroy the momentum-space structure of the ingap surface states and leads to a large increase of the density of states in the surface layers, leading to an overall darker tone in Fig. 4.4(d). For this disorder strength, the wave function probability densities $|\Psi_m(l, r)|^2$ exhibit sharp peaks spread through the entire layer, see Figs. 4.6(i) and 4.6(j). The real-space structures of $|\Psi_m(l, r)|^2$ for different wave functions with nearby energies are correlated, forming clusters of differently colored peaks. In other words, the surface state wave functions show signs of critical delocalization. Finally, for extremely strong impurity scatterers $\gamma \gg t$, almost fully localized impurity states are formed in the surface layer, that is, functionally transforming into unitary disorder impurities, while in the second and third outermost layers extended states reemerge, forming helical Majorana bands, Figs. 4.4(e) [160, 161].

In Figures 4.6(a)-(h) we show the layer and energy-resolved probability distribution of $\tilde{\rho}_l(\omega)$ for disorder strengths $\gamma = 5t$ and $\gamma = 30t$.³ For $\gamma = 30t$, the probability distribution

³As the ingap states are unperturbed, we cannot create a random ensemble to extract statistical properties. The level

$P[\tilde{\rho}_l(\omega)]$ in the surface layer $l = 1$ is peaked at $\tilde{\rho}_l = 0$, which signals localization, whereas $P[\tilde{\rho}_l(\omega)]$ for the inward layers $l = 2$ and $l = 4$ has a maximum close to $\tilde{\rho}_l = 1$, indicating delocalized states. We further note that the surface state wave function has a node in layer $l = 3$ and therefore $P[\tilde{\rho}_l(\omega)]$ for $l = 3$ is peaked closer to $\tilde{\rho}_l = 0$, see Fig. 4.6(g). With decreasing energy, the maximum of the distributions in Figs. 4.6(f) and 4.6(h) approaches $\tilde{\rho}_l = 1$, which shows that the states with energies near zero (in particular the Majorana zero-energy states) are more extended than those states with energies of the order of $\Delta/3$. For $\gamma \simeq 5t$, corresponding to the crossover from weak to strong disorder, $P[\tilde{\rho}_l(\omega)]$ in all four layers shows a broad peak, which we interpret as a sign of critical delocalization, cf. Figs. 4.6(i) and 4.6(j) [167].

The disorder-averaged total density of states $\rho_{\text{tot}}(\omega) = \sum_l \sum_{r_n} \rho_l(\omega, r_n)$ in Fig. 4.5(a) reveals that for $\gamma = 5t$ there exists a large number of ingap states, which completely fill up the superconducting gap. For even larger disorder strength, $\gamma \gg t$, on the other hand, the number of ingap states is reduced, indicating that the effects of disorder on the superconductor and its surface states become effectively weaker. Importantly, we find that for all disorder strengths and disorder configurations there exist two extended zero-energy Majorana surface states. These zero-energy modes appear in the total density of states of Fig. 4.5(a) as a narrow peak at $\omega = 0$.

Finally, we present in Fig. 4.5(b) the level spacing distribution function $P(s)$ for ingap states with energies within the interval $|\omega| < \Delta/3$ in the presence of surface disorder with strength $\gamma = 5t$ and $\gamma = 30t$. Interestingly, we find that for $\gamma = 5t$ the level statistics $P(s)$ fits the generalized Wigner surmise for the symmetry class DIII (i.e., $\alpha = 1$ and $\beta = 4$) [37, 39]. This indicates that the ingap states remain delocalized with significant overlap, giving rise to level repulsion. For $\gamma = 30t$, however, there are deviations from the generalized Wigner surmise, which we attribute to the emergence of localized states in the strongly disordered surface layer $l = 1$ with energies of the order of $\Delta/3$. These localized states do not exhibit level repulsion and hence lead to Poissonian level spacing statistics, which is superimposed on the class DIII level statistics of the extended states with energies close to zero. Importantly, we note that for $\gamma \gtrsim 5t$ the ingap surface states are strongly coupled to the bulk states and therefore can no longer be described by an effective *single-valley*, i.e. two-component Dirac Hamiltonian of the form of (2.39), for which all impurity terms are forbidden by symmetry and therefore no random ensemble with a universal level spacing statistics can be achieved.

spacing distribution shows a sharp peak centered at 1, evidence of the unperturbed linear dispersion, as well as the density of states distribution, evidence of the fully extended states. This quantities are, therefore, only calculated for the strong disorder limit.

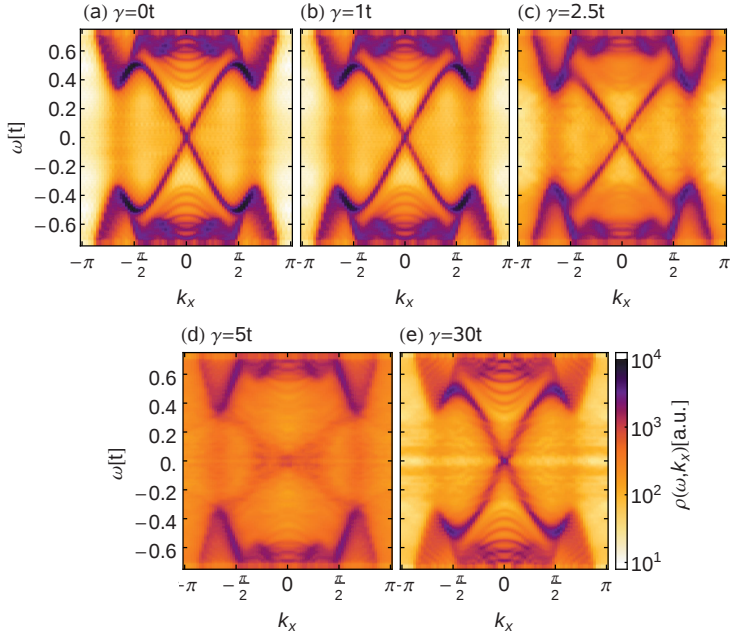


Figure 4.4. Spectral function $I(\omega, \mathbf{k}_{\parallel})$, Eq. (4.3), on a log scale as a function of energy ω and surface momentum k_x with $k_y = 0$ for the first three outermost layers at the (001) surface of a three-dimensional topological NCS. The strength γ of the Gaussian distributed surface disorder increases from $\gamma = 0t$ in (a) to $\gamma = 30t$ in (e).

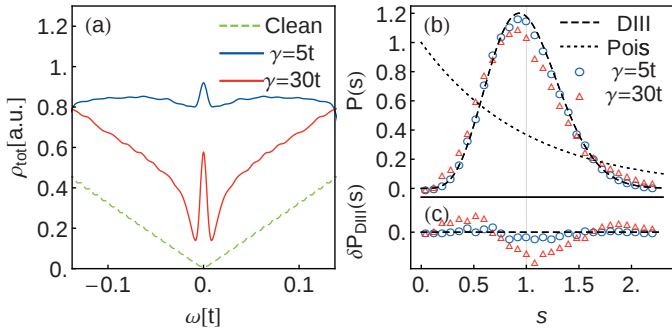


Figure 4.5. (a) Disorder-averaged total density of states $\rho_{\text{tot}}(\omega)$ for a three-dimensional topological NCS with disorder strength $\gamma = 5t$ (blue solid line) and $\gamma = 30t$ (red solid line). The average is taken over 1000 disorder configurations. For comparison, the green dashed line displays the density of states of a clean Majorana cone. (b) Level spacing distribution function $P(S)$ for ingap states with energies within the interval $|\omega| < \Delta/3$ with two different disorder strengths $\gamma = 5t$ (blue circles) and $\gamma = 30t$ (red triangles). The black dashed line is the generalized Wigner surmise for class DIII (i.e., $\alpha = 1$ and $\beta = 4$). The black dotted line represents the Poisson distribution. (c) Difference between the numerical data and the class DIII level statistics.

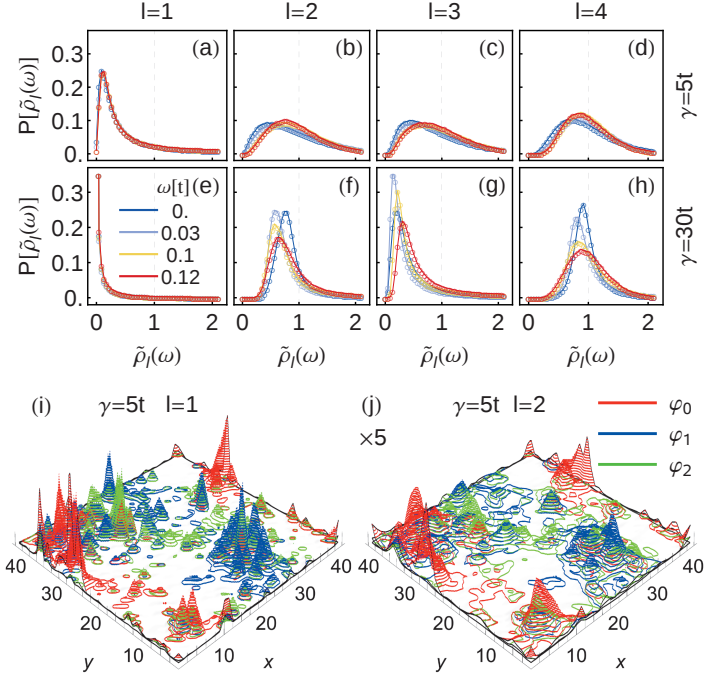


Figure 4.6. (a)-(h) Layer and energy-resolved probability distribution $P[\tilde{\rho}_l(\omega)]$ of the normalized local density of states $\tilde{\rho}_l(\omega)$ for an ensemble of one hundred disordered three-dimensional topological NCSs, with disorder strengths $\gamma = 5t$ [panels (a)-(d)] and $\gamma = 30t$ [panels (e)-(h)]. Each column shows the probability distribution $P[\tilde{\rho}_l(\omega)]$ for a different layer, with $l = 1$ the surface layer [panels (a) and (e)] and $l = 4$ the 4th inward layer [panels (d) and (h)]. The energy dependence is indicated by the color scale, with blue representing $\omega = 0$ and red $\omega = \Delta/3$. Panels (i) and (j) show the wave function probability density $|\Psi_m(l, \mathbf{r})|^2$ in the first ($l = 1$) and second inward layer ($l = 2$), respectively, for the three lowest positive energy wave functions φ_0 , φ_1 , and φ_2 with successive eigenvalues $E_0 = 0 < E_1 < E_2$ (red, green, blue), at the disorder strength $\gamma = 5t$. We find that at this disorder strength the wave functions show signs of critical delocalization. The amplitude in panel (j) has been multiplied by a factor of 5 for clarity. Ψ_0 (red) is the helical Majorana state at exactly zero energy.

4.2.3. Two-dimensional topological NCS

Secondly, we examine the helical Majorana states at the edge of a 2D topological NCS with nonmagnetic edge disorder. In Fig. 4.7 we present the spectral function $I(\omega, k_x, l)$, (4.3), summed over the three outermost layers. As for the 3D NCS, we find that in the clean case edge states appear at energies smaller than the bulk gap Δ , forming two Majorana bands that cross at $k_x = 0$ of the surface Brillouin zone, see Fig. 4.7(a). As a consequence of TRS, ingap states with opposite edge momenta have opposite spin polarization [101–103, 168]. This completely prohibits backscattering among the edge states by nonmagnetic impurities. Moreover, as discussed in Sec. 2.4, the only symmetry allowed perturbations of the edge Hamiltonian (2.27), are local variations of the superconducting gap Δ , i.e., changes in the Fermi velocity of the Majorana bands. Hence, one expects that nonmagnetic disorder with strength $\gamma \leq \Delta$ does not affect the surface states, which is confirmed by our numerical results in Fig. 4.7(b).

For stronger edge disorder with γ of the order of the bandwidth $5t$, the spectral function $I(\omega, k_x, l)$ becomes smeared out, but a momentum-space dispersion is still visible. We find that for this disorder strength, extended edge states forming Majorana bands, strongly interact with more localized ingap states. Moreover, comparing Figs. 4.7(a) and 4.7(b), we observe that edge disorder significantly modifies the Fermi velocity of the Majorana modes, particularly around zero energy. Interestingly, at $\gamma = 5t$ the probability distribution $P[\tilde{\rho}_l(\omega)]$ is strongly broadened (Fig. 4.9(a)-(d)) and the disorder-averaged total density of states $\rho_{\text{tot}}(\omega)$ exhibits a pronounced peak at $\omega = 0$ (blue trace in Fig. 4.8). The latter is reminiscent of the Dyson singularity at zero-energy which occurs in (quasi)-one dimensional dirty superconductors belonging to symmetry class DIII [169, 170]. That is, the spectral function of Fig. 4.7(d) and the total density of states of Fig. 4.8 indicate that extended ingap states coexist with critically delocalized states at the edge of the superconductor. Further increasing the disorder strength to $\gamma = 30t$, we observe that the number of ingap states decreases, the height of the zero-energy peak in ρ_{tot} is reduced significantly, and the Majorana bands recover a perfectly linear dispersion (Fig. 4.7(e) and red trace in Fig. 4.8). This shows that the effects of the edge disorder on the bulk superconductor and its Majorana ingap states effectively decreases for $\gamma \gg t$. In fact, just as for the 3D topological superconductor, very strong impurity scatterers give rise to almost fully localized edge states in the surface layer, while the extended states that form the Majorana bands are now mostly located in the second and fourth outermost layers (Fig. 4.9(e)-(h)). Overall, we find that disorder affects the Majorana modes of 2D topological NCSs less strongly than those of 3D topological NCSs. In part, this is due to the helical spin texture of the Majorana modes, which completely prohibits backscattering at the one-dimensional NCS edge, whereas it only partially suppresses scattering across the Majorana cone of a 3D topological NCS.

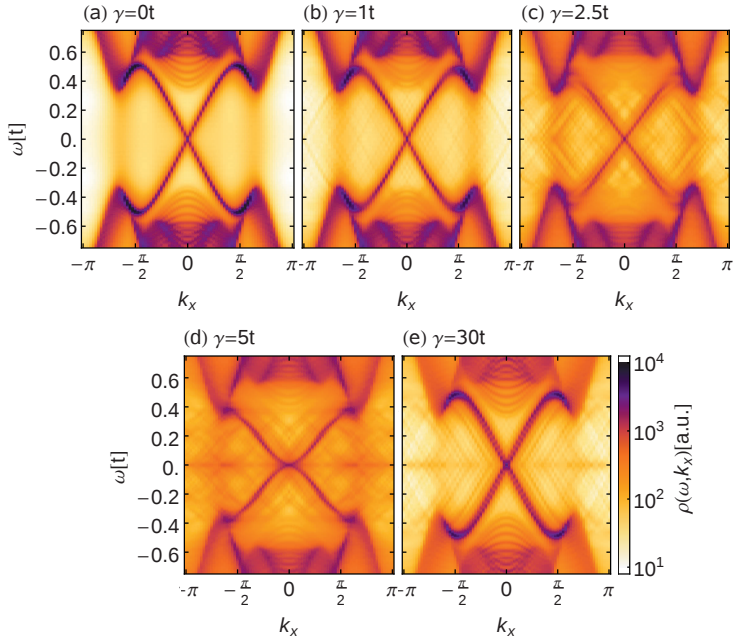


Figure 4.7. Spectral function $I(\omega, k_x, l)$ on a log scale as a function of edge momentum k_x for the first three outermost layers at the (01) edge of a two-dimensional topological NCS on a square lattice of size 80×40 . The strength of the edge disorder increases from $\gamma = 0t$ in (a) to $\gamma = 30t$ in (e).

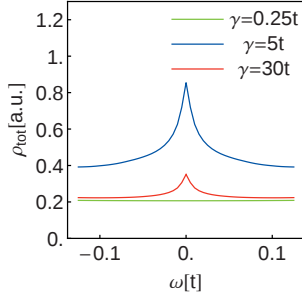


Figure 4.8. Disorder-averaged total density of states $\rho_{\text{tot}}(\omega)$ for a two-dimensional topological NCS with disorder strengths $\gamma = 0.25t$ (green), $\gamma = 5t$ (blue), and $\gamma = 30t$ (red). The average is taken over 100 disorder configurations.

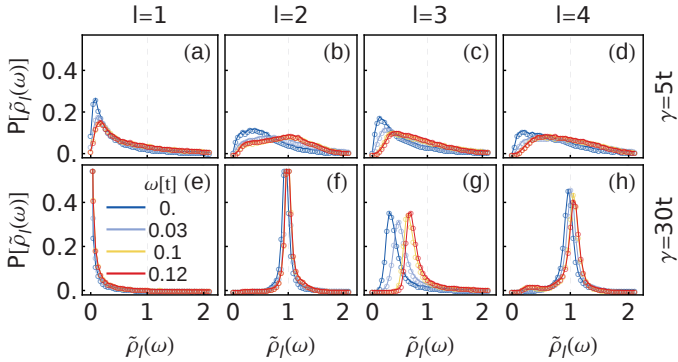


Figure 4.9. (a)-(h) Layer and energy-resolved probability distribution $P[\tilde{\rho}_l(\omega)]$ of the normalized local density of states $\tilde{\rho}_l(\omega)$ for an ensemble of one hundred disordered two-dimensional topological NCSs with disorder strengths $\gamma = 5t$ and $\gamma = 30t$. The energy dependence is indicated by the color scale, with blue representing $\omega = 0$ and red $\omega = \Delta/3$. Each column shows the probability distribution $P[\tilde{\rho}_l(\omega)]$ for a different layer.

4.2.4. Magnetic surface disorder

Magnetic surface disorder lifts the time-reversal symmetry protection of the helical Majorana cone and therefore can induce a full gap in the surface spectrum. In Figs. 4.10(a)-(b) we show the spectral function $I(\omega, k_x, l)$ integrated over the three outermost layers at the (001) surface of a three-dimensional topological NCS in the presence of magnetic impurities $V_r^{x,y,z} = v(r)S^{x,y,z}$, (2.12), polarized along the x , y , and z axes. We find that whether the Majorana state is gapped out by magnetic disorder with $\gamma \leq \Delta$, depending on the direction in which the impurity spins are polarized. As discussed in Sec. 2.4, the Majorana bands couple most strongly to the z component of the impurity spins, since they exhibit a strong z -spin polarization [101–103, 168]. Hence, z -polarized impurity spins open up a full gap in the surface spectrum, as clearly observed in Fig. 4.10(c), inducing a thermal quantum Hall state at the surface [171]. On the other hand, y -polarized impurities only couple weakly to the Majorana cone, whereas x -polarized impurity spins do not affect the surface states at all, since the polarization of the Majorana bands has zero component along the x axis, see Figs. 4.10(a) and 4.10(b).

A similar behavior is also observed for the Majorana edge states of a two-dimensional topological NCSs, Figs. 4.10(d)-(f). Here, we find that the Majorana bands couple most strongly to the x -spin component of the magnetic disorder, Fig. 4.10(d), whereas the y component of the impurity spins does not interact with the edge states, which are fully polarized within the xz spin plane, Fig. 4.10(e) [101–103, 168].

4.2.5. Conclusion

By means of numerical diagonalization, we have here confirmed that there are no marginal or relevant perturbations we can add to the surface Majorana state for weak to moderate nonmagnetic impurities with $\gamma \lesssim \Delta$ (Fig. 4.4(b)). Maximal coupling between boundary and bulk states emerges for $\gamma \gtrsim \Delta$, in particular, peaking at energies close to the bandwidth $\gamma = \gamma_c \sim 5t$, (Fig. 4.4(d)). We find that generally disorder affects the states with energies close to the gap more strongly than those with energies close to zero. This phenomena can be interpreted as an increasingly repulsive potential between particle-hole symmetric impurity states appearing around the Fermi level. In contrast with the topological superconductor studied in the previous section, we find that for all disorder strengths an extended zero-energy state must exist, which indicates that a diffusive thermal metal phase cannot be realized at the surface of a class DIII topological superconductor [119, 148, 160]. At the crossover from weak to strong disorder the surface state wave functions exhibit signs of critical delocalization, particularly around zero energy. For the critical value of disorder

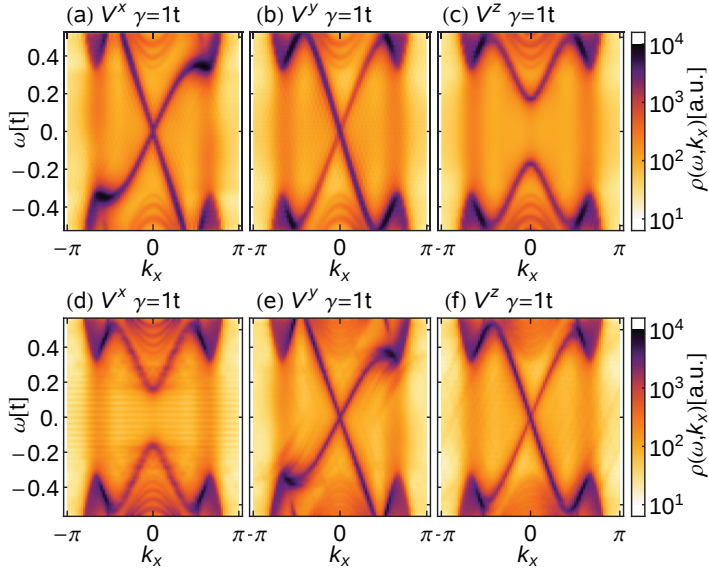


Figure 4.10. (a)-(c) Spectral function $I(\omega, k_x, l)$ on a log scale as a function of surface momentum k_x with $k_y = 0$ for the first three outermost layers at the (001) face of a three-dimensional topological NCS in the presence of magnetic surface disorder with $\gamma = 1t$. In (a), (b), and (c) the impurity spins are polarized along the x , y , and z axes, respectively. (d)-(f) show the same as (a)-(c) but for the (01) edge of a two-dimensional topological NCS on a square lattice of size 80×40 .

strength, the density of states of the two-dimensional topological superconductor diverges at zero energy, which is similar to the Dyson singularity of disordered quasi-one-dimensional superconductors. The (de)localization properties of the wave functions at the crossover from weak to strong disorder, for example the multifractal scaling properties, deserve further investigation. Moreover, it would be interesting to study the (de)localization properties of weak topological superconductors or of three-dimensional topological superconductors with more than one Majorana cone (i.e., winding number $W > 1$).

Very strong disorder with γ much larger than the bandwidth, however, partially localizes the outermost layer while the linearly dispersive Majorana band reappears in the second and third inward layers. That is, for $\gamma \gg \gamma_c$ the effects of disorder on the superconductor and its surface states become weaker, in parallel with what is observed in Bi_2Se_3 (Fig. 4.6).

Finally, we also consider magnetic surface disorder with moderate strength $\gamma = t$, for which the surface states respond according to their intrinsic helical structure. (Fig. 4.10).

We note that magnetic disorder does not result in a more blurred spectral function, rather it distorts the Dirac cone to a preferred direction. In particular, for magnetic impurities polarized along the \hat{z} -direction, we find well defined gapped bands that carry a two dimensional Chern number. An consequently, it could be of interest to study its properties by, for example, puncturing vortices in the bulk superconductor to localize nonabelian Majorana bound states.

Tunneling experiments on disordered surfaces of these systems can be used to confirm our predictions [161].

5. Beyond low energy: Flat-band edge states

In previous chapters, we have discussed extensively the possible exotic surface and edge states in nodal superconductors. We have established the different topological invariants on which they rely on, as well as their basic properties such as spin configuration and localization profiles as they approach nodal structures. Our entire discussion lays on the ability to define these topological invariants which depend explicitly on the surface momenta. A conflict emerges when the surface is disordered. In a disordered system, explicitly breaking translational symmetry, the Hamiltonian is no longer diagonal in momentum space, and \mathbf{k} is not a good quantum number (see introductory discussion in Sec. 1.2). In Chp. 5 we have noticed that under surface disorder alone the momentum-resolved density of states shows clear sharp features in momentum space (cf. Fig. 4.7 and 4.4), leading us to believe that the same should be true for gapless systems. In the latter case, however, low-energy bulk states have a strong presence at the surface, and will be more intensely affected by surface disorder. A second complication we have encountered was when defining the topological invariant itself (cf. Sec. 2.1), since we have used the continuum limit to deform the path into a projection onto the surface Brillouin zone.

Both these questions will be investigated in this chapter by resorting to exact diagonalization and the recursive Green's function technique (cf. App. B).

5.1. Edge states at irregularly shaped boundaries

We consider the model defined in equations (2.1) for a two dimensional system with Rashba spin orbit coupling with point group C_{4v} . To account for higher momentum structures of the superconducting order parameter, we consider the Hamiltonian (2.1), with the form factor

$$f(\mathbf{k}) = \sin k_x \sin k_y, \quad \Delta(\mathbf{k}) = f(\mathbf{k})(i\psi + d \mathbf{g}(\mathbf{k}) \cdot \boldsymbol{\sigma})(i\sigma^2), \quad (5.1)$$

this system was carefully studied in Section 2.6, where we have calculated the momentum dependence of the Berry flux (Fig. 2.6), showing singularities in 8 nodal points of the Brillouin zone. Within the projection of the nodal points (k_0^\pm), we found for dominant triplet pairing,

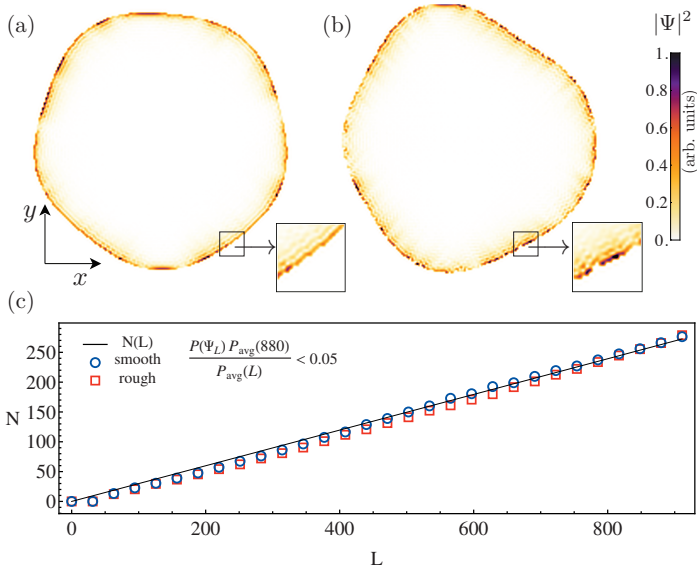


Figure 5.1. Density plot of the edge-state wave function amplitudes $|\Psi_L|^2$ in a $(d_{xy} + p)$ -wave superconducting dot with (a) smooth and (b) rough boundaries. Edge states are present both at an irregular but smooth boundary (a) and at a boundary with short-range disorder (b). Panel (c) shows the average number of edge states for an ensemble of randomly shaped superconducting dots with smooth (blue circles) and rough (red squares) boundaries as a function of circumference L of the dot. Here, the edge states are separated from the bulk states according to criterion (5.5) and by additionally requiring that the energy of the states is smaller than $0.1|\Delta_{\pm}|$ in absolute value. The solid black line represents the analytical approximation given by (5.3).

a singly degenerate flat band edge state as pictured in Fig 2.3(b). This result was bound to the surface projection (01), that is, we had constructed a ribbon geometry where the model (2.1) was discretized over the \hat{y} direction. Considering instead projecting the Brillouin zone onto the (11)-direction, we note the nodal points, carrying negative and positive chirality, project on top of each other in the surface BZ. A rotation interpolating these two surfaces must contract the flat band slowly onto a single point. From this reasoning, we have obtained a general expression for the angular dependence of the zero-bias density of states

$$\frac{dN}{dl} = |k_0^- \sin \varphi - k_0^+ \cos \varphi| - |k_0^- \cos \varphi - k_0^+ \sin \varphi|, \quad (5.2)$$

where $0 \leq \varphi < \pi/4$ is the angle between the local edge orientation and the nearest (01) or (10) direction. Integrating (5.2) along its circumference, we find that the total number of edge states for a circular dot is given by

$$N(L) = \int_0^L \frac{dN}{dl} dl = \frac{8L}{\pi} \left[\frac{k_0^- + k_0^+}{\sqrt{2}} + \frac{k_0^- - k_0^+}{2} - \sqrt{(k_0^-)^2 + (k_0^+)^2} \right]. \quad (5.3)$$

The validity of the previous discussion can be naturally checked numerically by considering irregular shapes, for which the edge direction is not well defined globally and consequently, translational symmetry is broken. An ideal system to study these properties are mesoscopic quantum dots [172]. In this system we can consider two different pictures. First, we consider that the quantum dot has smooth edges, where the edge orientation can be locally determined uniquely. Second we look at the effect of roughness on the same irregularly shaped dots.

We compute the edge-state wave functions of an irregularly shaped ($d_{xy} + p$)-wave superconducting dot with smooth or rough edges, by Fourier transforming the Hamiltonian (2.1) to real space and diagonalize it using standard eigenvalue algorithms [162]. The model parameters used throughout this study are $(t, \mu, \lambda, \psi, d) = (1, 1, 0.5, 0, 0.5)$. The shape of the superconducting dot is defined in terms of a direction-dependent radius [173]

$$R(\theta) = \sum_{i=1}^5 w_i \sin(i\theta - \phi_i), \quad (5.4)$$

with the parameters w_i and ϕ_i , and θ the edge orientation angle. With this definition, the dots can be constructed by cutting shapes of the form (5.4) out of a square, real-space lattice. As depicted in Fig. 5.1(a), this results in superconducting dots with smooth edges, whose orientation is locally well defined for a large enough dot. Bulk- and edge-state wave functions can be distinguished in terms of the participation ratio $P(\Psi_L)$ of a given eigenstate $\Psi_L(\mathbf{r}_i)$ of a dot with circumference L given by Eq. (1.33) in Sec. 1.2. The participation ratio $P(\Psi_L)$ represents the number of lattice sites occupied by the Bogoliubov quasiparticle wave function Ψ_L compared to the total number of sites \mathcal{N} . Hence, for extended bulk states $P(\Psi_L) \simeq 1$, whereas for localized edge states $P(\Psi_L) \ll 1$. We find that for sufficiently large dots, a good characterization of the edge-state wave functions is given by

$$P(\Psi_L) \frac{P_{\text{avg}}(880)}{P_{\text{avg}}(L)} < 0.05, \quad (5.5)$$

where

$$P_{\text{avg}}(L) = \frac{1}{n} \sum_{\iota=1}^n \frac{1}{|\mathcal{W}_\iota|} \sum_{\Psi_L^\iota \in \mathcal{W}_\iota} P(\Psi_L^\iota), \quad (5.6)$$

is the average participation ratio of all the low-energy wave functions Ψ_L^ι of an ensemble of randomly shaped superconducting dots of circumference L . Here, n denotes the size of the statistical ensemble and \mathcal{W}_ι is the set of the first $\sim L/2$ lowest positive energy wave functions calculated numerically for each sample [162]. Since edge disorder leads to a small L -dependent decrease of the participation ratio $P(\Psi_L)$ of all the wave functions Ψ_L , we have included in (5.5) the renormalization factor $P_{\text{avg}}(880)/P_{\text{avg}}(L)$, where $L = 880$ is the circumference of the largest dots.

Smooth edges

We first study irregularly shaped dots with smooth boundaries (Fig. 5.1(a)). These boundaries consist of both (01)-edge and (11)-edge type parts, leading to long-range correlated disorder. As exemplified in Fig. 5.1(a), we find that ingap states appear at almost all boundaries of the dot. That is, the behavior characteristic of the (01)-edge (Fig. 5.1(c)) is generic and qualitatively independent of the edge orientation. Hence, the number of edge states is expected to scale linearly with the circumference L of the superconducting dot. As it turns out, (5.3) is a good approximation for the number of edge states of an irregularly shaped dot. This is revealed in Fig. 5.1(c), which shows the average number of edge states as a function of L for an ensemble of randomly shaped superconducting dots with smooth boundaries (blue circles)¹ together with the analytical result, (5.3). The numerical data and the analytic curve are in good agreement except for dots with small circumferences, with $L < 50$, where finite-size effects become important.

Rough edges

Second, we consider rough boundaries with edge disorder on the lattice scale. In order to introduce short-range edge disorder, we start from the smooth edges, (5.4), and randomly extract edge sites with probability $p_{\text{rm}} = 0.01$, while moving around the edge of the dot once [173]. This “etching” process is repeated twenty times, which leads to an irregular boundary with both long-range and short-range correlated disorder. The edge-state wave function amplitudes for a superconducting dot with rough edges is plotted in Fig. 5.1(b). As

¹Including more disordered layers gives qualitatively similar results, the frozen peaks extend through the disordered layers, while the always existing extension of the edge state in the clean layers is distributed homogeneously.

in the case of smooth edges, we find that edge states appear at almost all boundaries. That is, short-range edge disorder does not change the total number of edge states, but only shifts some of the edge states away from zero energy. This is further evidenced in Fig 5.1(c) (red squares), which shows that the average number of ingap states at a randomly shaped boundary with short-range disorder scales linearly in L , and is in good agreement with (5.3).

5.2. Strong edge disorder

Let us now investigate in detail the effects of both Gaussian and unitary strong edge disorder on the edge of a superconducting nanoribbon. In order to access larger system sizes than in the previous section, we employ here recursive Green's function techniques[174, 175] to calculate the lattice Green's function $G(\omega; r)$ of the disordered system. The local density of states is once again obtained by equation (4.4). In our numerical simulations we consider samples of width $\mathcal{N}_y = 70$ sites and length $\mathcal{N}_x = 600$ sites. Quenched edge disorder is implemented by adding random on-site potentials following (2.12) where we implement explicitly $v(r_j)S^\beta$ in the two outermost layers of the superconducting ribbon. The two limits of Gaussian and unitary disorder are considered (cf. 1.2.4):

- i *Gaussian disorder*: We consider scatterers on the ribbon edge along the \hat{x} -direction, at each lattice site with local potentials $v(x_j)$ drawn from a box distribution $p[v(x_j)] = 1/\gamma_{\text{imp}}$ for $v(x_j) \in [-\gamma_{\text{imp}}/2, +\gamma_{\text{imp}}/2]$. The disorder strength is controlled by the width γ_{imp} of the distribution.
- ii *Unitary disorder*: A dilute density ρ_{imp} of strong scatterers is considered along the ribbon's edge, with constant potential strength $v(x_j) = v_{\text{imp}}$ taken to be much bigger than the gap magnitude $v_{\text{imp}} \gtrsim |\Delta_\pm|$. Both impurity density ρ_{imp} and potential strength v_{imp} can be adjusted to define the total disorder strength.

5.2.1. Nonmagnetic impurities

We start by discussing the effects of nonmagnetic impurities with potentials $v(x_j)S^0$. In Fig. 5.2 is shown the local density of states $\rho_y(\omega)$ for the first four outermost layers of a $(d_{xy} + p)$ -wave superconducting ribbon with nonmagnetic disorder of different strengths. The case of Gaussian type disorder is plotted in panels (a)-(e), whereas the effects of unitary type disorder are presented in panels (f)-(j). In order to estimate the number of ingap edge states in the system, we have fitted a Lorentzian function to the zero-bias peaks in Fig. 5.2. The peak width Γ and the peak area A provide a measure for the number of edge states and their spread in energy, respectively (insets in Fig. 5.2). In agreement with the analytical

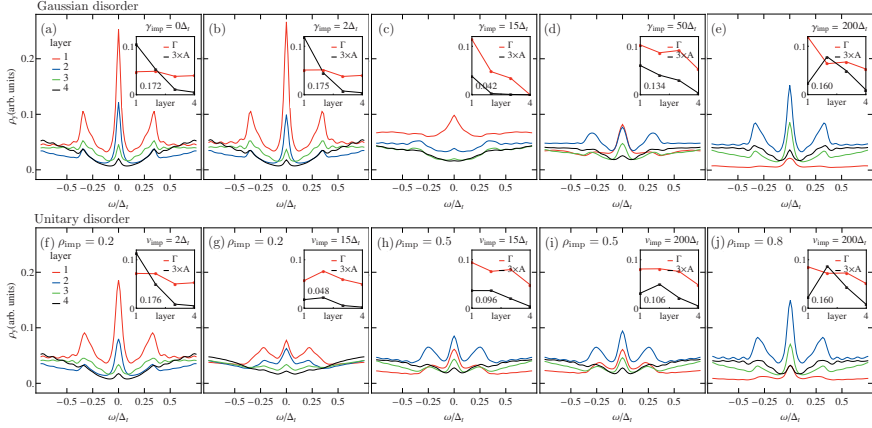


Figure 5.2. Layer-resolved local density of states $\rho_y(\omega)$ plotted for the first four outermost layers of a $(d_{xy} + p)$ -wave superconducting ribbon with (01) edges in the presence of (a)-(e) Gaussian edge disorder and (f)-(j) unitary edge disorder (for details see text). The insets show the width Γ and the area A of the Lorentzian peaks at $\omega = 0$ as a function of layer index y . The number in the lower left corner of the insets indicates the total area of the zero-bias peak as obtained by summing A over the first four layers. In the clean case, $v_{\text{imp}} = 0$, the edge states penetrate only about two layers into the bulk [panel (a)]. For strong disorder the outermost layer shows signatures of localization, while new weakly disordered states appear in the second and third inward layers [panels (e) and (j)].

arguments given in Sec. 2.6, we find that weak and even moderately strong disorder, with γ_{imp} (or $\rho_{\text{imp}}v_{\text{imp}}$) of the same order as the superconducting gaps $|\Delta_{\pm}|$, has very little effect on the edge states: Gaussian disorder gives rise to a slightly faster decay of the edge states into the bulk (Fig. 5.2(b)), whereas unitary disorder somewhat increases the energy spread of the ingap states (Fig. 5.2(f)). The total number of edge states, however, is unaffected by moderately strong disorder as we can conclude by comparing the insets in Figs. 5.2(a), 5.2(b), and 5.2(f).

For strong edge disorder with $\gamma_{\text{imp}} \gg |\Delta_{\pm}|$ (or $\rho_{\text{imp}}v_{\text{imp}} \gg |\Delta_{\pm}|$), on the other hand, the states in the outermost layer become strongly localized. But remarkably, new weakly disordered edge states appear at the second and third inward layers, see Fig. 5.2(e) and 5.2(j). In other words, due to the bulk-boundary correspondence, zero-energy states emerge at the interface between the bulk topological superconductor and the Anderson insulator formed by the outermost layer. This behavior is reminiscent of topological-insulator surface states perturbed by strong disorder [160, 176].

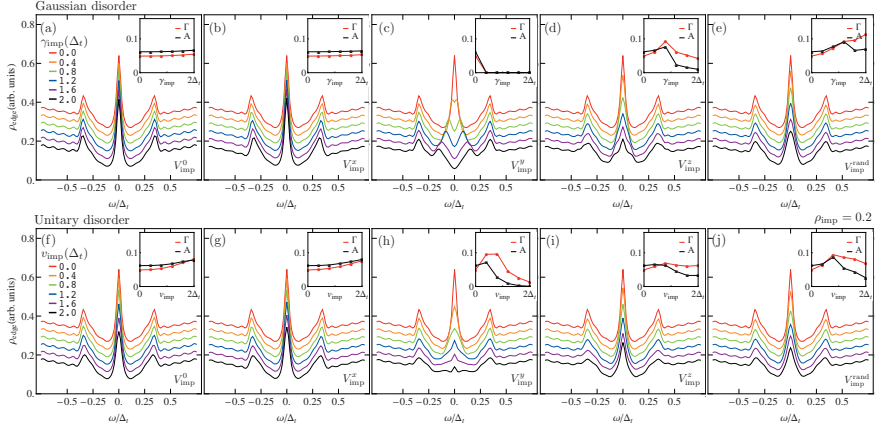


Figure 5.3. Local density of states summed over the four outermost layers, $\rho_{\text{edge}}(\omega) = \frac{1}{4} \sum_{y=1}^4 \rho_y(\omega)$, of a $(d_{xy} + p)$ -wave superconducting ribbon with (01) edges in the presence of nonmagnetic [panels (a) and (f)] and magnetic impurities [panels (b)-(e) and (g)-(j)] in the two outermost layers. Two different disorder distributions are considered: (a)-(e) Gaussian disorder and (f)-(j) unitary disorder with $\rho_{\text{imp}} = 0.2$ (for details see text). Individual traces are vertically offset by 0.02 from one another for clarity. The insets show the width Γ and the area A of the Lorentzian peaks at $\omega = 0$ as a function of disorder strengths γ_{imp} and v_{imp} , respectively.

5.2.2. Magnetic impurities

Magnetic impurities $v(x_j)S^{x,y,z}$ break time-reversal symmetry, thereby lifting the symmetry protection of the edge states. In Fig. 5.3 we present the edge density of states ρ_{edge} , defined as the sum of $\rho_y(\omega)$ over the four outermost layers, of a $(d_{xy} + p)$ -wave superconducting ribbon with (01) edges in the presence of impurity spins polarized along the x , y , and z axes [panels (b)-(d) and (g)-(i)] and randomly oriented magnetic disorder [panels (e) and (j)]. For comparison, Figs. 5.3(a) and 5.3(f) show the edge density of states for nonmagnetic scalar impurities. As before, we consider both Gaussian type disorder (Figs. 5.3(a)-(e)) and unitary type disorder (Figs. 5.3(f)-(j)). Since the flat-band edge states are polarized within the yz spin-plane (cf. Sec. 2.6), impurity spins polarized along the y and z axes couple strongly to the flat bands, whereas scalar impurities and x spin polarized impurities leave the edge states almost unaffected as long as $\gamma_{\text{imp}} (\rho_{\text{imp}} v_{\text{imp}})$ is not much larger than $|\Delta_{\pm}|$. As shown in Figs. 5.3(c) and 5.3(h), y spin polarized impurities are particularly harmful to the flat-band edge states, even for relatively small disorder strengths of $\gamma_{\text{imp}} \simeq 0.8 |\Delta_{\pm}|$ (or $v_{\text{imp}} \simeq 0.8 |\Delta_{\pm}|$ for the unitary type disorder).

Strikingly, random magnetic impurities (Fig. 5.3 (e) and (f)) have a very mild effect on the protection of the surface states, resulting in a broadening of the peak, rather than their total destruction even at high disorder strengths. One can understand this as a more strongly disordered state with an average time-reversal symmetry, since there is no net magnetization on the sample's surface [177].

5.3. Conclusion

In conclusion, our numerical simulations of $(d_{xy} + p)$ -wave superconducting dots with short-range and long-range edge disorder demonstrate that the bulk-edge correspondence remains valid even in the absence of translational symmetry. Ingap states generically appear at the boundary of these superconductors, for almost all edge orientations. Due to their topological origin (cf. Sec. 2.6), the edge states are robust against nonmagnetic scattering from both short-range and long-range correlated edge disorder.

In summary, we have shown that flat-band edge states in noncentrosymmetric superconductors are robust against weak and moderately strong nonmagnetic edge disorder, as long as the disorder strength is not much larger than the superconducting gaps. By means of extensive numerical simulations, we have demonstrated that moderately strong spin-independent disorder spreads the zero-energy edge states over a small band in energy, but does not alter the total number of edge states (Figs. 5.3(a) and 5.3(f)). However, in the presence of strong edge disorder, with strength much larger than the superconducting gaps, the wave functions in the outermost layer localize, but new weakly disordered ingap states appear in the second and third inward layers (Figs. 5.2(e) and 5.2(j)). We have investigated the edge orientation dependence of the edge state density by numerically simulating superconducting dots with both smooth and rough boundaries. Edge states appear for almost all edge orientations, even in the absence of translational symmetry along the boundary, cf. Fig. 5.1. This demonstrates that translational symmetry is not crucial for the protection of the edge states. Time-reversal and particle-hole symmetry, on the other hand, play a key role for the stability of the flat-band states. Consequently, we have found that magnetic impurities, which break time-reversal symmetry, substantially decrease the number of edge states even for small impurity densities, Figs. 5.3(c) and 5.3(h) [178].

6. Effects of correlations on highly degenerate surface states

Noncentrosymmetric superconductors are characterized by a lack of inversion symmetry and strong antisymmetric spin-orbit coupling, possibly bearing topologically nontrivial nodal structures. Consequently, NCSs support surface states that can either have linear dispersion – helical Majorana states; a fully flat dispersion – zero energy flat bands; or linear and flat dispersions in the two orthogonal surface momenta – Majorana arc states (cf. Chp.2). The non-trivial spin structure of these states acts as a protecting shield against local disorder, in this chapter, we ask the question whether this protection extends to local electronic correlations.

It is well established [179] that a system with flat dispersion, and consequently infinite degeneracy, is unstable even to the slightest interaction. Instabilities due to the high density of states emerge to form ordered phases that break down the degeneracy, this is the case, for example, of the ferromagnetic instability in the one-dimension flat band Hubbard model [180, 181].

Another example are the flat-band edge states of two-dimensional high- T_c superconductors. The mechanism of how the degeneracy of these edge states is lifted is under debate. It has been proposed that a new type of pairing symmetry develops as we approach the edge, in particular *is*-wave pairing [182–184]. However, since in high- T_c superconductors pairing is believed to emerge due to repulsive, rather than attractive interactions [7], *s*-wave pairing should be disfavoured. An alternative proposal by Potter and Lee [185] argues that the reason for the zero bias peak splitting is the emergence of a ferromagnetic instability, which is favored in the presence of repulsive interactions. In both cases time-reversal symmetry is explicitly broken, which underlies the topological protection of these edge states. In contrast with NCSs, the flat band edge states of *d*-wave cuprates are doubly degenerate, and superconductivity emerges generally due to attractive interactions, as opposed to repulsive interaction in the case of high- T_c cuprates. In this chapter we argue that this poses a fundamental difference between the two systems, and discuss the mechanism underlying spontaneous breaking of time-reversal symmetry.

In the following sections, we will study the effects of lattice termination on the superconducting order parameter using a self consistent mean-field treatment of an on-site and

nearest-neighbour pairing interaction in the presence of spin-orbit coupling. Such general interaction can be divided into three sectors [186], corresponding to the formation of on-site singlets, nearest-neighbour triplets, and an antisymmetric contribution allowing for scattering of Cooper pairs between the latter channels. The antisymmetric contribution is due to Dzyaloshinskii-Moriya-type interactions [187, 188]. We will see that the existence of infinitely degenerate zero-energy states at the surface results in spontaneous breaking of time-reversal symmetry, thereby removing the topological protection [66]. As a consequence, the flat-bands acquire a finite dispersion leading to spontaneous charge- and spin- currents. This is accompanied by the development of an imaginary contribution in the gap function, however no ferromagnetism is present at the mean-field level for the singly degenerate flat-bands. We contrast this picture with the instability for Majorana arc states, where the degeneracy is doubled, and the Majoranas carry no spin.

6.1. Self-consistent Gap equation

We consider the tight-binding Hamiltonian (2.1) with antisymmetric spin orbit coupling of strength λ ,

$$\mathcal{H} = \sum_{\mathbf{k}} [\varepsilon_{\mathbf{k}} \sigma_{\sigma\tau}^0 - \lambda (\mathbf{g}_{\mathbf{k}} \cdot \boldsymbol{\sigma})_{\sigma\tau}] c_{\mathbf{k},\sigma}^{\dagger} c_{\mathbf{k},\tau}, \quad (6.1)$$

where the vector $\mathbf{g}_{\mathbf{k}}$ is antisymmetric in momentum and σ^{μ} are the Pauli matrices, $\sigma^0 = \mathbb{1}_2$ and $\sigma^i = \{\sigma^1, \sigma^2, \sigma^3\}$, and we assume contraction over spin indices $\{\tau, \sigma, \tau', \sigma'\}$ if repeated. Spin-orbit coupling results in lack of spin conservation, allowing for anomalous interactions between the electrons, such as antisymmetric exchange, or Dzyaloshinskii-Moriya. In its most general form, the pairing interaction is written as

$$\mathcal{H}_{\text{int}} = \sum_{\mathbf{k}, \mathbf{k}'} U_{\sigma\tau\tau'\sigma'}(\mathbf{k}, \mathbf{k}') c_{\mathbf{k}\sigma}^{\dagger} c_{-\mathbf{k}\tau}^{\dagger} c_{-\mathbf{k}'\tau'} c_{\mathbf{k}'\sigma'}, \quad (6.2)$$

which is conveniently separated into three parts [186]:

$$\begin{aligned} U_{\sigma\tau\tau'\sigma'}(\mathbf{k}, \mathbf{k}') &= e_s \tau_{\sigma\tau}^0 \tau_{\tau'\sigma'}^{0\dagger} + e_t [(\mathbf{g}_{\mathbf{k}} \cdot \boldsymbol{\tau})_{\sigma\tau} (\mathbf{g}_{\mathbf{k}'} \cdot \boldsymbol{\tau}^{\dagger})_{\tau'\sigma'}] \\ &\quad + e_m [(\mathbf{g}_{\mathbf{k}} \cdot \boldsymbol{\tau})_{\sigma\tau} \tau_{\tau'\sigma'}^{0\dagger} + \tau_{\sigma\tau}^0 (\mathbf{g}_{\mathbf{k}'} \cdot \boldsymbol{\tau}^{\dagger})_{\tau'\sigma'}], \end{aligned} \quad (6.3)$$

corresponding to an onsite, singlet interaction (e_s), coupling of nearest neighbours through triplet pairing (e_t) and the mixed term (e_m), reflecting the lack of spin conservation. For simplicity we have defined $\tau^i \equiv (i/2)\sigma^2 \sigma^i$. In the mean-field approximation the interacting Hamiltonian is reduced to a superconducting state with an admixture of spin-singlet and

spin-triplet components of magnitudes ψ and d , respectively, and the triplet part inherits the orientation of the spin-orbit vector \mathbf{g}_k [97],

$$\widetilde{\mathcal{H}}_{\text{int}} = \sum_{\mathbf{k}} (i[\psi + d(\mathbf{g}_k \cdot \boldsymbol{\sigma})] \sigma^2)_{\sigma\tau} c_{\mathbf{k},\sigma}^\dagger c_{-\mathbf{k},\tau}^\dagger + \text{h.c.} \quad (6.4)$$

In order to study the spatial dependence of the superconducting gap as we approach the surface, we consider the Fourier transform of the Hamiltonian along k_\perp , perpendicular to the surface. In this basis, the Hamiltonian takes the form

$$\mathcal{H} = \sum_{\mathbf{k}_\parallel, i, j} \Psi_i^\dagger(\mathbf{k}_\parallel) H_{ij}(\mathbf{k}_\parallel) \Psi_j(\mathbf{k}_\parallel), \quad (6.5)$$

where (i, j) label the slab along the r_\perp direction, and the Nambu vectors $\Psi_n(\mathbf{k}_\parallel)$ are given in terms of fermionic creation and annihilation operators as

$$\Psi_i(\mathbf{k}_\parallel) = \{c_{\mathbf{k}_\parallel i\uparrow}, c_{\mathbf{k}_\parallel i\downarrow}, c_{-\mathbf{k}_\parallel i\uparrow}^\dagger, c_{-\mathbf{k}_\parallel i\downarrow}^\dagger\}. \quad (6.6)$$

The interaction after the Fourier transform is given by

$$\begin{aligned} U(\mathbf{k}_\parallel, \mathbf{k}'_\parallel, i, j, n) = \\ \frac{1}{2} [\tau_{\sigma\tau}^0 (e_s \tau^{0\dagger} + e_m \bar{g}_{n-j}^\dagger(\mathbf{k}'_\parallel))_{\tau'\sigma'} + \bar{g}_{i-j}(\mathbf{k}_\parallel)_{\sigma\tau} (e_m \tau^{0\dagger} + e_t \bar{g}_{n-j}^\dagger(\mathbf{k}'_\parallel))_{\tau'\sigma'} \\ + \tau_{\sigma\tau}^0 (e_s \tau^{0\dagger} + e_m \bar{g}_{j-n}^\dagger(\mathbf{k}'_\parallel))_{\tau'\sigma'} + \bar{g}_{j-i}(-\mathbf{k}_\parallel)_{\sigma\tau} (e_m \tau^{0\dagger} + e_t \bar{g}_{j-n}^\dagger(\mathbf{k}'_\parallel))_{\tau'\sigma'}], \quad (6.7) \end{aligned}$$

and the mean-field Hamiltonian reads

$$\widetilde{\mathcal{H}}_{\text{int}} = \Delta_{ij}(\mathbf{k}_\parallel) c_{\mathbf{k}_\parallel i\sigma}^\dagger c_{-\mathbf{k}_\parallel j\tau}^\dagger + \text{h.c.}, \quad (6.8)$$

where the gap takes the form

$$\Delta_{ij}(\mathbf{k}_\parallel) = [\tau^0 \psi_j + \bar{g}_{i-j}(\mathbf{k}_\parallel) d_j] + [\tau^0 \psi_i + \bar{g}_{j-i}(-\mathbf{k}_\parallel) d_i]^\dagger, \quad (6.9)$$

and the surface momentum dependence of the triplet gap is absorbed in the functions

$$\bar{g}_{i-j'}(\mathbf{k}_\parallel) = \frac{1}{4\pi} \int dk_\perp (\mathbf{g}_k \cdot \boldsymbol{\tau}) e^{ik_\perp(i-j)}. \quad (6.10)$$

Finally, the gaps ψ_i and d_i are calculated self consistently by

$$\Delta_i^p = \sum_{\mathbf{k}_\parallel, j} (e_s^p \tau^{0\dagger} + e_t^p \bar{g}_{j-i}^\dagger(\mathbf{k}_\parallel))_{\tau\sigma} \langle c_{-\mathbf{k}_\parallel i\tau} c_{\mathbf{k}_\parallel j\sigma} \rangle, \quad (6.11)$$

for $p = s, t$, where we have introduced the simplified notation $\Delta^s = \psi$, $\Delta^t = d$ with $e_p^p = e_i$ and $e_t^s = e_s^t = e_m$.

6.2. Phase diagram and nodal structure

As a prototype of a topological superconductor with time-reversal symmetry, we consider the noncentrosymmetric superconductor with monoclinic point group symmetry C_2 , for which the spin-orbit coupling vector takes the form

$$\mathbf{g}_k = (\sin k_x + \sin k_y)(\hat{\mathbf{x}} + \hat{\mathbf{y}}) + \sin k_z \hat{\mathbf{z}}. \quad (6.12)$$

This system is expected to support surface states for a wide range of values of ψ and d in the (010) direction. Thus, we take the surface momenta to be along the \hat{x} and \hat{z} axis. We note that the physical phenomena here discussed are only dependent on the existence of topologically non-trivial nodal structures in a bulk superconductor with time-reversal symmetry, and not on the point group used. Other known examples of such systems are $\text{Li}_2\text{Pd}_x\text{Pt}_{3-x}\text{B}$ with cubic point-group (O) and CePt_3Si with tetragonal point group (C_{4v}). Different representations of the point group will add a richer momentum space structure [66]. Our choice of \mathbf{g}_k is the simplest that capture both flat bands (2D degeneracy) and Majorana arc states (1D degeneracy).

For an attractive interaction in the singlet channel $e_s < 0$ or in the triplet channel $e_t < 0$, we expect to find superconducting instabilities. The mixed term e_m will, on the other hand, expand the region of superconducting instabilities, allowing a wider range of e_s and e_t values, including positive ones [186, 189]. A three-dimensional phase diagram can be obtained by solving (6.11) numerically with periodic boundary conditions. Here, for the sake of clarity, we show in Fig. 6.2 (d) a schematic picture of regions where superconductivity can be found.

As expected due to spin-orbit coupling, the solution of the self-consistent gap equation will generally consist of a finite value in both singlet (ψ) and triplet (d) channels. It is known [66] (cf. Sec. 2.3) that for comparable amounts of singlet and triplet pairing, one can achieve through topological Lifshitz transitions both closed or open nodal lines in the Brillouin zone. These nodal lines can be viewed as topological defects in momentum space, which are characterized by topological invariants in the form of a 1-dimensional \mathbb{Z} winding number, defined on a closed loop in momentum space, or, by a two-dimensional \mathbb{Z}_2 index defined on their enclosing spheres [66]. We can see from our numerical calculation below that, most commonly, in the presence of surface flat bands, there is a partner arc state which connects them. Once the nodal rings open or contract to a point, only the arc states remain.

6.3. Surface current

The charge- and spin-current densities are given by the tensor $\mathcal{J}_j^\mu = \text{Re}\{\Psi^\dagger \hat{\mathcal{J}}_j^\mu \Psi\}$, where $\mu = 0$ stands for charge current and $\mu = 1, 2, 3$ refers to the spin-current in the three spatial directions j . The operator $\hat{\mathcal{J}}$ in the real space representation takes the form [190]

$$\hat{\mathcal{J}}_j^\mu = \frac{1}{2} \frac{d}{dt} \{\hat{r}_j, \hat{\sigma}^\mu\}, \quad (6.13)$$

where \hat{r}_j and $\hat{\sigma}^\mu$ are the position and spin operators, respectively. Since the spin-orbit interaction term is not negligible, spin is not conserved and the time-derivative of the spin-operator is non-zero. Using the Heisenberg equation we have $\dot{r}_j = -i[\hat{r}_j, \mathcal{H}]$ and $\dot{\sigma}^\mu = -i[\hat{\sigma}^\mu, \mathcal{H}]$. There are two contributions to the currents, namely one due to the kinetic component of the Hamiltonian, and another one due to spin-orbit coupling. \mathcal{H}^ε and due to the spin-orbit coupling \mathcal{H}^λ . Using $[\hat{r}_j, \hat{\sigma}^i] = 0$ and $[\hat{\sigma}^i, H_j^\varepsilon] = 0$ we have

$$\mathcal{J}_j^\mu(r_1, r_2) = \mathcal{J}_j^{\mu\varepsilon}(r_1, r_2) + \mathcal{J}_j^{\mu\lambda}(r_1, r_2), \quad (6.14)$$

with

$$\begin{aligned} \mathcal{J}_j^{\mu\varepsilon}(r_1, r_2) &= -\text{Im} \Psi_{r_1}^\dagger \frac{1}{2} \{[\hat{r}_j, H_j^\varepsilon], \hat{\sigma}^\mu\} \Psi_{r_2}, \\ \mathcal{J}_j^{\mu\lambda}(r_1, r_2) &= -\text{Im} \Psi_{r_1}^\dagger [\hat{\sigma}^\mu \hat{r}_j, H_j^\lambda] \Psi_{r_2}, \end{aligned} \quad (6.15)$$

where

$$H_j^\varepsilon(r_1, r_2) = \frac{t}{2} (\delta(r_1 - r_2 - 1) + \delta(r_1 - r_2 + 1)) \sigma^0, \quad (6.16)$$

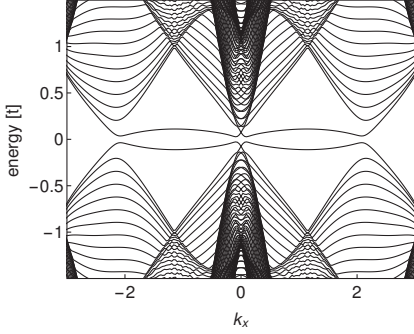
is the kinetic real-space Hamiltonian and

$$H_j^\lambda(r_1, r_2) = \frac{\lambda}{2i} (\delta(r_1 - r_2 - 1) - \delta(r_1 - r_2 + 1)) a^j, \quad (6.17)$$

the real-space spin-orbit coupling with $a^1 = a^2 = (\sigma^1 + \sigma^2)$ and $a^3 = \sigma^3$. Simplifying (6.15) and performing a Fourier transformation along the surface directions we find

$$\begin{aligned} \mathcal{J}_x^{\mu\varepsilon}(\mathbf{k}_\parallel, n) &= t \sin(k_x) \rho_n^\mu(\mathbf{k}_\parallel), \\ \mathcal{J}_z^{\mu\varepsilon}(\mathbf{k}_\parallel, n) &= t \sin(k_z) \rho_n^\mu(\mathbf{k}_\parallel), \\ \mathcal{J}_x^{0\lambda}(\mathbf{k}_\parallel, n) &= -\lambda \cos(k_x) (\rho_n^x(\mathbf{k}_\parallel) + \rho_n^y(\mathbf{k}_\parallel)), \\ \mathcal{J}_z^{0\lambda}(\mathbf{k}_\parallel, n) &= -\lambda \cos(k_z) \rho_n^z(\mathbf{k}_\parallel), \end{aligned} \quad (6.18)$$

(a)



(b)

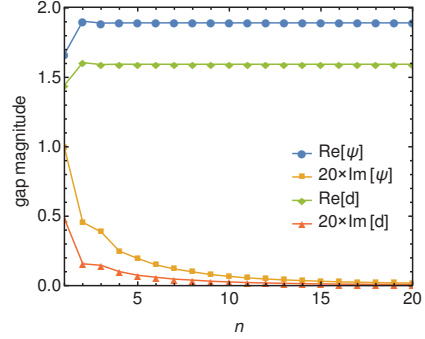


Figure 6.1. (a) Band structure of a NCS superconductor computed self consistently with interaction strengths $(e_s, e_m, e_t) = (-2, -3, -2)$ corresponding to the point D in the parameter space (cf. Fig. 6.2(d)) for the model parameters $(\lambda = 0.5, t = 1, \mu = 2)$. (b) Depth profile of the real and imaginary parts of the gap magnitudes ψ_n and d_n . We note the flat bands gain a dispersion which breaks TRS, together with a gap opening in the nodal points, resulting in a gain of condensation energy. This is in consonance with an imaginary component of the gap function forming at the surface.

and zero for the non-specified components. The local charge- and spin- density of states are defined by

$$\rho_n^\mu(\mathbf{k}_\parallel) = \sum_{\omega} \Psi_n^\dagger(\omega, \mathbf{k}_\parallel) \sigma^\mu \Psi(\omega, \mathbf{k}_\parallel), \quad (6.19)$$

and the total current intensity at the surface is given by

$$I_j^{\mu(\varepsilon, \lambda)} = \sum_{\mathbf{k}_\parallel} \mathcal{J}_x^{\mu(\varepsilon, \lambda)}(\mathbf{k}_\parallel, n = 1). \quad (6.20)$$

The current will therefore be nonzero for density of states antisymmetric in \mathbf{k}_\parallel .

6.4. Numerical results

We see in Fig. 6.1(a-b) that the superconducting gap develops an imaginary contribution as it approaches the surface layers, together with the expected suppression of their total magnitude. This conducts a change in the dispersion of the zero energy flat bands which, depending on their spin orientation, rise or lower in energy. The quasiparticles will accordingly occupy a single one of these flat bands and induce a spontaneous chiral current, that is, with a preferred

direction, breaking simultaneously translational symmetry and time reversal symmetry. We further note that in Fig. 6.1(a) we observe an opening at nodal point. This is consistent with the fact that the eigenstates at the nodal momenta extend along the entire system and are simultaneously present in both surfaces. It follows that under breaking of TRS at the node, a mass term can be formed and consequently a gap can be opened, however, in the infinite size limit, this contribution is expected to vanish, as the ratio between surface and bulk layers rapidly decreases. We refer to Sec. 1.1 to clear any confusion regarding the topological protection of the flat bands when the nodes are opened by a small symmetry breaking gap. In Sec. 6.5 we motivate the gap opening on the flat bands by looking at the surface theory alone.

Fig. 6.2 shows the dependence of the total current intensity on interaction strength for the three different paths in parameter space (a)-(c) with specific values labeled by capital letters A – X:

- (a) Dependence on the singlet pairing interaction e_s for a fixed value of attractive nearest-neighbour e_t and no mixed interaction e_m ;
- (b) Tuning the mixed interaction with a fixed attractive interaction in the singlet and triplet channels;
- (c) Tuning e_t for no mixed interaction and fixed attractive e_s , here we note that for large enough e_t superconductivity is suppressed.

From the form of the spin-orbit coupling (6.12) we can distinguish three main scenarios:

- i $|\psi/d| \gg 1$: Singlet-dominant superconductor, with full gap (s -wave) and topologically trivial (e.g. J).
- ii $|\psi/d| \ll 1$: Triplet-dominant superconductor with nodal points (p -wave) with a non-trivial 2D \mathbb{Z}_2 topological index leading to the emergence of Majorana arc states (e.g. B).
- iii $|\psi/d| \approx 1$: Mixed gap with comparable s - and p -wave components, which results in the appearance of nodal rings or open lines bound to a non-trivial 1D \mathbb{Z} topological winding number, and possibly a 2D \mathbb{Z}_2 index. In this regime, the system bears flat band zero energy states and (or) arc surface states connecting the two symmetric rings (e.g. D).

In Fig. 6.3 we present the momentum dependence of the spin current $\mathcal{J}_x^{x\varepsilon}$, antisymmetrized in the x -direction, part which contributes to the total intensity $I_x^{x\varepsilon}$. This is calculated for a few special points along the paths (a)-(c) marked with capital letters A – J. We start by noting that a finite current exist if and only if the bulk is topologically non-trivial. Topological phase transitions are evident by a change in the topology of the nodal structure, for example a ring

contracting to a point ($X \rightarrow B$), two nodal rings that intersect (E), or simply a gap opening along the rings ($H \rightarrow D$). In these cases, a clear kink can be observed in the current curves, or eventually a full suppression of the total current when the system is driven to a trivial phase. The total current intensity grows with the flat band area, but a sharp peak is found for a pure p -wave superconductor only in the kinetic contribution (see Fig. 6.2(a)-B), for which the charge density of states in the surface is enhanced as a Majorana arc state emerges. Since, in contrast with flat bands, the Majorana arc state is not spin polarized $\rho_1^{\uparrow} = 0$, spin current (Fig. 6.3-B) and the spin-orbit coupling part of the current are fully suppressed. As a final remark, we note the current increases generally with spin-orbit coupling strength λ , however, the change in λ can also result in a different nodal structure, including going through topological Lifshitz phase transitions.

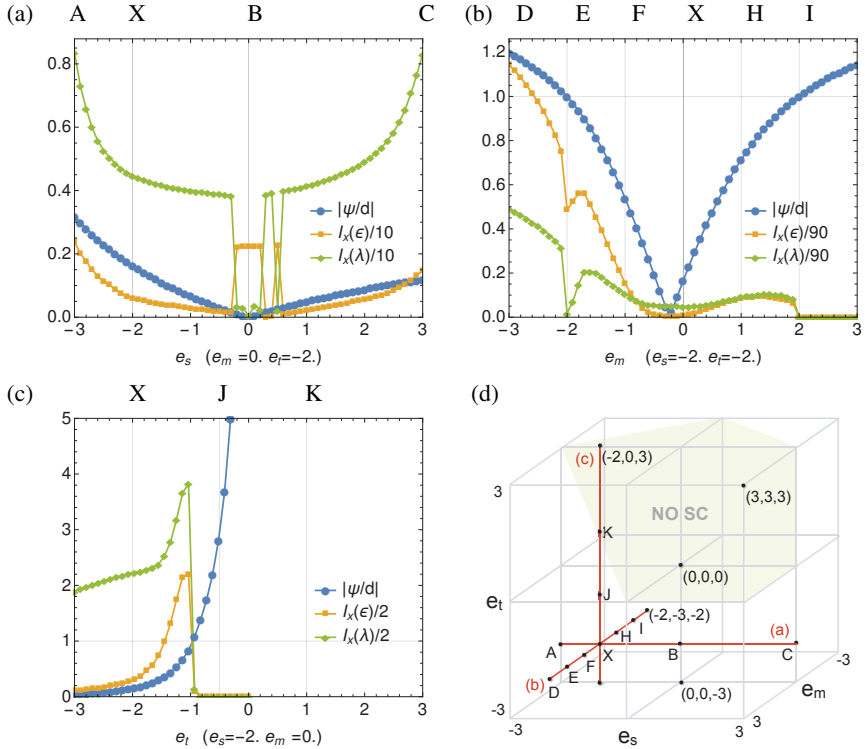


Figure 6.2. (a)-(c) Kinetic and spin-orbit coupling contributions to the charge current, $(I_x^\varepsilon, I_x^\lambda)$ and gap ratio $(|\psi/d|)$ for different strengths of interaction (e_s, e_m, e_t) , corresponding respectively to a on-site-singlet, an antisymmetric Dzyaloshinskii-Moriya and nearest-neighbour-triplet interactions. For all curves we set $t = 1$, $\mu = 2$ and $\lambda = 0.5$. and take systems with size $N_\perp = 50$ and $N_\parallel = 100$. (d) Sketch of the phase diagram in interaction space (e_s, e_m, e_t) . Numerical calculations in shown in (a)-(c) correspond to paths marked in red. Specific interaction values shown in Fig. 6.3 are marked with capital letters along these paths: $A = (-3, 0, -2)$; $B = (0, 0, -2)$; $C = (3, 0, -2)$; $D = (-2, -3, -2)$; $E = (-2, -2, -2)$; $F = (-2, -1, -2)$; $X = (-2, 0, -2)$; $H = (-2, 1, -2)$; $I = (-2, 2, -2)$; $J = (-2, 0, -0.5)$. X is common to the three paths. The region where we don't expect to find a superconducting instability is marked in beige.

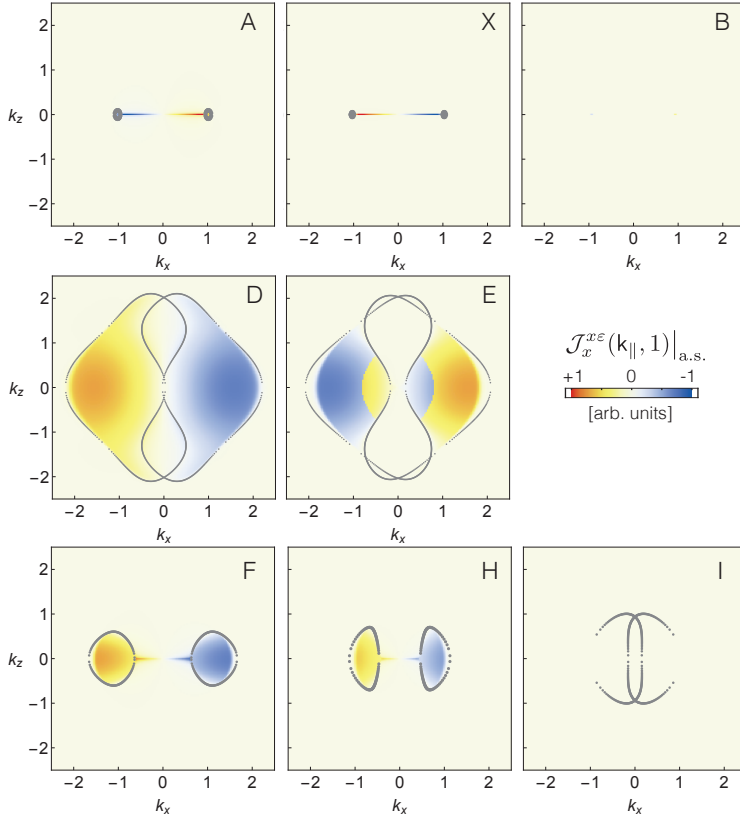


Figure 6.3. Surface momenta (k_{\parallel}) dependence of kinetic spin current $\mathcal{J}_x^{x\varepsilon}$ at the surface layer, delimited by the projection of the nodal structure given the bulk ratio $|\psi/d|$. The result was antisymmetrized to include only the nonvanishing contribution to the current. This, however, results in a symmetry in k_x which is artificial, since only bands with negative energy contribute to the total current. The parameters used for each panel are found in Fig. 6.2. All calculations were performed for $N_{\perp} = 100$ and $N_{\parallel} = 200$.

6.5. Role of Majorana flat bands for TRS breaking

The Majorana character of the surface flat bands sheds a light into why the time-reversal symmetry breaking instability exists to start with. Let us consider that at each momentum k_{\parallel} a single Majorana is present. This is substantiated by the fact that each flat band is singly degenerate and fully chiral. These boundary excitations have half the degrees of freedom of a bulk state, as it is spatially delocalized. They satisfy the local condition $\Psi_n(k) = C^{-1}\Psi_n(k)C$, where n denotes the layer and k the surface momenta. In particular a three dimensional system in the class DIII, as the one introduced above, if it supports Majorana bound states they must satisfy

$$\Psi_{n\sigma}^{\dagger}(k) = (\sigma^1 \otimes \sigma^0)_{\sigma\tau}^* \Psi_{n\tau}(-k), \quad (6.21)$$

where σ, τ are combined spin and charge superindices. Consequently, the Majorana eigenstates have the general form at a single surface ($n = 1$),

$$\Psi^{\dagger}(k) = (u(k), v(k), u^*(-k), v^*(-k))^T, \quad (6.22)$$

for complex functions $u(k)$ and $v(k)$, which we assume to be normalized. If $\Psi^{\dagger}(k)$ is a zero energy bound states, they are eigenstates of the chiral operator S , satisfying $S\Psi^{\dagger}(k) = i\chi\Psi^{\dagger}(k)$ with chirality χ being $\chi = +1$ for $k \in \text{FB1}$ and $\chi = -1$ for $k \in \text{FB2}$. This further restricts $u(k)$ and $v(k)$,

$$\begin{pmatrix} u(k) \\ v(k) \end{pmatrix} = \chi\sigma^2 \begin{pmatrix} u^*(-k) \\ v^*(-k) \end{pmatrix}. \quad (6.23)$$

It is then clear that one can rewrite the basis operators as spinless Majoranas

$$\begin{aligned} \gamma_k &= u(k)c_{k\uparrow} + v(k)c_{k\downarrow} - i\chi v(k)c_{-k\uparrow}^{\dagger} + i\chi u(k)c_{-k\downarrow}^{\dagger} \\ &= u(k)(c_{k\uparrow} + i\chi c_{-k\downarrow}^{\dagger}) + v(k)(c_{k\downarrow} - i\chi c_{-k\uparrow}^{\dagger}), \end{aligned} \quad (6.24)$$

Let us now fix $\chi = +1$ in the surface. We have

$$\gamma_k = u(k)(c_{k\uparrow} + ic_{-k\downarrow}^{\dagger}) + v(k)(c_{k\downarrow} - ic_{-k\uparrow}^{\dagger}), \quad (6.25a)$$

$$\gamma_{-k} = iv^*(k)(c_{-k\uparrow} - ic_{k\downarrow}^{\dagger}) - iu^*(k)(c_{-k\downarrow} + ic_{k\uparrow}^{\dagger}), \quad (6.25b)$$

satisfying $\gamma_k = \gamma_{-k}^{\dagger}$ according to the conventions above. The interaction (6.3) is reduced in the surface to

$$\mathcal{H}^{\text{int}} = -U_{\sigma\tau\tau'\sigma}(k, k')W_{\sigma}(k)V_{\tau}(k)V_{\tau'}^*(k')W_{\sigma'}^*(k')\gamma_k\gamma_{-k}\gamma_{k'}\gamma_{-k'}, \quad (6.26a)$$

with vectors $W(\mathbf{k}) = (u(\mathbf{k}), -v(\mathbf{k}))^T$ and $V(\mathbf{k}) = -i(u(\mathbf{k}), v(\mathbf{k}))^T$. The latter interaction can be decoupled into the different pairing channels

$$\mathcal{H}^{\text{int}} = \sum_i -2e_i f_i(\mathbf{k}, \mathbf{k}') \gamma_{\mathbf{k}} \gamma_{-\mathbf{k}} \gamma_{\mathbf{k}'} \gamma_{-\mathbf{k}'} \quad (6.26b)$$

$$f_s(\mathbf{k}, \mathbf{k}') = u_{\mathbf{k}} u_{\mathbf{k}'}^* v_{\mathbf{k}} v_{\mathbf{k}'}^* \quad (6.26c)$$

$$f_t(\mathbf{k}, \mathbf{k}') = \sin k_x \sin k'_x (u_{\mathbf{k}}^2 - i v_{\mathbf{k}}^2)(u_{\mathbf{k}'}^{*2} + i v_{\mathbf{k}'}^{*2}) \quad (6.26d)$$

$$f_m(\mathbf{k}, \mathbf{k}') = \sin k_x u_{\mathbf{k}'}^* v_{\mathbf{k}'}^* (u_{\mathbf{k}}^2 - i v_{\mathbf{k}}^2) + \sin k'_x u_{\mathbf{k}} v_{\mathbf{k}} (u_{\mathbf{k}'}^{*2} + i v_{\mathbf{k}'}^{*2}) \quad (6.26e)$$

where \mathbf{k} and \mathbf{k}' belong to the same flat band region, and the negative sign in (6.26a) follows from the basis transformation. We note that a ferromagnetic instability cannot emerge from any of these channels due to their spinless character. In fact, the only possible mean-field Hamiltonian one can write is given by

$$\mathcal{H}^{\text{MF}} = \sum_i \Delta_{\mathbf{k}}^i \gamma_{\mathbf{k}} \gamma_{-\mathbf{k}} \quad (6.27)$$

where

$$\Delta_{\mathbf{k}}^i = -2e_i \sum_{\mathbf{k}' \in \text{FB1}} f_i(\mathbf{k}, \mathbf{k}') \langle \gamma_{\mathbf{k}'} \gamma_{-\mathbf{k}'} \rangle. \quad (6.28)$$

which corresponds to an imaginary contribution to the pairing amplitude in the fermionic basis (6.1). Explicitly, we note that TRS ensures $\Delta_{\mathbf{k}}^i = -\Delta_{\mathbf{k}}^{i\dagger}$, and the spontaneous emergence of a non-zero $\Delta_{\mathbf{k}}^i$ necessarily breaks it. This term would, however, cause a total decrease of free energy as condensation energy is gained by opening a gap in the spectrum.

6.6. Role of Majorana arc state for TRS breaking

In a similar approach to the last section, we determine the effective order at the surface of a topological superconducting showing Majorana arc surface states at the mean-field level. In the basis chosen for this calculation, arc surface states are characterized by a linear dispersion along the k_x direction and a flat dispersion along k_z . The explicit form of the two Majorana states at $k_x = 0$ ($E = 0$) was calculated in Sec. 2.5, where we have shown they acquire the simple form (2.23),

$$\gamma_{\mathbf{k}\uparrow} = +i c_{\mathbf{k}\uparrow} + c_{-\mathbf{k}\downarrow}^\dagger, \quad (6.29a)$$

$$\gamma_{\mathbf{k}\downarrow} = -i c_{\mathbf{k}\downarrow} + c_{-\mathbf{k}\uparrow}^\dagger, \quad (6.29b)$$

where we have introduced $k = k_z$, and the operators satisfy $\gamma_{k\sigma} = (i\sigma_2)_{\sigma\tau}\gamma_{-k\tau}^\dagger$. First, we note that for this region in the surface BZ ($k_x = 0$) the interaction tensor is reduced to

$$U(k, k') = e_s \sigma_{\sigma\tau}^2 \sigma_{\tau'\sigma'}^2 + e_t \sin k \sin k' \sigma_{\sigma\tau}^1 \sigma_{\tau'\sigma'}^1 - i e_m (\sin k \sigma_{\sigma\tau}^1 \sigma_{\tau'\sigma'}^2 - \sin k' \sigma_{\sigma\tau}^2 \sigma_{\tau'\sigma'}^1), \quad (6.30)$$

In the Majorana basis we have the reduction

$$c_{k\sigma}^\dagger c_{-k\tau}^\dagger c_{-k'\tau'} c_{k'\sigma'} \rightarrow -W_{\sigma\tau} \gamma_{k\sigma} \gamma_{-k\tau} \gamma_{k'\tau'} \gamma_{-k'\sigma'} \quad (6.31)$$

for $W = \sigma^0 - \sigma^1$. For simplicity, we look at the different interaction channels separately,

$$\mathcal{H}_i^{\text{int}} = -U_i(k, k')_{\sigma\tau\tau'\sigma'} W_{\sigma\tau} \gamma_{k\sigma} \gamma_{-k\tau} \gamma_{k'\tau'} \gamma_{-k'\sigma'} \quad (6.32a)$$

i Singlet channel

$$\mathcal{H}_s^{\text{int}} = e_s \sigma_{\sigma\tau}^2 \sigma_{\tau'\sigma'}^2 \gamma_{k\sigma} \gamma_{-k\tau} \gamma_{k'\tau'} \gamma_{-k'\sigma'}, \quad (6.32b)$$

$$\mathcal{H}_s^{\text{MF}} = \Delta^s (\gamma_{k\uparrow} \gamma_{-k\downarrow} - \gamma_{k\downarrow} \gamma_{-k\uparrow}), \quad \text{with } \Delta^s = e_s \sum_{k'} i \sigma_{\tau'\sigma'}^2 \langle \gamma_{k'\tau'} \gamma_{-k'\sigma'} \rangle, \quad (6.32c)$$

ii Triplet channel

$$\mathcal{H}_t^{\text{int}} = e_t \sin k \sin k' \sigma_{\sigma\tau}^1 \sigma_{\tau'\sigma'}^1 \gamma_{k\sigma} \gamma_{-k\tau} \gamma_{k'\tau'} \gamma_{-k'\sigma'}, \quad (6.32d)$$

$$\mathcal{H}_t^{\text{MF}} = \Delta^t \sin k (\gamma_{k\uparrow} \gamma_{-k\downarrow} + \gamma_{k\downarrow} \gamma_{-k\uparrow}), \quad \text{with } \Delta^t = e_t \sum_{k'} \sin k' \sigma_{\tau'\sigma'}^1 \langle \gamma_{k'\tau'} \gamma_{-k'\sigma'} \rangle, \quad (6.32e)$$

iii Mixed channel

$$\mathcal{H}_m^{\text{MF}} = \frac{e_m}{e_t} \Delta^t (\gamma_{k\uparrow} \gamma_{-k\downarrow} - \gamma_{k\downarrow} \gamma_{-k\uparrow}) + \frac{e_m}{e_s} \Delta^s \sin k (\gamma_{k\uparrow} \gamma_{-k\downarrow} + \gamma_{k\downarrow} \gamma_{-k\uparrow}). \quad (6.32f)$$

We see that, even in the presence of spin-unpolarized doubly degenerate bands, the system has a tendency towards TRS breaking order.

6.7. Conclusion

Due to the infinite number of states at zero energy localized on the surface layers, there is a local instability towards lifting this degeneracy, which can be detected at the mean-field level. The degeneracy lifting is bound to spontaneously break time-reversal symmetry, which protects the topological surface states. TRS is broken by the gap function which acquires an imaginary part (see Fig. 6.1). Both flat band edge states and Majorana arc states become dispersive, leading to spontaneous chiral currents. The surface currents are critically dependent on the nodal structure of the superconducting gap, therefore a change in the interaction strength at any channel, for example by strain, results in a change in the current intensity which can be experimentally detected.

We argue that the mechanism underlying the development of an $i(s + p)$ -wave pairing symmetry on the surface supporting flat bands relies on a repulsive interaction between surface Majorana states, most critically due to their single degeneracy. This is in contrast with high temperature superconductors, where the doubly degenerate flat bands favour edge ferromagnetism.

7. Topology of interacting fermions

In the previous chapter, we have discussed the instability of the surface towards spontaneous symmetry breaking in the presence of electron-electron correlations and infinite surface state degeneracy. These correlations lead to a lifting of the degeneracy, accompanied by the spontaneous breaking of time-reversal symmetry, the global symmetry protecting the DIII bulk topology. Here, we go a step further to ask whether it is possible to remove the surface states via an interaction that does not break any of the global bulk symmetries.

The motivation for such a consideration originates from the pioneering work of Fidkowski and Kitaev [191] where it was shown that for a one-dimensional chains belonging to the class BDI, it is possible to write a fully symmetric interaction involving 8 chains (or one chain with winding number 8) that turns it topologically trivial, i.e., with no boundary modes. From this observation, they conclude that there exists an adiabatic path connecting two distinct topological sectors in the non interacting case, provided part of this path is taken in a region of strong interactions. Here, focusing on fully gapped topological systems with large topological numbers ($W > 1$), we show an extension of these arguments to an arbitrary dimension and symmetry class. Applying a similar reasoning to nodal superconductors is of high priority for future research.

We use a dimensional hierarchy construction to show that Bott periodicity does not hold in the presence of interactions, and derive the resulting topological classification of fermionic systems. In this work we focus uniquely on interacting fermionic phases with short-range entanglement. That is, many interesting interacting topological phases with long-range entanglement are left out, as within strongly correlated systems the classification found in Table 1.1 can be further subdivided as quasiparticles are not constrained to fermionic statistics [192–196]. In this study we choose to focus our attention on fermionic phases in which a parallel to the different entries in Table. 1.1 is still legitimate. We further remark that for interacting fermionic systems, the \mathbb{Z}_2 classification can never be reduced, as these phases are characterized by non-degenerate surface modes. In the following we focus our attention fully on the \mathbb{Z} table entries. Alternative approaches for the derivation of the topological classification of interacting phases in higher dimensions can be found in the literature, under the formalism of cobordism [197], super cohomology [198] and non-linear sigma models [199].

7.1. Dimensional hierarchy in noninteracting fermions

In this section we follow the method presented in Ref. [40] to determine the dimensional hierarchy among non-interacting phases. In this construction, a representative Dirac Hamiltonian is chosen for each entry of the Table 1.1, such that it can be adiabatically deformed into the specific system of study. We have motivated in the introduction that such a choice is always possible. Perhaps the easiest way to understand this simplification is by noting that from the general Dirac Hamiltonian in equation (1.8), we can explicitly write a Hamiltonian for each sector, dimension and symmetry class in Table 1.1. Thus, using the definition of topological sector, we can adiabatically transform any band Hamiltonian in the continuum limit into a Dirac Hamiltonian with the same topological invariant.

7.1.1. Complex classes $\mathbf{A} \leftrightarrow \mathbf{AIII}$

Without any reality condition imposed on the matrix Hamiltonian, $H(\mathbf{k})$ belongs to one of two classes \mathbf{A} or \mathbf{AIII} , determined by whether or not the chiral symmetry S is present. In the absence of chiral symmetry, we can define in even dimensions a Chern number in terms of the Berry curvature. It follows that in class \mathbf{A} , we can write the Dirac representative as an element of the irreducible spinor representation of $SO(2n + 1)$, explicitly given by [40]

$$H_{2n+1}^{2n}(\mathbf{k}) = \sum_{a=1}^{d=2n} k_a \Gamma_{2n+1}^a + m \Gamma_{2n+1}^{2n+1}, \quad (7.1)$$

for $\{\Gamma_{2n+1}^a, \Gamma_{2n+1}^b\} = \delta_{ab}$, as introduced in Sec. 1.1. To construct this Hamiltonian, all the Dirac matrices were exhausted. That is, there is by construction no matrix which anticommutes with the Hamiltonian, leaving no possible symmetry breaking term to be added. For $n = 1$ the above Hamiltonian serves as the representative of the quantum Hall state with the first Chern number (or TKNN number) given by $C_1 = \frac{1}{2}$. As previously encountered in the introduction, this halving of the Chern number is resolved once a lattice regularization is considered. Note, however, that if the above Hamiltonian lives on the surface of a bulk system, such as a topological insulator, this halving is meaningful, and it has been experimentally evidenced by transport measurements [29].

We can reexpress the previous Hamiltonian in a lower dimension via a Kaluza–Klein (KK) dimensional reduction. That is, we can compactify one of the momentum directions (k) into a circle S^1 . This transformation leads to discrete levels of $k = 2\pi N/l$, where l is the radius of S^1 and N is an integer. Taking the limit $l \rightarrow 0$ the gap between the discrete levels diverges, and any state with $N \neq 0$ leaves the relevant energy range. We can then make the

substitution $k = 0$ for the compactified dimension. We get

$$H_{2n+1}^{2n}(\mathbf{k}) = \sum_{a=1}^{2n} k_a \Gamma_{2n+1}^a + m \Gamma_{2n+1}^{2n+1}$$

$$\xrightarrow{\text{KK}(k_1)} H_{2n+1}^{2n-1}(\mathbf{k}) = \sum_{a=2}^{2n} k_a \Gamma_{2n+1}^a + m \Gamma_{2n+1}^{2n+1}, \quad (7.2)$$

where in $H_{2n+1}^d(\mathbf{k})$ the upper and lower-scripts denote dimension d and representation $SO(2n+1)$, respectively. With the absence of Γ_{2n+1}^1 in the reduced Hamiltonian, we get the condition

$$\{H_{2n+1}^{2n-1}(\mathbf{k}), \Gamma_{2n+1}^1\} = 0. \quad (7.3)$$

We have therefore constructed a chiral symmetric Hamiltonian with the chiral operator $S = \Gamma_{2n+1}^1$. Hence, it belongs to the symmetry class AIII, protected by a winding number W . To check that the two-fold Bott periodicity works in this construction, we can compactify a second dimension k_2 . Doing this we get

$$H_{2n+1}^{2n-2}(\mathbf{k}) = \sum_{a=2}^{2n-2} k_a \Gamma_{2n+1}^a + m \Gamma_{2n+1}^{2n+1}. \quad (7.4)$$

The existence of two Dirac matrices that anticommute with the Hamiltonian renders the model above reducible. The combination $R = \Gamma_{2n+1}^1 \Gamma_{2n+1}^2$ commutes with H , since any combination of two Dirac matrices commutes with a third one. Thus, we can block diagonalize the Hamiltonian and look at a single block. We can do this explicitly by using the recursive relations between Dirac matrices¹

$$H_{2n+1}^{2n-2}(\mathbf{k}) = \sum_{a=1}^{2n-1} k_a (\sigma^0 \otimes \Gamma_{2n-1}^a) + m (\sigma^3 \otimes \Gamma_{2n-1}^{2n-1})$$

$$\rightarrow H_{2n-1}^{2n-2}(\mathbf{k}) = \sum_{a=1}^{2n-1} k_a \Gamma_{2n-1}^a + m \Gamma_{2n-1}^{2n-1}, \quad (7.6)$$

¹We can get a general representation of the Dirac matrices by the recursive relation

$$\Gamma_{2n+1}^1 = \sigma^1 \otimes \Gamma_{2n-1}^{2n-1}, \quad \Gamma_{2n+1}^2 = \sigma^2 \otimes \Gamma_{2n-1}^{2n-1}, \quad \Gamma_{2n+1}^{a+2} = \sigma^0 \otimes \Gamma_{2n-1}^a, \quad \Gamma_{2n+1}^{2n+1} = \sigma^3 \otimes \Gamma_{2n-1}^{2n-1}, \quad (7.5)$$

where the dimension of the Dirac matrices Γ_{2n+1}^a is 2^n . In this basis it is easy to see that Γ_{2n+1}^{2a} are all purely imaginary, while Γ_{2n+1}^{2a-1} are purely real.

where in the last step we pick a sign of m . It is interesting to notice that $H_{2n+1}^{2n-2}(\mathbf{k})$ has chiral symmetry, which is broken under reduction. We recover the symmetry class AIII in $d = 2n - 1$, thereby yielding the zig-zag pattern in the first two-rows of Table 1.1.

7.1.2. Real classes DIII \leftrightarrow D \leftrightarrow BDI $\leftrightarrow \dots$

Let us now consider the effect of reality conditions on the above scheme. To do this we will rather apply the TRS and PHS operators to the basis vectors as opposed to the matrix Hamiltonian. We have seen in the introduction that one or both of the following conditions hold,

$$\mathcal{T}\Psi_i\mathcal{T}^{-1} = (U_T)_{ij}\Psi_j, \quad \mathcal{C}\Psi_i\mathcal{C}^{-1} = (U_C)_{ij}\Psi_j^\dagger, \quad (7.7)$$

thereby halving the degrees of freedom of the basis vectors in contrast with the complex case. The resulting basis states are given by Majorana states (classes BDI, D, DIII, CII, C and CI)² or spinless fermions (classes AI and AII). Within these restrictions, we can form four distinct irreducible Dirac Hamiltonians³

$$H_{2n+1}^{2n}(\mathbf{k}) = \sum_{a=2}^{2n+1} k_a \Gamma_{2n+1}^a + m \Gamma_{2n+1}^1, \quad (7.8a)$$

$$H_{2n+1}^{2n-1}(\mathbf{k}) = \sum_{a=3}^{2n+1} k_a \Gamma_{2n+1}^a + m \Gamma_{2n+1}^1, \quad (7.8b)$$

$$H_{2n+1}^{2n-2}(\mathbf{k}) = \sum_{a=4}^{2n+1} k_a \Gamma_{2n+1}^a + im \Gamma_{2n+1}^1 \Gamma_{2n+1}^2 \Gamma_{2n+1}^3, \quad (7.8c)$$

$$H_{2n+1}^{2n-3}(\mathbf{k}) = \sum_{a=5}^{2n+1} k_a \Gamma_{2n+1}^a + im \Gamma_{2n+1}^1 \Gamma_{2n+1}^2 \Gamma_{2n+1}^3, \quad (7.8d)$$

where (7.8b) follows from (7.8a) by a KK compactification, contriving the 8-fold periodic \mathbb{Z} ladder, with alternating chiral symmetry. Similarly, (7.8d) follows from (7.8c) by the KK reduction, forming the $2\mathbb{Z}$ ladder, as a natural double degeneracy emerges from the mass $\mathcal{M} \propto \Gamma_{2n+1}^1 \Gamma_{2n+1}^2 \Gamma_{2n+1}^3$. The antiunitary symmetry operators act on the kinetic and

²Class BDI can also be interpreted as a system with sublattice symmetry of spinless fermions. However, in this work we choose to interpret the states as Majoranas.

³Here we use the notation where the index of the momentum k_a denotes which Γ -matrix it multiplies rather than a specific direction. The spatial dimension should be read off from the total number of independent momenta rather than their exact labels.

mass-like Dirac matrices as follows

$$U_T^\dagger(\Gamma^a)^* U_T = -\Gamma^a, \quad U_T^\dagger(\mathcal{M})^* U_T = +\mathcal{M}, \quad (7.9a)$$

$$U_C^\dagger(\Gamma^a)^* U_C = +\Gamma^a, \quad U_C^\dagger(\mathcal{M})^* U_C = -\mathcal{M}. \quad (7.9b)$$

The sign of the momentum \mathbf{k} is inverted in the process, thus the action is opposite for both terms in the Hamiltonian. \mathcal{M} denotes the appropriate mass matrix, as in either (7.8a) or (7.8c).

As an example (which will be handy for the next section) let us construct explicitly the ladder from DIII in three dimensions to BDI in one dimension,

$$H_5^3(\mathbf{k}) = \sum_{a=2}^4 k_a \Gamma_5^a + m \Gamma_5^1, \quad (\text{DIII} : S = \Gamma_5^5), \quad (7.10a)$$

$$\xrightarrow{\text{KK}} H_5^2(\mathbf{k}) = \sum_{a=3}^4 k_a \Gamma_5^a + m \Gamma_5^1, \quad (\text{DIII} + \text{R} : S = \Gamma_5^5, R = \Gamma_5^5 \Gamma_5^2), \quad (7.10b)$$

$$\xrightarrow{\text{red.}} H_3^2(\mathbf{k}) = \sum_{a=2}^3 k_a \sigma^a + m \sigma^1, \quad (\text{D}), \quad (7.10c)$$

$$\xrightarrow{\text{KK}} H_3^1(k_2) = k_2 \sigma^2 + m \sigma^1, \quad (\text{BDI} : S = \sigma^3). \quad (7.10d)$$

For $n = 2$ we can use the identity $\Gamma^5 = i\Gamma_5^1 \Gamma_5^2 \Gamma_5^3 \Gamma_5^4$, to conclude that the Hamiltonian (7.10a) belongs to the class DIII with $\mathcal{T} = \Gamma_5^1 \Gamma_5^2 \Gamma_5^3 \Gamma_5^4$, from which it follows $\mathcal{T}^2 = -1$ and $\mathcal{C} = \Gamma_5^3 \mathcal{K}$ with $\mathcal{C}^2 = 1$. The combination gives $S = \Gamma_5^5$. The basis states in class DIII will be Majoranas, as they respect $\Psi = \Gamma_5^3 \Psi^\dagger$ with Γ_5^3 real, and spinful, since $\Psi = (\Gamma^5 \Gamma^3) \Psi$, which in a more familiar notation translates to $\Psi = [\sigma^3 \otimes (i\sigma^2)] \Psi$. The Hamiltonian (7.10b) is enriched with a unitary symmetry R and is consequently reducible; (7.10c) does not have TRS but we can define the PHS operator $\mathcal{C} = \sigma^3 \mathcal{K}$, squaring to $+1$. In the last step, we finally recover TRS for the BDI class, now squaring to $+1$, with the symmetry operators given by $\mathcal{T} = \mathcal{K}$ and $\mathcal{C} = \sigma^3 \mathcal{K}$.

As $2\mathbb{Z}$ invariants can be interpreted as \mathbb{Z} invariants with double degeneracy, a similar construction can be made for those ladders. For the present problem this discussion is not relevant and upon interest should be found in the discussion of Ref. [40].

7.2. Breakdown of \mathbb{Z} classification in BDI chains

In their work, Fidkowski and Kitaev [191] have proven the existence of an adiabatic path between two different topological sectors in a one-dimensional Majorana chain without breaking any of the wire's symmetries. For such path to be possible, the system must go through a region of strong interactions involving eight different Majorana fermions. Recalling that we have defined topological sector as an equivalence class of adiabatically connected Hamiltonians, this important result clearly shows that the number of topologically distinct sectors can be changed in the presence of interactions. In particular, the topological invariant for one dimensional systems belonging to class BDI should be taken modulo 8, that is $W^{\text{int}} \approx (W^{\text{free}} \bmod 8)$ resulting in the collapse of the free fermion classification from \mathbb{Z} to \mathbb{Z}_8 .

Even though in their paper Fidkowski and Kitaev have shown the adiabatic path for the entire one-dimensional system, one can understand the same result by looking only at the end points of the chain. If the Majoranas at the ends are gapped out without breaking any bulk symmetries, then the bulk is also trivial [200–202]. This argument is, however, rather subtle and we will assume in the following it generally holds.

Consider 8 Majorana fermions labelled by $\gamma_1, \dots, \gamma_N$, one can understand the number 8 by ruling out the other options. A mass term (coupling two Majoranas) breaks explicitly TRS $\mathcal{H}_{\text{int}}^{\nu=2} = i\gamma_i\gamma_j$, consistent with band topology. Let's consider now four Majoranas, the only 4-point interaction one can write is given by

$$\mathcal{H}_{\text{int}}^{\nu=4} = V\gamma_1\gamma_2\gamma_3\gamma_4. \quad (7.11)$$

Even though this term does not break either TRS or PHS, one can see that its ground state is still degenerate. This can be computed by forming two complex fermions $\psi_1 = \gamma_1 + i\gamma_2$ and $\psi_2 = \gamma_3 + i\gamma_4$. Now (7.11) is given by

$$\mathcal{H}_{\text{int}}^{\nu=4} = -\frac{V}{4} \left(\psi_1\psi_1^\dagger - \frac{1}{2} \right) \left(\psi_2\psi_2^\dagger - \frac{1}{2} \right). \quad (7.12)$$

The ground state of $\mathcal{H}_{\text{int}}^{\nu=4}$ is composed by two states $|11\rangle |00\rangle$ with energies $-V/4$, and is thus not trivial. With an additional two complex fermions (four Majoranas) it is possible to get a singly degenerate ground state by forming singlet state. It follows that the interaction

$$\mathcal{H}_{\text{int}}^{\nu=8} = V\psi_1\psi_2^\dagger\psi_3\psi_4^\dagger + \text{h.c.}, \quad (7.13)$$

has a single ground state given by

$$|\Omega\rangle = \frac{1}{\sqrt{2}}(|0101\rangle - |1010\rangle). \quad (7.14)$$

Consequently, an interface connecting regions defined by $W = +8$ and $W = 0$ hosts no boundary modes, once a local interaction of the form (7.13) is included around the interfacial region, see Fig. 7.1(a-b).

7.3. Dimensional hierarchy for interacting fermions

7.3.1. Example: From BDI to DIII

Let us build on the case of zero dimensional boundary Majoranas in class BDI to derive the classification reduction for a three dimensional system in the symmetry class DIII. To do so, we first go through an intermediate step, in the spirit of Ref. [200], consisting of the construction of two two-dimensional systems in class D with opposite Chern numbers ν and $-\nu$, respectively. The edge theory of the combined system is given by

$$\tilde{\mathcal{H}}_3^1 = \sum_{i=1}^{\nu} \int dx \Psi_i^\dagger (i\sigma^3 \partial_x) \Psi_i, \quad \Psi_i = (\chi_{iL}, \chi_{iR})^T. \quad (7.15)$$

where we have used the Majorana representation, where the charge conjugation operator $\mathcal{C} \equiv C$ is simply the identity, and chiral symmetry $\mathcal{S} \equiv \mathcal{T}$ coincides with the time-reversal operator and is taken to be antiunitary. Without loss of generality, we assume the velocity to be one for all Majorana states, labeled by valley index i and left (L) or right (R) moving. This Hamiltonian belongs to the class DIII+ R which is contained in the less symmetric class D. To see this explicitly, we note that (7.15) is invariant under the symmetries $\mathcal{S} = i\sigma^2 \mathcal{K}$ and $R = -i\sigma^2 \sigma^1$. We now introduce a symmetry breaking term that opens a gap in the edge states, breaking *both* \mathcal{S} and R , but not the combination

$$\mathcal{H}_3^1 = \sum_{i=1}^{\nu} \int dx \Psi_i^\dagger (i\sigma^3 \partial_x + m\sigma^2) \Psi_i. \quad (7.16)$$

Despite that, the Hamiltonian (7.16) respects the chiral symmetry $\tilde{\mathcal{S}} = \mathcal{S}R = \sigma^1 \mathcal{K}$. It is effectively a gapped one dimensional chain belonging to the symmetry class BDI. To find the states at the end of this chain, a zero dimensional edge can be implemented by forcing the mass m to change sign at $x = 0$. For this, we choose

$$m = \tanh x, \quad (7.17)$$

and obtain the zero energy bound state

$$\gamma = (\chi_L + \chi_R) \operatorname{sech} x. \quad (7.18)$$

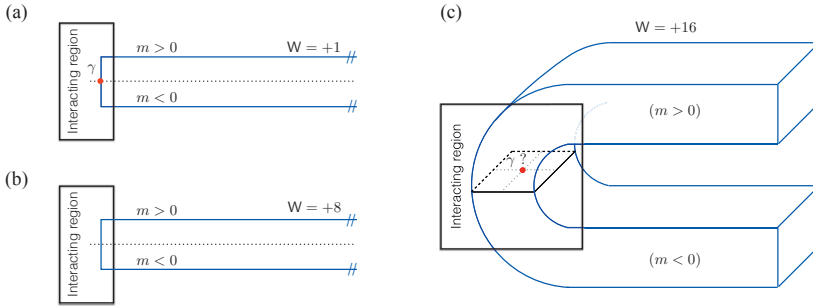


Figure 7.1. Interface between topologically distinct regions, described by a band inversion parametrized by the mass m . At the interface between the two, a region with interactions is considered such that it affects the interface bound states. (a) BDI wire with invariant $W = 1$ holding a Majorana bound state at the mass domain wall, even in the presence of interactions. (b) BDI wire with topological invariant $W = 8$ with no Majorana bound states at the edge due to the local interaction, revealing its topological triviality. (c) Extension of the defect argument to three dimensions in symmetry class DIII with winding number $W = 16$. A mass domain wall defined by $\mathbf{M} = (\tanh x, \tanh y)^T$ is imposed at the interface creating a vortex with 8 localized Majorana bound states. In the presence of the local interaction (7.25) the 8 Majoranas can be gapped out leading to a unique symmetric ground state with no degenerate zero-energy bound states localized at the defect.

Considering a set of ν BDI chains, we find the interchain coupling to be restricted by symmetry. In particular, mass terms of the form $M_{ij}\gamma_i^\dagger\gamma_j$ are forbidden by Hermiticity, $M_{ij} = M_{ji}^*$, and chiral symmetry, $M_{ij} = -M_{ji}^*$, leading to $M = 0$. Quartic terms, on the other hand, are allowed by symmetry.

We have seen in the previous section that given $\nu = 8$ chains, the edge Majoranas can be gapped out. Consequently, the BDI bulk composed of 8 chains is topologically trivial, and so must be the two dimensional DIII + R parent theory hosting it on its edges, for which the defect zero-modes are expected (see discussion on defect bound states in Sec. 1.1.2). We can therefore construct a dimensional reduction mechanism analogous to Eq. (7.10), where instead of compactifying one momentum direction k^a to zero, we create a topological defect which upon breaking the bulk's symmetry, captures the daughter theory. From the topological character of the daughter theory under interactions, one can deduce the topological character of the parent theory under similar interactions. The subtleties of this argument are discussed in the following section.

The second step follows naturally. We construct the two dimensional DIII+ R , surface of a

three dimensional DIII system,

$$\mathcal{H}_5^2 = \sum_{i,j=1}^{\nu} \int d^2 r \eta_i^\dagger [(i\sigma^3 \partial_x + i\sigma^1 \partial_y + m' \sigma^2) \otimes \sigma^3] \eta_i, \quad (7.19)$$

with the symmetries $S = \sigma^0 \otimes \sigma^1 \mathcal{K}$ and $R = -i\sigma^0 \otimes \sigma^2$. $\eta_i = (\chi_{iL}^1, \chi_{iR}^1, \chi_{iL}^2, \chi_{iR}^2)^T$ is the minimal vector composed by the two different chiral sectors (L, R) and the R isospin (1, 2). We note that the mass m' must be introduced with an opposite sign for opposite R isospin, and is thus multiplied by σ^3 . Eq. (7.16) is obtained at the edge of Eq. (7.19) by imposing a domain wall in the mass $m' = \tanh y$. This projection leads to the selection of a single isospin, reducing the vector's size by 2, $\eta \rightarrow \chi$. One can interpret Eq. (7.19) as the surface of a three dimensional DIII Hamiltonian, again, where a gap m' is locally introduced at the surface. In Fig. 7.1(c) this construction is pictured, where we show a mass defect imposed at the interface between two topological distinct regions. At $\mathbf{r} = (0, 0)$ the mass function $\mathcal{M}(\mathbf{r}) = (\tanh x \sigma^2 \otimes \sigma^0 + \tanh y \sigma^2 \otimes \sigma^3)$ forms a zero dimensional defect hosting zero-energy bound states, marked with a red dot. Due to the helical (in contrast with chiral) nature of the DIII class, the surface (7.19) can only be achieved by considering a direct sum of two irreducible Hamiltonians, labeled by the isospin, $\mathcal{H}_5^3 = (\mathcal{H}_5^3)^{(1)} \oplus (\mathcal{H}_5^3)^{(2)}$. A doubling of the number of boundary modes is thus required to achieve 8 Majorana bound states at the zero dimensional defect. This suggests that in order to use symmetry preserving interactions to gap a three dimensional system in the symmetry class DIII with topological invariant ν , we would need at least $\nu = 16$. That is the collapse must be no less than $\mathbb{Z} \rightarrow \mathbb{Z}_{16}$.

7.3.2. General reduction mechanism

In this section, we deduce what is the minimal winding number $W = n$ that allows for such a transformation. Classes with \mathbb{Z} topology lie in three different periodic series, pictured as ladders in Table 1.1,

$$(i) \text{ AIII} \rightarrow \text{A} \rightarrow \dots, \quad (ii) \text{ BDI} \rightarrow \text{D} \rightarrow \text{DIII} \rightarrow \dots, \quad (iii) \text{ CII} \rightarrow \text{C} \rightarrow \text{CI} \rightarrow \dots \quad (7.20)$$

In odd dimensions, each element of these series possesses chiral symmetry \mathcal{S} and bears helical boundary states, it is therefore possible to open a gap on the boundary without explicitly breaking momentum conservation. That is, there is a chance that the topological sectors are unstable under interactions. Conversely, in even dimensions, classes with \mathbb{Z} topology host chiral modes on the boundaries, whose protection does not rely on a symmetry breaking term. In the latter case, the classification is expected to be robust to any interaction

Table 7.1. Topological classification of interacting fermionic phases. Interactions lead to a reduction of the free classification from $\mathbb{Z} \rightarrow \mathbb{Z}_n$, invalidating the two- and eight-fold Bott periodicity. Due to the lack of chiral symmetry S , in even dimensions the \mathbb{Z} phases are robust to interactions.

class	S	$d=1$	$d=2$	$d=3$	$d=4$	$d=5$	$d=6$	$d=7$	$d=8$
A	0	0	\mathbb{Z}	0	\mathbb{Z}	0	\mathbb{Z}	0	$\mathbb{Z} \dots$
AIII	1	$\mathbb{Z} \rightarrow \mathbb{Z}_4$	0	$\mathbb{Z} \rightarrow \mathbb{Z}_8$	0	$\mathbb{Z} \rightarrow \mathbb{Z}_{16}$	0	$\mathbb{Z} \rightarrow \mathbb{Z}_{32}$	0 \dots
AI	0	0	0	0	\mathbb{Z}	0	\mathbb{Z}_2	\mathbb{Z}_2	$\mathbb{Z} \dots$
BDI	1	$\mathbb{Z} \rightarrow \mathbb{Z}_8$	0	0	0	$\mathbb{Z} \rightarrow \mathbb{Z}_{16}$	0	\mathbb{Z}_2	$\mathbb{Z}_2 \dots$
D	0	\mathbb{Z}_2	\mathbb{Z}	0	0	0	\mathbb{Z}	0	$\mathbb{Z}_2 \dots$
DIII	1	\mathbb{Z}_2	\mathbb{Z}_2	$\mathbb{Z} \rightarrow \mathbb{Z}_{16}$	0	0	0	$\mathbb{Z} \rightarrow \mathbb{Z}_{32}$	0 \dots
AII	0	0	\mathbb{Z}_2	\mathbb{Z}_2	\mathbb{Z}	0	0	0	$\mathbb{Z} \dots$
CII	1	$\mathbb{Z} \rightarrow \mathbb{Z}_2$	0	\mathbb{Z}_2	\mathbb{Z}_2	$\mathbb{Z} \rightarrow \mathbb{Z}_{16}$	0	0	0 \dots
C	0	0	\mathbb{Z}	0	\mathbb{Z}_2	\mathbb{Z}_2	\mathbb{Z}	0	0 \dots
CI	1	0	0	$\mathbb{Z} \rightarrow \mathbb{Z}_4$	0	\mathbb{Z}_2	\mathbb{Z}_2	$\mathbb{Z} \rightarrow \mathbb{Z}_{32}$	0 \dots

term added to the action. However, we can impose chiral symmetry on these classes by adding two copies of the corresponding class with counter-propagating boundary modes. This happens at the expense of adding an additional unitary symmetry $[\mathcal{H}, R] = 0$, preventing the coupling between the two chiral sectors. R can be implemented as a mirror symmetry as in the case of topological crystalline insulators [43], as long as $\{S, R\} = 0$.

In the following we argue that the topological classification for the symmetry class s belonging to (i), (ii) or (iii) in d -dimensions can be reduced under interactions from \mathbb{Z} to \mathbb{Z}_n with n given by

$$n = 2^{\lfloor \frac{d-1}{2} \rfloor} n_0, \quad (7.21)$$

with $\lfloor \dots \rfloor$ indicating the floor operator and n_0 the one dimensional reduction for the parent symmetry classes, given by 4, 4 and 2 for (i), (ii) and (iii) in Eq.(7.20), respectively. This result is summarized in Table 7.1 and in Table 7.2 where in the latter we consider R -enriched symmetry classes in even dimensions. In classes BDI, D and DIII, whose surfaces host spinless Majorana states, n needs to be multiplied by a factor of 2 to account for Majorana states being half complex fermions.

Our construction proceeds by reducing a d dimensional system with topological invariant n to a 1D system through a sequence of dimensional reductions. These transformations reduce n by a factor of 2 whenever d is reduced from odd to even, thus, the 1D system inherits

Table 7.2. Topological classification of R -enriched interacting fermionic phases in even dimensions. In the presence of the additional unitary symmetry, chiral symmetry S is recovered by doubling the system. In this case, interactions will lead to a reduction to \mathbb{Z}_n topology.

class	S	$d=2$	$d=4$	$d=6$	$d=8$
A+ R	1	$\mathbb{Z} \rightarrow \mathbb{Z}_4$	$\mathbb{Z} \rightarrow \mathbb{Z}_8$	$\mathbb{Z} \rightarrow \mathbb{Z}_{16}$	$\mathbb{Z} \rightarrow \mathbb{Z}_{32}$...
AIII	1	0	0	0	0 ...
AI+ R	1	0	$\mathbb{Z} \rightarrow \mathbb{Z}_4$	\mathbb{Z}_2	$\mathbb{Z} \rightarrow \mathbb{Z}_{32}$...
BDI	1	0	0	0	\mathbb{Z}_2 ...
D+ R	1	$\mathbb{Z} \rightarrow \mathbb{Z}_8$	0	$\mathbb{Z} \rightarrow \mathbb{Z}_{16}$	\mathbb{Z}_2 ...
DIII	1	\mathbb{Z}_2	0	0	0 ...
AII+ R	1	\mathbb{Z}_2	$\mathbb{Z} \rightarrow \mathbb{Z}_8$	0	$\mathbb{Z} \rightarrow \mathbb{Z}_{16}$...
CII	1	0	\mathbb{Z}_2	0	0 ...
C+ R	1	$\mathbb{Z} \rightarrow \mathbb{Z}_2$	\mathbb{Z}_2	$\mathbb{Z} \rightarrow \mathbb{Z}_{16}$	0 ...
CI	1	0	0	\mathbb{Z}_2	0 ...

the topological invariant $n_0 = 2^{-\lfloor \frac{d-1}{2} \rfloor} n$. Subsequently, we use interaction (7.13) to get a unique symmetry-preserving ground state at the zero dimensional boundary of the one dimensional system and use the resulting phase to adiabatically connect the n_0 topological sector to the trivial one. Analogously, we can show that a d dimensional Hamiltonian in the topological sector $\nu < n$ can never be adiabatically connected to the trivial one. To this end let us write $\nu = 2^r(2k+1)$. For $k > 0$, the dimensional reduction leads to a $d' < d$ dimensional system with an odd number of surface states. An odd number of surface states can never be gapped out. For $k = 0$, the dimensional reduction argument will lead to a zero dimensional defect with $\nu < n_0$ which, as shown in Ref. [191] can never be gapped out. We conclude that $\nu = n$ is the minimum value for which a d dimensional Hamiltonian can be reduced under interactions, without resulting in inconsistencies. Thus, there is a minimum of n topologically distinct sectors, even in the presence of interactions.

Now, we explicitly construct a zero dimensional topological defect at the interface between topologically distinct regions (see Fig 7.1). From Sec. 1.1.2, we know that the bulk topological sector is related to the number of zero-energy bound states at the defect. To carry out the explicit construction of topological defect, we consider the $(d-1)$ dimensional surface hosting $\nu = 2^r$ gapless states. Each gapless state can be described by a 2^{r_0} dimensional Dirac Hamiltonian where $r_0 = \lfloor \frac{d}{2} \rfloor + 1$ for (i) and (ii), and $r_0 = \lfloor \frac{d}{2} \rfloor + 2$ for (iii). That is, the ν topological sector can be expressed under the spinor representation of $SO(2(r+r_0)+1)$ by writing a 2^{r+r_0} dimensional massive Dirac Hamiltonian, given by (1.8), which can be

rewritten as

$$H(\mathbf{r}) = \sum_{a=1}^d i\Gamma^a \partial_a + \mathcal{M}(\mathbf{r}), \quad (7.22)$$

with $a, b = 1, \dots, 2(r + r_0) + 1$. If $r + r_0 \geq d$, we can split the first $2d$ Γ matrices into position and momentum matrices as shown in (1.16),

$$H(\mathbf{r}) = i\mathbf{\Gamma} \cdot \partial_{\mathbf{r}} + \tilde{\mathbf{\Gamma}} \cdot \mathbf{M}, \quad (7.23)$$

where $\mathbf{\Gamma} = (\Gamma^1, \dots, \Gamma^{2d-1})$ are the odd Dirac matrices and $\tilde{\mathbf{\Gamma}} = (\Gamma^2, \dots, \Gamma^{2d})$ the even ones. \mathbf{M} is chosen to represent a topological defect at $\mathbf{x} = 0$. As in the previous section, we set $\mathbf{M} = (\tanh x_1, \dots, \tanh x_d)^T$ (another possible mass function is $\mathbf{M} = \mathbf{x}$ as in [41], this choice affects only the spatial dependence of the zero mode). The zero energy bound states are obtained by

$$\gamma_0^{s_1, \dots, s_d} = \prod_{i=1}^d P_i^{s_i} \operatorname{sech} x_i \Psi, \quad P_i^{\pm} = \frac{1}{2}(1 \pm i\Gamma^{2i-1}\Gamma^{2i}), \quad (7.24)$$

for any constant vector Ψ . The operators P_i^{\pm} are projection operators ($P_i^{\pm 2} = P_i^{\pm} = P_i^{\pm \dagger}$) each reducing the space size by two. Consequently, the topological defect hosts $2^{r - \lfloor \frac{d-1}{2} \rfloor}$ zero energy states. We can conclude that for $2^{r - \lfloor \frac{d-1}{2} \rfloor} = \nu 2^{-\lfloor \frac{d-1}{2} \rfloor} < n_0$, there is no interaction that gaps out the $(d-1)$ dimensional surface, as it would be projected onto a zero dimensional interaction gapping a system with $n < n_0$.

In closing we note that a crucial component of the argument here presented is the enlargement of the representation on which we define the bulk Dirac Hamiltonian. This enlargement guarantees we have enough anticommuting operators to project onto the zero dimensional edge. By construction, the symmetry group is enriched with $\lfloor \frac{d-1}{2} \rfloor$ independent R symmetry operators. This, however, does not pose an impediment, as an enlarged Hamiltonian can always be adiabatically connected to a less symmetric Hamiltonian without changing its topology. The inclusion of an extra unitary symmetry at each two step of two dimensions justifies the doubling in n for higher dimensions and the consequent breakdown of Bott periodicity.

7.3.3. General form of the interaction

In this section, we propose a general form for the d dimensional interaction having a singly degenerate and symmetric ground state. First, we notice that the existence of such an interac-

tion is a direct consequence of the result shown in Tables 7.1 and 7.2, and, from the discussion above, we conclude that such an interaction when projected onto any zero dimensional defect using each of the 2^d projectors (7.24), must result in a trivial zero dimensional system with a unique trivial ground state.

We group $2^{\lfloor \frac{d-1}{2} \rfloor}$ states for the series (i) and (ii), and $2^{\lfloor \frac{d+1}{2} \rfloor - 1}$ for (iii) (cf. Eq. (7.20)) to form a 2^d vector Ψ , acted on by a Dirac Hamiltonian belonging to $SO(2d+1)$, generally given by Eq. (7.22). The minimal interaction can then be constructed with four independent operators Ψ_i ,

$$\mathcal{H}_{\text{int}}^d = V(\Psi_1^\dagger \Gamma^{2d+1} \Psi_2)(\Psi_3^\dagger \Gamma^{2d+1} \Psi_4). \quad (7.25)$$

It can be easily checked that (7.25) reduces to (7.13) if we replace each ψ by its zero dimensional projection γ_0 given by (7.24). Moreover, (7.25) is also manifestly chiral symmetric, since $\mathcal{S}^{-1} \Psi \mathcal{S} = \Gamma^{2d+1} \Psi^\dagger$.

A determination of the d dimensional trivial ground state of the Hamiltonian (7.25) is still lacking. Remarkably, an exact solution was obtained for $d = 1$ using Gross-Neveu models [201], however, at higher dimensions the problem becomes undoubtedly harder. A general proof of adiabaticity between the sectors indicated in this work will be a major focus for future research. Due to the simplicity of the arguments presented in this chapter and the agreement with the current literature [197–199, 201–205], we can hope to find a solution to this problem having a correspondingly simple mathematical structure.

7.4. Conclusion

We have shown that the interface between two distinct topological sectors can fail to host zero-energy boundary modes, provided a region of strong interactions around the interface is considered. In order to write such an interaction, we must consider topological systems with chiral symmetry and a specific number of valleys given by Eq. (7.21), depending on both dimension and symmetry class. We propose a general form for this interaction, which does not break any of the bulk symmetries. From these considerations we can infer the collapse of single particle topology for interacting fermions. This demonstrates the breakdown of Bott periodicity in the presence of interactions, as depicted in Tables 7.1 and 7.2.

8. Conclusion and Outlook

In this work we have studied surface properties of unconventional superconductors of topological origin. We have focused on topological superconductors without inversion center as a playground for multiple topological phenomena. We have derived the different topological boundary states in noncentrosymmetric superconductors in two and three dimensions. Topological invariants that protect these surface states have been determined and low-energy effective surface Hamiltonians have been derived. We have determined the main characteristics of the surface states such as spin polarization and decay profile (cf. Q1 in Sec. 1.4).

Based on these results, we have proposed an experimental signature with universal character which can help in the detection and identification of these unusual states (Q2). We show that dilute disorder affects different types of surface states in drastically different way. On the other hand, disorder can be harmful for topology, mainly if we are concerned with nodal topological phases where no clear energy gap separating bulk and topological states is present. The question of whether topological surface states can withstand disorder is a relevant question which we have addressed in our research (Q3). First, we have discussed it in the context of fully gapped topological superconductors, which are in direct analogy to the well studied topological insulators such as Bi_2Se_3 . Here, in the presence of a pronounced gap in the bulk, the topological states are extremely robust to both weak and moderate disorder. Nevertheless, interesting phenomena emerge when we consider disorder strengths comparable with the bandwidth. Here, impurity bands localized on the surface are maximally coupled with the protected boundary modes, the coupling between the two is not forbidden by symmetry. We evidence numerically that at a critical disorder strength, an Anderson localization transition occurs driving the surface into a localized phase. At this point delocalized boundary modes emerge at inner layers. Behind this process is a transformation on the type of disorder affecting the topological states, a transformation from Gaussian to unitary-like disorder. Our collaborators have measured the predicted burial of the surface states by means of soft X-ray ARPES, equipped with a penetration depth larger than the usual laser-based UV-APRES.

In Chapter 5 we have studied the effect of the two different types of disorder in nodal systems (Q4). We have shown numerically that the number of edge states for irregularly shaped quantum dots is in good agreement with the theoretical prediction, suggesting that the topological edge states exist even in the absence of translation symmetry. Interestingly, we

have shown that even if the surface direction is not locally well defined, but only on average, the results are unchanged. This supports the claim that topological edge states are robust to local perturbations as long as the core symmetries time-reversal and particle-hole are preserved (Q3). We calculate the surface density of states for long superconducting ribbons and show the zero bias conductance peak to be largely unaffected by disorder.

Finally, we focused our attention on possible electronic correlation perturbations to the topological protection of gapless topological systems. We show that correlations play an important role at the surface of superconductors hosting dispersionless topological boundary states. Since their degeneracy is protected by symmetry, we conclude that any type of order emerging at the surface with the role of lifting the degeneracy of the surface flat bands is accompanied by spontaneous breaking of time-reversal symmetry (Q5). We have studied the mechanism of time-reversal symmetry breaking at the surface of noncentrosymmetric superconductors by performing a mean field analysis of a terminated lattice, highlighting the role of the Majorana character of the bound states.

In the last chapter, we have considered the possibility of suppressing topological protection if quartic interactions are present. Building upon the work of Fidkowsky and Kitaev, where the collapse of \mathbb{Z} topology to \mathbb{Z}_8 topology in one-dimensional chains was demonstrated, we derived a dimensional hierarchy mechanism to infer the collapse of topological sectors with any dimension and symmetry (Q6).

In conclusion, we have highlighted that disorder and interactions constitute essential tools to understanding the defining properties of topological boundary states. Beyond the problems discussed in this work, many questions are yet to be addressed. Being far from exhaustive, here I list a few examples. First, in light of the recent observation of Weyl and Dirac semimetals [53, 54], an extension of our results to these systems is desirable. A quantitative study of the localization transition discussed in Chp. 4 deserves to be pursued, however alternative approaches must be considered due to the size limitation of our numerical simulations. Moreover, we have seen in Chp. 6 that spontaneous symmetry breaking plays an important role on the surface of topological materials, as a result of interacting boundary modes. This largely unexplored subject will be a priority for future research. Finally, we have pointed out in Chp. 7 that symmetry protected topological phases can be fundamentally changed in the presence of interactions. Our focus in the near future will be to extend these concepts to nodal systems and to further explore the interacting three dimensional system, relaxing the defect construction. These questions are currently being addressed by many specialists and are bound offer new perspectives on the mathematical structure of topological phases.

A. Point group symmetries

Coupling of spin and orbital degrees of freedom in an antisymmetric way, $\lambda \mathbf{g}_k \cdot \boldsymbol{\sigma}$ with $\mathbf{g}_k = -\mathbf{g}_{-k}$, results in the lift of spin degeneracy of the Fermi surface and leads to complex spin textures of the bands. The Rashba spin-orbit coupling vector $\mathbf{g}(\mathbf{k})$ is constrained by the point group symmetry of the crystal.

Table A.1. Adapted from Ref [96]. Possible $\mathbf{g}(\mathbf{k})$ vectors for all noncentrosymmetric point groups using Schoenflies notation; $k_{\pm} = k_x \pm ik_y$; a 's and b 's are real and complex constants, respectively. Symmetry-imposed $\mathbf{g}(\mathbf{k})$ zeros, and some examples mentioned in the main text.

\mathcal{G}_{pg}	$\mathbf{g}(\mathbf{k})$	nodes	examples
C_1	$(a_1k_x + a_2k_y + a_3k_z)\hat{x} + (a_4k_x + a_5k_y + a_6k_z)\hat{y} + (a_7k_x + a_8k_y + a_9k_z)\hat{z}$	point	
C_2	$(a_1k_x + a_2k_y)\hat{x} + (a_3k_x + a_4k_y)\hat{y} + a_5k_z\hat{z}$	point	BiPd
C_s	$a_1k_z\hat{x} + a_2k_z\hat{y} + (a_3k_x + a_4k_y)\hat{z}$	point	Ir ₂ Ga ₉
D_2	$a_1k_x\hat{x} + a_2k_y\hat{y} + a_3k_z\hat{z}$	point	
C_{2v}	$a_1k_y\hat{x} + a_2k_x\hat{y} + ia_3(k_+^2 - k_-^2)k_z\hat{z}$	line	LaNiC ₂
C_4	$(a_1k_x + a_2k_y)\hat{x} + (-a_2k_x + a_1k_y)\hat{y} + a_3k_z\hat{z}$	point	
S_4	$(a_1k_x + a_2k_y)\hat{x} + (a_2k_x - a_1k_y)\hat{y} + (bk_+^2 + b^*k_-^2)k_z\hat{z}$	line	
D_4	$a_1(k_x\hat{x} + k_y\hat{y}) + a_2k_z\hat{z}$	point	
C_{4v}	$a_1(k_y\hat{x} - k_x\hat{y}) + ia_2(k_+^4 - k_-^4)k_z\hat{z}$	line	CePt ₃ Si, YBCO
D_{2d}	$a_1(k_x\hat{x} - k_y\hat{y}) + a_2(k_+^2 + k_-^2)k_z\hat{z}$	line	
C_3	$(a_1k_x + a_2k_y)\hat{x} + (-a_2k_x + a_1k_y)\hat{y} + a_3k_z\hat{z}$	point	
D_3	$a_1(k_x\hat{x} + k_y\hat{y}) + a_2k_z\hat{z}$	point	
C_{3v}	$a_1(k_y\hat{x} - k_x\hat{y}) + a_2(k_+^3 + k_-^3)\hat{z}$	line	
C_6	$(a_1k_x + a_2k_y)\hat{x} + (-a_2k_x + a_1k_y)\hat{y} + a_3k_z\hat{z}$	point	
C_{3h}	$(b_1k_+^2 + b_1^*k_-^2)k_z\hat{x} + i(b_1k_+^2 - b_1^*k_-^2)k_z\hat{y} + (b_2k_+^3 + b_2^*k_-^3)\hat{z}$	line	
D_6	$a_1(k_x\hat{x} + k_y\hat{y}) + a_2k_z\hat{z}$	point	
C_{6v}	$a_1(k_y\hat{x} - k_x\hat{y}) + ia_2(k_+^6 - k_-^6)k_z\hat{z}$	line	
D_{3h}	$a_1[i(k_+^2 - k_-^2)k_z\hat{x} - (k_+^2 + k_-^2)k_z\hat{y}] + ia_2(k_+^3 - k_-^3)\hat{z}$	line	
T	$a(k_x\hat{x} + k_y\hat{y} + k_z\hat{z})$	point	
O	$a(k_x\hat{x} + k_y\hat{y} + k_z\hat{z})$	point	LiPt ₃ B, ³ He(B)
T_d	$a[k_x(k_y^2 - k_z^2)\hat{x} + k_y(k_z^2 - k_x^2)\hat{y} + k_z(k_x^2 - k_y^2)\hat{z}]$	3 lines	La ₂ C ₃ , Y ₂ C ₃

B. Recursive Green's function

The recursive Green's function method (RGF) [175, 206] has been proven to be an extremely efficient method to calculate transport properties of quasi-one-dimensional systems. In its lattice form, one can calculate both global transport quantities by attaching leads [207], or local quantities, such as local density of states (LDOS) [174]. For the purpose of the numerical calculations shown in Chapters 4 and 5, we use RGF to calculate the LDOS at the edge of a topological superconductor nanoribbon.

We consider a ribbon of length N_x and width N_y such that $N_x \gg N_y$. We can easily diagonalize the Hamiltonian of a single, decoupled column at the site $i\hat{x}$, with numerical effort scaling with N_y^3 . The unperturbed Green's function at the column i is given by $G_{i,i}^0 = H_i^{-1}$. Including the coupling between neighboring columns, $V_{i,j}$, can be seen as a perturbation to the initial decoupled system. This procedure is schematically shown in Fig.B.1 This is achieved by considering a discrete ribbon in real space with width of N_y sites and length of N_x sites. Let us define the block Hamiltonian H^n corresponding to the coupling of two columns spaced by n lattice sites in the x direction,

$$H^n = \frac{1}{(2\pi)^2} \int d^2k H_k e^{ik_y(y-y')} e^{ink_x}, \quad (\text{B.1})$$

where H^0 corresponds to a free column Hamiltonian, while H^1 and H^2 are the coupling to the nearest and next nearest neighbouring columns, respectively. We have considered in our simulations on-site impurities. Thus, for each ribbon's column, i.e., fixed x in $r = (x, y)$, we have

$$H_{\text{imp}}^\beta(x) = \sum_{i=1, N_{\text{imp}}} \Phi_r^\dagger v_{\text{imp}}(r_i) \delta_{r, r_i} S^\beta \Phi_r, \quad (\text{B.2})$$

with impurity positions, r_i , defined according to the disorder distribution, see Sec. 2.3. To accommodate next-nearest neighbor hopping in a convenient way, we can redefine the building blocks of the ribbon to be $8N_y \times 8N_y$ matrices incorporating two columns as the

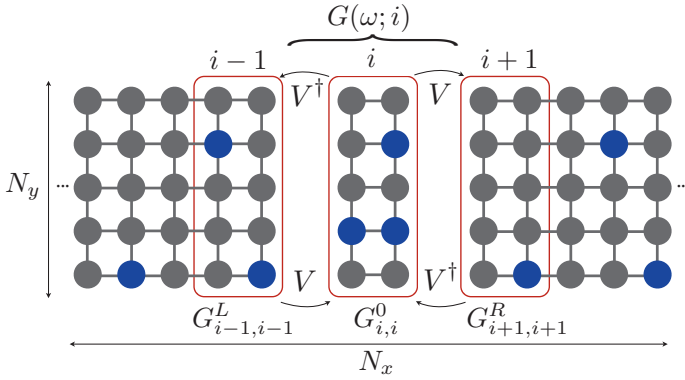


Figure B.1. Scheme of the recursive relation used in Chp. 5 where an effective block of two columns is added at each iteration loop in order to accommodate second neighbour hopping. The local Green's function $G(\omega; i)$ is calculated by attaching the left and right ribbons, $G^{L/R}$, at the site i , according to Eq. B.4. Adapted from Ref. [178].

building blocks, by writing

$$H_i^\beta = \begin{pmatrix} H^0 + H_{\text{imp}}^\beta(2i-1) & H^1 \\ H^{1\dagger} & H^0 + H_{\text{imp}}^\beta(2i) \end{pmatrix},$$

$$V = \begin{pmatrix} H^2 & 0 \\ H^1 & H^2 \end{pmatrix}. \quad (\text{B.3})$$

Here, the block index i runs from 1 to $N_x/2$, i.e., with spacing of 2 lattice sites. Dyson's equation for $G(\omega; i) \equiv G_{i,i}$ takes the form

$$G_{i,i} = G_{i,i}^0 + G_{i,i}^0 V G_{i-1,i}^L + G_{i,i}^0 V^\dagger G_{i,i+1}^R, \quad (\text{B.4})$$

where the ω dependence is suppressed for simplicity, $G_{i,i}^0 = [\omega + i\eta - H_i^\beta]^{-1}$ stands for the uncoupled block at i , while $G_{i,j}^{L/R}$ represent the ribbons to its left and right,

$$G_{i-1,i}^L = G_{i-1,i-1}^L V G_{i,i}, \quad G_{i,i+1}^R = G_{i+1,i+1}^R V^\dagger G_{i,i}. \quad (\text{B.5})$$

The side ribbons are calculated recursively, using the relations

$$G_{n,n}^{L(n)} = \left[\omega + i\eta - H_{n-1}^\beta - V^\dagger G_{n-1,n-1}^{L(n-1)} V \right]^{-1},$$

$$G_{n,n}^{R(n)} = \left[\omega + i\eta - H_{n+1}^\beta - V G_{n+1,n+1}^{R(n+1)} V^\dagger \right]^{-1}, \quad (\text{B.6})$$

at iteration step n , where $n \in \{1, \dots, i-1\}$ and $n \in \{N_x/2, \dots, i+1\}$ for G^L and G^R , respectively. Finally, the local Green's function can be reduced to

$$G_{i,i} = \left[\omega + i\eta - H_i^\beta - \Sigma_i^L - \Sigma_i^R \right]^{-1}, \quad (\text{B.7})$$

with self-energies, $\Sigma_i^{L/R}$, given by

$$\Sigma_i^L = V^\dagger G_{i-1,i-1}^L V, \quad \Sigma_i^R = V G_{i+1,i+1}^R V^\dagger. \quad (\text{B.8})$$

The local density of states can then be easily computed by

$$\rho_y(\omega) = -\frac{1}{4\pi} \frac{1}{N_x} \sum_x \text{Im} \text{tr} G(\omega; x, y), \quad (\text{B.9})$$

where $G(\omega; x, y)$ are obtained from the diagonal entries of $G(\omega; i)$.

Bibliography

- [1] L. D. Landau, Phys. Z. Sowjetunion **11**, 26 (1937).
- [2] V. L. Ginzburg and L. D. Landau, Zhurnal Eksperimental'noi i Teoreticheskoi Fiziki **20**, 1064 (1950).
- [3] H. Onnes, Commun. Phys. Lab. Univ. Leiden **12**, 120 (1911).
- [4] J. Bardeen, L. N. Cooper, and J. R. Schrieffer, Physical Review **108**, 1175 (1957).
- [5] J. G. Bednorz and K. A. Müller, Zeitschrift für Physik B **64**, 189 (1986).
- [6] A. Abanov, A. V. Chubukov, and J. Schmalian, Advances in Physics **52**, 57 (2001).
- [7] D. J. Scalapino, Physics Reports **250**, 329 (1995).
- [8] K. V. Klitzing, G. Dorda, and M. Pepper, Physical Review Letters **45**, 494 (1980).
- [9] M. Z. Hasan and C. L. Kane, Reviews of Modern Physics **82**, 3045 (2010).
- [10] X.-L. L. Qi and S.-C. C. Zhang, Reviews of Modern Physics **83**, 1057 (2011).
- [11] B. I. Halperin, Physical Review B **25**, 2185 (1982).
- [12] C. C. Tsuei and J. R. Kirtley, Physical Review Letters **85**, 182 (2000).
- [13] E. Majorana, Il Nuovo Cimento **14**, 171 (1937).
- [14] J. Alicea, Reports on Progress in Physics **75**, 076501 (2012).
- [15] M. Franz, Physics **3**, 24 (2010).
- [16] E. Bauer and M. Sigrist, *Non-Centrosymmetric Superconductors: Introduction and Overview*, vol. 847 of *Lecture Notes in Physics* (Springer Berlin, 2012).
- [17] S. Yip, Annual Review of Condensed Matter Physics **5**, 15 (2014).
- [18] C.-K. Chiu, J. C. Y. Teo, A. P. Schnyder, and S. Ryu, Arxiv Preprint **1505.03535** (2015).
- [19] D. Hsieh, D. Qian, L. Wray, Y. Xia, Y. S. Hor, R. J. Cava, and M. Z. Hasan, Nature **452**, 970 (2008).
- [20] Y. L. Chen, J. G. Analytis, J.-H. Chu, Z. K. Liu, S.-K. Mo, X. L. Qi, H. J. Zhang, D. H. Lu, X. Dai, Z. Fang, et al., Science **325**, 178 (2009).

- [21] Y. Xia, D. Qian, D. Hsieh, L. Wray, A. Pal, H. Lin, A. Bansil, D. Grauer, Y. S. Hor, R. J. Cava, et al., *Nature Physics* **5**, 18 (2009).
- [22] S. Souma, K. Kosaka, T. Sato, M. Komatsu, A. Takayama, T. Takahashi, M. Kriener, K. Segawa, and Y. Ando, *Physical Review Letters* **106**, 216803 (2011).
- [23] T. Sato, K. Segawa, K. Kosaka, S. Souma, K. Nakayama, K. Eto, T. Minami, Y. Ando, and T. Takahashi, *Nature Physics* **7**, 840 (2011).
- [24] D. Hsieh, Y. Xia, D. Qian, L. A. Wray, J. H. Dil, F. Meier, J. Osterwalder, L. Patthey, J. G. Checkelsky, N. P. Ong, et al., *Nature* **460**, 1101 (2009).
- [25] S.-Y. Xu, Y. Xia, L. A. Wray, S. Jia, F. Meier, J. H. Dil, J. Osterwalder, B. Slomski, A. Bansil, H. Lin, et al., *Science* **332**, 560 (2011).
- [26] S.-Y. Xu, M. Neupane, C. Liu, D. Zhang, A. Richardella, L. Andrew Wray, N. Alidoust, M. Leandersson, T. Balasubramanian, J. Sánchez-Barriga, et al., *Nature Physics* **8**, 616 (2012).
- [27] S. V. Ereameev, G. Landolt, T. V. Menshchikova, B. Slomski, Y. M. Koroteev, Z. S. Aliev, M. B. Babanly, J. Henk, A. Ernst, L. Patthey, et al., *Nature Communications* **3**, 635 (2012).
- [28] L. Fu, *Physical Review Letters* **103**, 266801 (2009).
- [29] M. König, S. Wiedmann, C. Brune, A. Roth, H. Buhmann, L. W. Molenkamp, X. L. Qi, and S.-C. Zhang, *Science* **318**, 766 (2007).
- [30] W. P. Su, J. R. Schrieffer, and A. J. Heeger, *Physical Review Letters* **42**, 1698 (1979).
- [31] M. V. Berry, *Proceedings of the Royal Society A: Mathematical, Physical and Engineering Sciences* **392**, 45 (1984).
- [32] A. Kitaev, in *AIP Conference Proceedings* (AIP, 2009), vol. 1134, p. 22.
- [33] A. P. Schnyder, S. Ryu, A. Furusaki, and A. W. W. Ludwig, in *AIP Conference Proceedings* (AIP, 2009), vol. 1134, p. 10.
- [34] D. J. Thouless, M. Kohmoto, M. P. Nightingale, and M. Den Nijs, *Physical Review Letters* **49**, 405 (1982).
- [35] X. G. Wen, *International Journal of Modern Physics B* **04**, 239 (1990).
- [36] X.-G. Wen, *Advances in Physics* **44**, 405 (1995).
- [37] F. Haake, *Quantum Signatures of Chaos* (Springer, 2010).
- [38] A. P. Schnyder, S. Ryu, and A. W. W. Ludwig, *Physical Review Letters* **102**, 2 (2009).
- [39] A. Altland and M. R. Zirnbauer, *Physical Review B* **55**, 1142 (1996).
- [40] S. Ryu, A. P. Schnyder, A. Furusaki, and A. W. W. Ludwig, *New Journal of Physics* **12**, 65010 (2010).

- [41] J. C. Y. Teo and C. L. Kane, *Physical Review B* **82**, 115120 (2010).
- [42] C.-K. Chiu and A. P. Schnyder, *Phys. Rev. B* **90**, 27 (2014).
- [43] L. Fu, *Physical Review Letters* **106**, 106802 (2011).
- [44] J. Milnor, *Morse Theory* (Princeton University Press, 1963).
- [45] M. Stone, C.-K. Chiu, and A. Roy, *Journal of Physics A: Mathematical and Theoretical* **44**, 045001 (2011).
- [46] M. Ezawa, Y. Tanaka, and N. Nagaosa, *Scientific reports* **3**, 2790 (2013).
- [47] H. Nielsen and M. Ninomiya, *Nuclear Physics B* **193**, 173 (1981).
- [48] A. A. Zyuzin and A. A. Burkov, *Physical Review B* **86**, 115133 (2012).
- [49] P. Hosur, S. A. Parameswaran, and A. Vishwanath, *Physical Review Letters* **108**, 46602 (2012).
- [50] V. Aji, *Physical Review B* **85**, 241101 (2012).
- [51] M. M. Vazifeh and M. Franz, *Physical Review Letters* **111**, 27201 (2013).
- [52] G. B. Halász and L. Balents, *Physical Review B* **85**, 035103 (2012).
- [53] S.-Y. Xu, I. Belopolski, N. Alidoust, M. Neupane, G. Bian, C. Zhang, R. Sankar, G. Chang, Z. Yuan, C.-C. Lee, et al., *Science* **349**, 613 (2015).
- [54] B. Q. Lv, H. M. Weng, B. B. Fu, X. P. Wang, H. Miao, J. Ma, P. Richard, X. C. Huang, L. X. Zhao, G. F. Chen, et al., *Physical Review X* **5**, 031013 (2015).
- [55] K. Wakabayashi, Y. Takane, M. Yamamoto, and M. Sigrist, *New Journal of Physics* **11** (2009).
- [56] G. Volovik, *The Universe in a helium droplet* (Oxford University Press, 2003).
- [57] E. Cartan, *Bulletin de la Societe Mathematique de France* **54**, 214 (1926).
- [58] A. P. Schnyder, S. Ryu, A. Furusaki, and A. W. W. Ludwig, *Physical Review B* **78**, 195125 (2008).
- [59] J. Teo, Ph.D. thesis, University of Pennsylvania (2010).
- [60] M. Nakahara, *Geometry, topology and physics* (CRC Press, 2003).
- [61] M. Atiyah and R. Bott, *Acta Mathematica* **112**, 229 (1964).
- [62] M. Atiyah, R. Bott, and a. Shapiro, *Topology* **3**, 3 (1964).
- [63] F. Wilczek and A. Zee, *Physical Review Letters* **52**, 2111 (1984).
- [64] S. Matsuura, P.-Y. Y. Chang, A. P. Schnyder, and S. Ryu, *New Journal of Physics* **15**, 065001 (2013).

- [65] A. P. Schnyder and S. Ryu, *Physical Review B* **84**, 60504 (2011).
- [66] A. P. Schnyder, P. M. R. Brydon, and C. Timm, *Physical Review B* **85**, 024522 (2012).
- [67] M. Sato and S. Fujimoto, *Physical Review B* **79**, 094504 (2009).
- [68] C. L. Kane and E. Mele, *Physical Review Letters* **95**, 1 (2005).
- [69] M. Sato, *Physical Review B* **79**, 214526 (2009).
- [70] C.-k. Chiu, H. Yao, and S. Ryu, pp. 1–25 (2013).
- [71] B. A. Bernevig and T. L. Hughes, *Topological insulators and topological superconductors* (Princeton University Press, 2013).
- [72] E. Prodan, *Journal of Physics A: Mathematical and Theoretical* **44**, 239601 (2011).
- [73] P. a. Lee and T. V. Ramakrishnan, *Reviews of Modern Physics* **57**, 287 (1985).
- [74] P. W. Anderson, *Physical Review* **109**, 1492 (1958).
- [75] E. Abrahams, P. Anderson, D. Licciardello, and T. Ramakrishnan, *Physical Review Letters* **42**, 673 (1979).
- [76] R. von Helmolt, J. Wecker, B. Holzapfel, L. Schultz, and K. Samwer, *Physical Review Letters* **71**, 2331 (1993).
- [77] F. Evers and A. Mirlin, *Reviews of Modern Physics* **80**, 1355 (2008).
- [78] P. Heinzner, A. Huckleberry, and M. Zirnbauer, *Communications in Mathematical Physics* **257**, 725 (2005).
- [79] F. J. Dyson, *Journal of Mathematical Physics* **3**, 1191 (1962).
- [80] C. W. J. Beenakker, *Reviews of Modern Physics* **69**, 731 (1997).
- [81] F. Wilczek, *Nature Physics* **5**, 614 (2009).
- [82] F. J. Wegner, *Zeitschrift fur Physik B* **25**, 327 (1976).
- [83] A. D. Mirlin and Y. V. Fyodorov, *Physical Review Letters* **72**, 526 (1994).
- [84] F. J. Dyson, *Physical Review* **92**, 1331 (1953).
- [85] W. A. Atkinson, P. J. Hirschfeld, A. H. MacDonald, and K. Ziegler, *Physical Review Letters* **85**, 3926 (2000).
- [86] A. P. Schnyder, Ph.D. thesis, ETH Zurich (2006).
- [87] R. B. Laughlin, *Physical Review B* **23**, 5632 (1981).
- [88] K.-H. Bennemann and J. B. Ketterson, *Superconductivity* (Springer, 2008).

- [89] V. Mourik, K. Zuo, S. M. Frolov, S. R. Plissard, E. P. A. M. Bakkers, and L. P. Kouwenhoven, *Science* **336**, 1003 (2012).
- [90] S. Nadj-berge, I. K. Drozdov, J. Li, H. Chen, S. Jeon, J. Seo, A. H. Macdonald, B. A. Bernevig, and A. Yazdani, *Science* **346**, 6209 (2014).
- [91] A. P. Mackenzie and Y. Maeno, *Reviews of Modern Physics* **75**, 657 (2003).
- [92] Y. Maeno, S. Kittaka, T. Nomura, S. Yonezawa, and K. Ishida, *Journal of the Physical Society of Japan* **81**, 11009 (2012).
- [93] A. Tanaka and S. Takayoshi, *Science and Technology of Advanced Materials* **16**, 014404 (2015).
- [94] E. Bauer, G. Hilscher, H. Michor, C. Paul, E. W. Scheidt, A. Griбанov, Y. Seropegin, H. Noël, M. Sigrist, and P. Rogl, *Physical Review Letters* **92**, 027003 (2004).
- [95] Y. A. Bychkov and E. I. Rashba, *Journal of Physics C: Solid State Physics* **17**, 6039 (2000).
- [96] K. V. Samokhin, *Annals of Physics* **324**, 2385 (2009).
- [97] P. A. Frigeri, D. F. Agterberg, and M. Sigrist, *New Journal of Physics* **6**, 115 (2004).
- [98] A. B. Vorontsov, I. Vekhter, and M. Eschrig, *Physical Review Letters* **101**, 127003 (2008).
- [99] Y. Tanaka, T. Yokoyama, A. V. Balatsky, and N. Nagaosa, *Physical Review B* **79**, 060505 (2009).
- [100] C.-K. Lu and S. Yip, *Physical Review B* **82**, 104501 (2010).
- [101] P. M. R. Brydon, C. Timm, and A. P. Schnyder, *New Journal of Physics* **15**, 45019 (2013).
- [102] A. P. Schnyder, C. Timm, and P. M. R. Brydon, *Physical Review Letters* **111**, 77001 (2013).
- [103] J. S. Hofmann, R. Queiroz, and A. P. Schnyder, *Physical Review B* **88**, 134505 (2013).
- [104] P. Coleman, *ChemInform* **38**, 97 (2007).
- [105] I. Sugitani, Y. Okuda, H. Shishido, T. Yamada, A. Thamizhavel, E. Yamamoto, T. D. Matsuda, Y. Haga, T. Takeuchi, R. Settai, et al., *Journal of the Physical Society of Japan* **75**, 043703 (2006).
- [106] N. Kimura, K. Ito, K. Saitoh, Y. Umeda, H. Aoki, and T. Terashima, *Physical Review Letters* **95**, 247004 (2005).
- [107] A. Giorgi, E. Szklarz, M. Krupka, and N. Krikorian, *Journal of the Less Common Metals* **17**, 121 (1969).

- [108] E. Bauer, R. T. Khan, H. Michor, E. Royanian, A. Grytsiv, N. Melnychenko-Koblyuk, P. Rogl, D. Reith, R. Podloucky, E.-W. Scheidt, et al., *Physical Review B* **80**, 064504 (2009).
- [109] H. Q. Yuan, D. F. Agterberg, N. Hayashi, P. Badica, D. Vandervelde, K. Togano, M. Sigrist, and M. B. Salamon, *Physical Review Letters* **97**, 17006 (2006).
- [110] M. Nishiyama, Y. Inada, and G.-q. Q. Zheng, *Physical Review Letters* **98**, 47002 (2007).
- [111] E. Bauer, G. Rogl, X.-Q. Chen, R. T. Khan, H. Michor, G. Hilscher, E. Royanian, K. Kumagai, D. Z. Li, Y. Y. Li, et al., *Physical Review B* **82**, 064511 (2010).
- [112] A. B. Karki, Y. M. Xiong, I. Vekhter, D. Browne, P. W. Adams, K. R. Thomas, J. Y. Chan, R. Prozorov, H. Kim, D. P. Young, et al., *Physical Review B* **82**, 15 (2010).
- [113] B. Joshi, A. Thamizhavel, and S. Ramakrishnan, *Physical Review B* **84**, 64518 (2011).
- [114] M. Mondal, B. Joshi, S. Kumar, A. Kamlapure, S. C. Ganguli, A. Thamizhavel, S. S. Mandal, S. Ramakrishnan, and P. Raychaudhuri, *Physical Review B* **86**, 094520 (2012).
- [115] Z. Sun, M. Enayat, A. Maldonado, C. Lithgow, E. Yelland, D. C. Peets, A. Yaresko, A. P. Schnyder, and P. Wahl, *Nature Communications* **6**, 6633 (2015).
- [116] F. Yang, A. A. Taskin, S. Sasaki, K. Segawa, Y. Ohno, and K. Matsumoto, pp. 4050–4055 (2015).
- [117] Z. K. Liu, J. Jiang, B. Zhou, Z. J. Wang, Y. Zhang, H. M. Weng, D. Prabhakaran, S.-K. Mo, H. Peng, P. Dudin, et al., *Nature materials* **13**, 677 (2014).
- [118] N. Reyren, S. Thiel, A. D. Caviglia, L. F. Kourkoutis, G. Hammerl, C. Richter, C. W. Schneider, T. Kopp, A.-S. Rüetschi, D. Jaccard, et al., *Science* **317**, 1196 (2007).
- [119] T. Senthil and M. P. A. Fisher, *Physical Review B* **61**, 9690 (2000).
- [120] J. M. Luttinger, *Physical Review* **135**, A1505 (1964).
- [121] K. Nomura, S. Ryu, A. Furusaki, and N. Nagaosa, *Physical Review Letters* **108**, 026802 (2012).
- [122] R. Nakai and K. Nomura, *Physical Review B* **89**, 064503 (2014).
- [123] B. Béri, *Physical Review B* **81**, 1 (2010).
- [124] X.-L. Qi, T. L. Hughes, and S.-C. Zhang, *Physical Review B* **81**, 134508 (2010).
- [125] M. Sato and S. Fujimoto, *Physical Review Letters* **105**, 217001 (2010).
- [126] M. Sato, Y. Tanaka, K. Yada, and T. Yokoyama, *Physical Review B* **83**, 224511 (2011).
- [127] Y. Tanaka, Y. Mizuno, T. Yokoyama, K. Yada, and M. Sato, *Physical Review Letters* **105**, 097002 (2010).

- [128] K. Yada, M. Sato, Y. Tanaka, and T. Yokoyama, *Physical Review B* **83**, 32 (2011).
- [129] Y. Tanaka, M. Sato, and N. Nagaosa, *Journal of the Physical Society of . . .* **81**, 11013 (2011).
- [130] J. P. Dahlhaus, M. Gibertini, and C. W. J. Beenakker, *Physical Review B* **86**, 174520 (2012).
- [131] C.-X. C. Liu, X.-L. Qi, H.-J. H. Zhang, X. Dai, Z. Fang, and S.-C. Zhang, *Physical Review B* **82**, 045122 (2010).
- [132] W.-Y. W.-Y. Shan, H.-Z. H.-Z. Lu, and S.-Q. S.-Q. Shen, *New Journal of Physics* **12**, 43048 (2010).
- [133] G. E. Volovik, *Journal of Experimental and Theoretical Physics Letters* **70**, 609 (1999).
- [134] A. P. Schnyder, P. M. R. Brydon, D. Manske, and C. Timm, *Physical Review B* **82**, 184508 (2010).
- [135] C. Nayak, S. H. Simon, A. Stern, M. Freedman, and S. Das Sarma, *Reviews of Modern Physics* **80**, 1083 (2008).
- [136] A. Stern, *Nature* **464**, 187 (2010).
- [137] Kitaev, Alexei, A. Yu, and A. Y. Kitaev, *Annals of Physics* **303**, 2 (2003).
- [138] D. A. Ivanov, *Physical Review Letters* **86**, 268 (2001).
- [139] J. Linder, T. Yokoyama, A. Sudbø, and M. Eschrig, *Physical Review Letters* **102**, 107008 (2009).
- [140] M. F. Crommie, C. P. Lutz, and D. M. Eigler, *Nature* **363**, 524 (1993).
- [141] L. Capriotti, D. J. Scalapino, and R. D. Sedgewick, *Physical Review B* **68**, 014508 (2003).
- [142] Q.-H. Wang and D.-H. Lee, *Physical Review B* **67**, 020511 (2003).
- [143] H.-M. Guo and M. Franz, *Physical Review B* **81**, 041102 (2010).
- [144] A. Akbari and P. Thalmeier, *EPL (Europhysics Letters)* **102**, 57008 (2013).
- [145] C. Iniotakis, N. Hayashi, Y. Sawa, T. Yokoyama, U. May, Y. Tanaka, and M. Sigrist, *Physical Review B* **76**, 12501 (2007).
- [146] X.-L. Qi, T. L. Hughes, S. Raghu, and S.-C. Zhang, *Physical Review Letters* **102**, 187001 (2009).
- [147] M. E. Peskin and D. V. Schroeder, *An introduction to quantum field theory* (Westview, 1995).
- [148] M. S. Foster, H.-Y. Xie, and Y.-z. Chou, *Physical Review B* **89**, 155140 (2014).

- [149] H.-Y. Xie, Y.-Z. Chou, and M. S. Foster, *Physical Review B* **91**, 024203 (2015).
- [150] A. W. W. Ludwig, M. P. A. Fisher, R. Shankar, and G. Grinstein, *Physical Review B* **50**, 7526 (1994).
- [151] H. H.-J. Zhang, C.-X. C. Liu, X.-L. Qi, X. Dai, Z. Fang, and S.-C. Zhang, *Nature Physics* **5**, 438 (2009).
- [152] Q. Liu and T. Ma, *Physical Review B* **80**, 5 (2010).
- [153] C.-Y. C. C.-Y. Moon, J. Han, H. Lee, and H. J. H. Choi, *Physical Review B* **84**, 195425 (2011).
- [154] B. Sacépé, J. B. Oostinga, J. Li, A. Ubal dini, N. J. G. Couto, E. Giannini, and A. F. Morpurgo, *Nature communications* **2**, 575 (2011).
- [155] M. H. Berntsen, O. Götberg, B. M. B. Wojek, and O. Tjernberg, *Physical Review B* **88**, 195132 (2013).
- [156] M. Bianchi, D. Guan, S. Bao, J. Mi, B. B. Iversen, P. D. C. King, and P. Hofmann, *Nature communications* **1**, 128 (2010).
- [157] M. Bianchi, R. C. Hatch, J. Mi, B. B. Iversen, and P. Hofmann, *Physical Review Letters* **107**, 086802 (2011).
- [158] H. M. Benia, C. Lin, K. Kern, and C. R. Ast, *Physical Review Letters* **107**, 177602 (2011).
- [159] R. C. Hatch, M. Bianchi, D. Guan, S. Bao, J. Mi, B. B. Iversen, L. Nilsson, L. Hornekær, and P. Hofmann, *Physical Review B* **83**, 241303 (2011).
- [160] G. Schubert, H. Fehske, L. Fritz, and M. Vojta, *Physical Review B* **85**, 201105 (2012).
- [161] R. Queiroz and A. P. Schnyder, *Physical Review B* **91**, 1 (2015).
- [162] R. Lehoucq, D. Sorensen, and C. Yang, *ARPACK user guide* (1997).
- [163] K. Nagai, Y. Nagato, M. Yamamoto, and S. Higashitani, *Journal of the Physical Society of Japan* **77**, 111003 (2008).
- [164] S. Murakawa, Y. Tamura, Y. Wada, M. Wasai, M. Saitoh, Y. Aoki, R. Nomura, Y. Okuda, Y. Nagato, M. Yamamoto, et al., *Physical Review Letters* **103**, 155301 (2009).
- [165] S. B. Chung and S.-C. Zhang, *Physical Review Letters* **103**, 235301 (2009).
- [166] G. Schubert, J. Schleede, K. Byczuk, H. Fehske, and D. Vollhardt, *Physical Review B* **81**, 155106 (2010).
- [167] Y.-Z. Chou and M. S. Foster, *Physical Review B* **89**, 165136 (2014).
- [168] P. M. R. Brydon, A. P. Schnyder, and C. Timm, *New Journal of Physics* **17**, 013016 (2015).

- [169] P. W. Brouwer, C. Mudry, B. D. Simons, and A. Altland, *Physical Review Letters* **81**, 862 (1998).
- [170] P. W. Brouwer, A. Furusaki, I. A. Gruzberg, and C. Mudry, *Physical Review Letters* **85**, 1064 (2000).
- [171] S. Ryu, J. E. Moore, and A. W. W. Ludwig, *Physical Review B* **85**, 045104 (2012).
- [172] A. R. Akhmerov, Ph.D. thesis, Leiden University (2011).
- [173] M. Wimmer, A. R. Akhmerov, and F. Guinea, *Physical Review B* **82**, 45409 (2010).
- [174] A. C. Potter and P. A. Lee, *Physical Review B* **83**, 94525 (2011).
- [175] P. Lee and D. S. Fisher, *Physical Review Letters* **47**, 882 (1981).
- [176] Z. Ringel, Y. E. Kraus, and A. Stern, *Physical Review B* **86**, 045102 (2012).
- [177] I. C. Fulga, B. van Heck, J. M. Edge, and a. R. Akhmerov, *Physical Review B* **89**, 155424 (2014).
- [178] R. Queiroz and A. P. Schnyder, *Physical Review B* **89**, 054501 (2014).
- [179] E. Lieb and D. Mattis, *Physical Review* **125**, 164 (1962).
- [180] H. Tasaki, *Journal of Statistical Physics* **84**, 535 (1996).
- [181] H. Tasaki, *Progress of Theoretical Physics* **99**, 489 (1998).
- [182] M. Sigrist, *Progress of Theoretical Physics* **99**, 899 (1998).
- [183] M. Matsumoto and H. Shiba, *Journal of the Physical Society of Japan* **64**, 3384 (1995).
- [184] P. Fulde, *Physical Review* **137**, A783 (1965).
- [185] A. C. Potter and P. a. Lee, *Physical Review Letters* **112**, 1 (2014).
- [186] P. A. Frigeri, D. F. Agterberg, I. Milat, and M. Sigrist, *The European Physical Journal B* **54**, 435 (2006).
- [187] I. Dzyaloshinsky, *Journal of Physics and Chemistry of Solids* **4**, 241 (1958).
- [188] T. Moriya, *Physical Review* **120**, 91 (1960).
- [189] L. Klam, Ph.D. thesis, Max-Planck-Institut für Festkörperforschung (2010).
- [190] J. Shi, P. Zhang, D. Xiao, and Q. Niu, *Physical Review Letters* **96**, 1 (2006).
- [191] L. Fidkowski and A. Kitaev, *Physical Review B* **81**, 134509 (2010).
- [192] F. Pollmann, A. M. Turner, E. Berg, and M. Oshikawa, *Physical Review B* **81**, 064439 (2010).
- [193] A. M. Turner, F. Pollmann, and E. Berg, *Physical Review B* **83**, 075102 (2011).

- [194] L. Fidkowski and A. Kitaev, *Physical Review B* **83**, 075103 (2011).
- [195] X. Chen, Z.-C. Gu, Z.-X. Liu, and X.-G. Wen, *Science* **338**, 1604 (2012).
- [196] E. Tang and X.-G. Wen, *Physical Review Letters* **109**, 1 (2012).
- [197] A. Kapustin, R. Thorngren, A. Turzillo, and Z. Wang, *Arxiv Preprint* **1406.7329** (2014).
- [198] Z.-C. Gu and X.-G. Wen, *Physical Review B* **90**, 115141 (2014).
- [199] T. Morimoto, A. Furusaki, and C. Mudry, *Physical Review B* **92**, 125104 (2015).
- [200] X. L. Qi, *New Journal of Physics* **15** (2013).
- [201] H. Yao and S. Ryu, *Physical Review B* **88**, 064507 (2013).
- [202] M. A. Metlitski, L. Fidkowski, X. Chen, and A. Vishwanath, *Arxiv Preprint* **1406.3032** (2014).
- [203] L. Fidkowski, X. Chen, and A. Vishwanath, *Physical Review X* **3**, 041016 (2013).
- [204] T. Senthil, *Annual Review of Condensed Matter Physics* **6**, 299 (2015).
- [205] C. Wang and T. Senthil, *Physical Review B* **89**, 195124 (2014).
- [206] D. J. Thouless and S. Kirkpatrick, *Journal of Physics C: Solid State Physics* **14**, 235 (2000).
- [207] T. Ando, *Physical Review B* **44**, 8017 (1991).

Zusammenfassung

In dieser Arbeit untersuchen wir die Oberflächeneigenschaften von topologischen Materialien. Insbesondere untersuchen wir die Eigenschaften von topologischen Supraleitern ohne Inversionszentrum. Diese Materialien besitzen eine Vielzahl von topologischen Eigenschaften, zum Beispiel Oberflächenzustände mit einer linearen und (oder) flachen Dispersion, die auf Grund einer topologischen Knotenstruktur des supraleitenden Ordnungsparameters entstehen.

Ein bemerkenswertes Merkmal von topologischen Phasen ist ihre Robustheit gegen lokale Störungen. In gewöhnlichen topologischen Phasen, wie zum Beispiel den topologischen Bandisolatoren, entsteht diese Robustheit durch eine nicht-triviale Phasenstruktur der Wellenfunktionen im Volumeninneren, sowie durch eine Bandlücke, die die Valenzbänder von den Leitungsbändern trennt. In der vorliegenden Arbeit untersuchen wir zu welchem Grade diese Robustheit auf lückenlose topologische Phasen übertragen werden kann. Wir benutzen numerische Methoden, um die Robustheit der Oberflächenzustände gegen lokale Verunreinigungen zu testen, und untersuchen den unterschiedlichen Einfluss von verschieden starken und verschieden gearteten Störstellen.

Wir bestimmen die experimentellen Signaturen der exotischen Oberflächenzustände in der Fourier-transformierten Zustandsdichte, unter der Annahme einer niedrigen Dichte von Störstellen. Die Fourier-transformierte Zustandsdichte kann mittels der Rastertunnelmikroskopie gemessen werden. Wir zeigen, dass verschiedene Arten von Oberflächenzuständen verschiedene Streuinterferenzmuster erzeugen. Daher ist die Rastertunnelmikroskopie besonders gut dazu geeignet, zwischen den Oberflächenzuständen zu unterscheiden.

Außerdem untersuchen wir die Effekte von starker Oberflächenunordnung, welche die topologischen Eigenschaften im Volumeninneren nur unwesentlich verändert. Wir zeigen, dass zwei Arten von Unordnungen besonders interessant sind. Zunächst betrachten wir starke Schwankungen im elektrostatischen Potential der Oberfläche, was zu einer hohen Dichte von schwachen Oberflächenstreuern führt. Wir zeigen, dass diese Störstellen zu Streuung zwischen den Oberflächenzuständen führen, da ihre Energie nahe bei der Energie der Oberflächenzustände liegt. Folglich ist diese Art von Störstellen besonders schädlich für die topologischen Oberflächenzustände, insbesondere wenn die Stärke der Schwankungen im elektrostatischen Potential von der Größenordnung der Bandbreite ist.

Die zweite Art von Unordnung, die wir untersuchen, besteht aus einer niedrigen Dichte

von starken Streuzentren, die zum Beispiel durch Gitterleerstellen oder Oberflächenrauheit erzeugt werden. Wir zeigen, dass sich in der Anwesenheit dieser Art von Unordnung die Oberflächenzustände ein Stück weit ins Volumeninnere zurückziehen. Daher können Gitterleerstellen oder Oberflächenunebenheiten die topologischen Randzustände von Materialien mit oder ohne Bandlücke nicht zerstören. Daraus folgt, dass die Existenz der topologischen Oberflächenzuständen nicht von der Translationssymmetrie abhängt. Wir zeigen, dass sich die Halbwertsbreite der Spektralfunktion der Oberflächenquasiteilchen verkleinert, wenn die erste Art von Unordnung durch die zweite ersetzt wird. Dies führt zu einem schärferen Signal in der Photoemissionsmessung von Bismutselenid, wenn an der Oberfläche Leerstellen durch Sputtern erzeugt werden.

Darüber hinaus untersuchen wir das Zusammenspiel zwischen Topologie und Elektron-Elektron-Wechselwirkung an der Oberfläche von Supraleitern mit Knoten in der der Energielücke. Dies ist wichtig, da die dispersionslosen Oberflächenbänder dieser Supraleiter eine unendliche Grundzustandsentartung haben, die zu einer spontanen Symmetriebrechung führen kann. Wir zeigen, dass für flache Bänder ohne Spinentartung die Zeitumkehrinvarianz durch eine komplexe, supraleitende Paarungsamplitude spontan gebrochen wird. Dies führt zur Erzeugung spontaner chiraler Ladungsströme an der Oberfläche des topologischen Supraleiters.

Als letztes studieren wir Wechselwirkungen, welche die Oberflächenzustände zerstören ohne die Symmetrie zu brechen. Es wurde vor kurzem gezeigt, dass die nichttriviale Topologie eines eindimensionalen topologischen Supraleiters mit einer Invarianten, die ein Vielfaches von acht ist, durch Wechselwirkungen zerstört werden kann. Mit Hilfe einer Dimensionsreduktion leiten wir die allgemeine Form der quadratischen Wechselwirkungen her, die die topologischen Sektoren der nicht-wechselwirkenden Hamiltonoperatoren durch eine adiabatische Transformation miteinander verbindet.

Resumo

Neste trabalho, consideramos propriedades de superfícies em sistemas topológicos, com especial atenção dada a supercondutores topológicos sem simetria sob inversão espacial. Devido a estruturas nodais complexas do parâmetro de ordem de supercondutividade, estes materiais são protótipos para sistemas ricos em fenómenos topológicos, tanto com estados de superfície com dispersão linear, como dispersão constante.

Uma das principais características em fases topológicas é a robustez perante perturbações locais. Em fases topológicas comuns, como isoladores topológicos de bandas, esta robustez vem da existência de um pronunciado hiato energético que separa os vários sectores topológicos. Averiguamos a possibilidade de estender esta análise a fases topológicas sem hiato energético e com regiões nodais. Nomeadamente, apresentamos um estudo numérico da robustez dos estados de superfície, explorando as diferenças entre tipos e distribuições de impurezas.

No contexto da técnica experimental *Fourier-transform scanning tunneling microscopy* (STM), identificamos indicadores experimentais que detectam estados de superfície exóticos no limite de impurezas muito diluídas. Mostramos que cada tipo de estado de superfície possui uma assinatura universal no seu padrão de interferência; STM, enquanto técnica de superfície, é particularmente adequada para a detecção dos estados topológicos.

Estudamos as consequências de intensa desordem de superfície sem alterar drasticamente as propriedades topológicas do volume. Dois limites são particularmente importantes.

O primeiro diz respeito a fortes flutuações no potencial electrostático, que leva à formação de uma grande concentração de estados localizados de Anderson. Mostramos que estes estados podem facilitar processos de difusão entre estados de superfície, dada a sua proximidade energética. Este tipo de desordem tem por isso um impacto negativo – eventualmente até fatal – nos estados de superfície, sendo o seu efeito máximo quando as flutuações são próximas da largura da banda.

O segundo limite de desordem aqui considerado relaciona-se com impurezas fortes localizadas na superfície. Estas impurezas podem ser vistas como vagas ou rugosidade na estrutura cristalina. Na presença deste tipo de desordem, os estados de superfície migram para camadas interiores da estrutura, de modo a evitar as impurezas. Assim, tanto para fases topológicas com como sem hiato energético, este tipo de desordem é inofensivo. Este

resultado é especialmente importante quando se consideram fases topológicas nodais, onde a invariante topológica é definido pelo momento de superfície, o que requer simetria de translação. Por exemplo, mostramos que introduzindo impurezas na superfície do isolador topológico Seleneto de Bismuto é possível alcançar melhores resultados em experiências de fotoemissão.

Consideramos ainda a relação entre topologia e interações entre electrões na superfície de supercondutores topológicos nodais. Aqui, a degenerescência infinita dos estados de superfície sem dispersão é susceptível a quebra espontânea de simetria. Mostramos que, neste caso, a simetria de inversão do tempo é espontaneamente quebrada, resultando num condensado com parâmetro de ordem de valor complexo. Consequentemente, vemos a formação de correntes quirais localizadas na superfície de superconductors nodais.

Finalmente, estudamos as possíveis interações que potencialmente levam à completa destruição dos estados topológicos de superfície, preservando todas as simetrias do sistema. Foi recentemente proposto que tal é possível em sistemas unidimensionais, desde que as interações emparelhem oito estados de superfície. Usando uma construção hierárquica na dimensão dos sistemas, propomos uma forma geral para interação que possibilita a conexão adiabática entre diferentes sectores topológicos.

Acknowledgements

This work would have not have been possible without the support and encouragement of many people for which I am deeply grateful. First, I am indebted to my supervisor Andreas Schnyder for introducing me to many interesting problems and techniques that will serve as a foundation for my future career. I would like to express my gratitude to Prof. Walter Metzner for the opportunity to be part of a wonderful group of scientists at the Max Planck Institute, and providing me with the freedom to travel, thereby allowing me to come in contact and learn from countless inspiring people. I would like to thank Prof. Maria Daghofer and Prof. Tilman Pfau at the University of Stuttgart for showing interest in my work and agreeing to be part of my examination committee.

My greatest appreciation goes to my collaborators, Johannes Hoffman for many fun discussions and great results; Eslam Khalaf for constantly reminding me how exciting solving problems can be; Mario Cuoco for being so enthusiastic; Hugo Dil for the opportunity to interact with the experimental world; and finally Ady Stern, for constantly challenging my statements and pushing me to really understand them.

Getting too focused on a single problem was always avoided by dynamic journal clubs and casual meetings. For this I need to thank Tobias Holder, Andreas Eberlein, Pavel Ioselevich, Federico Benitez, Xia-Wei Cheng, Darrick Lee, Nikolai Bittner, Pavel Ostrovsky, Fabien Trousselet and Wei Chen. The days in the institute were always highlighted by fun lunches and coffee breaks, where discussions on a wide range of interesting topics never failed to be stimulating. A special thanks goes to Peter Horsch, Roland Zeyer, Dirk Manske, Nils Hasselmann, Johannes Bauer, Adolfo Avella and Andrzej Oles.

I would have had a hard time without the strong support of the computer service team, my special thanks goes to Armin Burkhardt and Armin Schuhmacher for having so much patience, together with an apology for filling the cluster memory one too many times. A heartfelt appreciation goes to Jeanette Schüller-Knapp and Hans-Georg Libuda, for their unlimited help in bureaucratic matter.

A special thank you goes to Stefanos Kourtis, for his never-ending encouragement, many travels, and finally his comments on this manuscript.

Living in Stuttgart for four years was bound to be an important episode in my life. As expected, the city has seen me grow and witnessed many dear friendships. I must acknowledge

the unconditional support of a few: Anna Mercader for being an inspiration; Ramsay Nashev for walks, word games and playgrounds; Peter Hofmann for his kindness; My flatmates Gamze Mandaci, Marcel Seedorf and Olga Kiefer for so many good moments and good food; Marta Sofia, Ozan Polat, Elif Taskin, Andressa Ocker and Diana Schmidt, who always made it exciting; Mafalda Mendes Lopes, Rui Coelho and João Caldeira for bringing home to Germany every now and then. Finally, Martin Bluschke not only for the strong partnership, but also for never being satisfied with a dodgy scientific explanation.

I dedicate this thesis to the most influential people in my life, who have shaped me to be enchanted with nature and to never decline a challenge. My kind and supportive mother Maria João Queiroz; my stimulating and unbelievably funny father João Queiroz and my creative and perceptive sister Ana Queiroz. This family is my foundation and have created the ideal environment and strongest support system someone could possibly ask for. Going home for lunches that merge into late dinners was the true reason for keeping my sanity during this entire experience.